Department of Radio Science and Engineering

Developments in imaging at millimeter and submillimeter wavelengths

---

Aleksi Tamminen

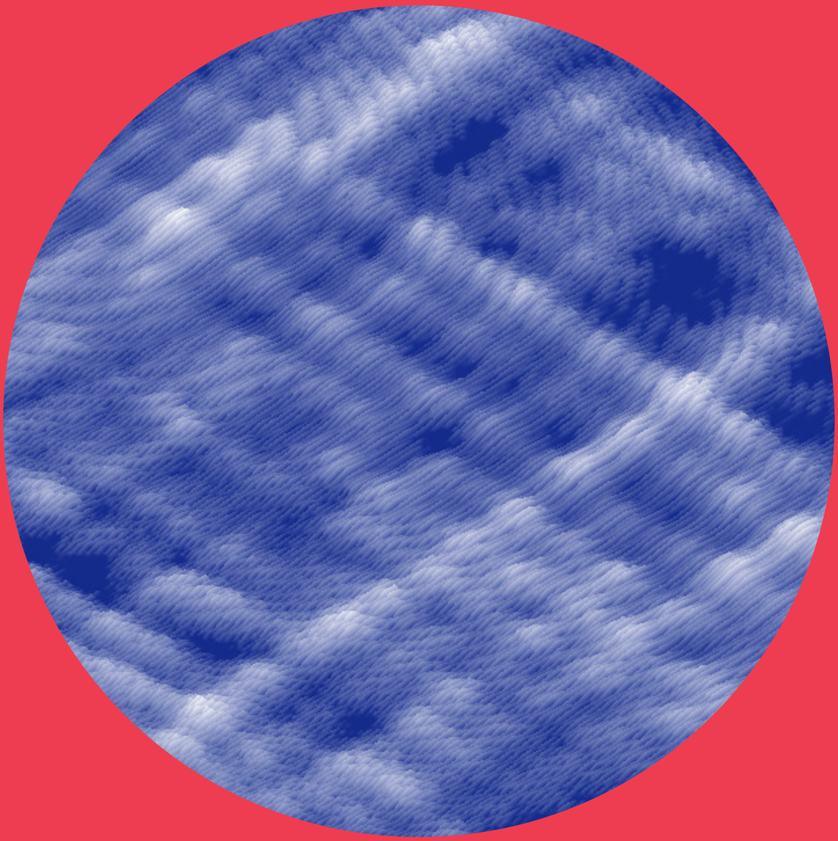

Aalto University

DOCTORAL
DISSERTATIONS

Aalto University publication series
DOCTORAL DISSERTATIONS 131/2013

Developments in imaging at millimeter and submillimeter wavelengths

Aleksi Tamminen

A doctoral dissertation completed for the degree of Doctor of Science (Technology) to be defended, with the permission of the Aalto University School of Electrical Engineering, at a public examination held at the lecture hall S2 of the school on 24 September 2013 at 12.

Aalto University
School of Electrical Engineering
Department of Radio Science and Engineering

Supervising professor
Professor Antti Räisänen

Thesis advisor
D.Sc. (Tech.) Juha Ala-Laurinaho

Preliminary examiners
Dr. Yuri Álvarez, Assistant Professor, University of Oviedo, Spain
Dr. Sergey Pivnenko, Associate Professor, Technical University of Denmark, Denmark

Opponent
Dr. Duncan Robertson, University of St. Andrews, Scotland, UK

Aalto University publication series
DOCTORAL DISSERTATIONS 131/2013

ISBN 978-952-60-5300-4 (printed)
ISBN 978-952-60-5301-1 (pdf)
ISSN-L 1799-4934
ISSN 1799-4934 (printed)
ISSN 1799-4942 (pdf)
http://urn.fi/URN:ISBN:978-952-60-5301-1

Unigrafia Oy
Helsinki 2013

Finland

NORDIC ECOLABEL
441 697
Printed matter

Aalto University

Abstract

Aalto University, P.O. Box 11000, FI-00076 Aalto www.aalto.fi

Author
Aleksi Tamminen

Name of the doctoral dissertation
Developments in imaging at millimeter and submillimeter wavelengths

Publisher School of Electrical Engineering

Unit Department of Radio Science and Engineering

Series Aalto University publication series DOCTORAL DISSERTATIONS 131/2013

Field of research Radio engineering

Manuscript submitted 13 June 2013 **Date of the defence** 24 September 2013

Permission to publish granted (date) 22 August 2013 **Language** English

☐ **Monograph** ☒ **Article dissertation (summary + original articles)**

Abstract

This thesis presents novel experimental results in the fields of millimeter- and submillimeter-wave imaging, reflectivity studies, as well as power detector characterization. The overlapping topics share key concepts of beam steering, holography, and antenna measurements.

Indirect holographic imaging technique is verified experimentally for the first time. This method allows for coherent detection of a target, using a reference wave and simple direct detection receivers. This is very promising, since receiver complexity is seen as the greatest hindrance to the realization of large imaging arrays. In the holographic method, coherent detection and focusing of the image is a post-detection task. A novel computational technique is introduced, which removes the restrictions on the reference-wave direction. In the experimental work at 310 GHz, the slanted-edge method is applied for estimating the point spread function. Experimental data indicate a decrease in resolution of 20-30 % compared to a diffraction limited case. The noise-equivalent reflectivity difference (NERD) is found to be approximately constant (NERD = 0.002), down to the received signal SNR of 26 dB.

Reflectarrays (RAs) are developed and characterized at 120 GHz. The RAs enable beam-steering, and they are designed to be compatible with MEMS microfabrication. Three static RAs are characterized in a near-field measurement range. The measured beamwidths are within 10 % of the simulated ones. The specular reflection from RAs is studied, and the concept of RA efficiency is introduced. The experimentally determined efficiency is found to be 0.11 while simulation results suggest an average efficiency of 0.54.

Reflection- and transmission-type phase holograms are used to create a planar wave front, quiet zone (QZ), in a compact test range at both 310 and 650 GHz. The measured QZ variation is ±1.5 dB and ±5° at 310 GHz and ±3 dB and ±25° at 650 GHz. The holograms are suitable for use in radar-cross-section (RCS) measurements. The reflectivity of different radar-absorbing materials (RAMs) is studied in a RCS range. Commercial RAM and low-cost materials are compared for their monostatic reflectivity in an angular range of 45° and 12° at 310 and 650 GHz, respectively. It is found that common materials, such as carpets have reflectivity from −60 to −30 dB, and are suitable for use as RAM.

Bolometers used in a submillimeter-wave imager are studied at 321-782 GHz. The antenna-coupled microbolometers are characterized in room temperature. They are coupled with an equi-angular spiral antenna and a silicon substrate lens. The beamwidth of the bolometers is found to follow an 8.5°/THz –relation across the band. A low-cost infrared detector is compared with dedicated power meters. It is found to have a sensitivity of 1700 V/W and noise-equivalent power (NEP) of $0.4\ \mu\mathrm{W}/\sqrt{\mathrm{Hz}}$. As such, it can be used as an ad hoc power detector.

Keywords bolometer, hologram, imaging, reflectarray, reflectivity

ISBN (printed) 978-952-60-5300-4 **ISBN (pdf)** 978-952-60-5301-1

ISSN-L 1799-4934 **ISSN (printed)** 1799-4934 **ISSN (pdf)** 1799-4942

Location of publisher Helsinki **Location of printing** Helsinki **Year** 2013

Pages 177 **urn** http://urn.fi/URN:ISBN:978-952-60-5301-1

Aalto-yliopisto

Aalto-yliopisto, PL 11000, 00076 Aalto www.aalto.fi

Tiivistelmä

Tekijä
Aleksi Tamminen

Väitöskirjan nimi
Millimetri- ja alimillimetriaaltoalueen kuvantamismenetelmien kehittämisestä

Julkaisija Sähkötekniikan korkeakoulu

Yksikkö Radiotieteen ja -tekniikan laitos

Sarja Aalto University publication series DOCTORAL DISSERTATIONS 131/2013

Tutkimusala Radiotekniikka

Käsikirjoituksen pvm 13.06.2013 **Väitöspäivä** 24.09.2013

Julkaisuluvan myöntämispäivä 22.08.2013 **Kieli** Englanti

☐ **Monografia** ☒ **Yhdistelmäväitöskirja (yhteenveto-osa + erillisartikkelit)**

Tiivistelmä

Tämä väitöskirja käsittelee millimetri- ja alimillimetriaaltoalueen kuvantamista, materiaalien heijastavuusmittauksia ja tehoilmaisimien karakterisointia. Aihealueet liittyvät toisiinsa keilanohjauksen, holografian ja antennimittausten kautta.

Epäsuora holografinen menetelmä on kokeellisesti varmennettu. Menetelmä mahdollistaa vaiheilmaisun referenssikentän ja yksinkertaisten tehovastaanottimien avulla. Tulokset ovat erittäin lupaavia, sillä vaihekoherentti vastaanotinryhmä on erittäin monimutkainen toteuttaa. Epäsuorassa holografisessa menetelmässä vaiheenilmaisu ja kuvan fokusointi tehdään tehoilmaisun jälkeen laskennallisesti. Työssä esitellään uusi menetelmä, jossa referenssikentän tulosuuntaa ei ole rajoitettu. Taajuudella 310 GHz saaduista kuvista on approksimoitu impulssivaste käyttäen askel-tyyppistä kohdetta. Diffraktion rajoittamaan teoreettiseen arvoon verrattuna erotuskyky kokeellisissa tuloksissa oli 20-30 % alempi. Kohinatasoinen heijastavuusero on 0,002, kun ilmaistun tehon signaali-kohina –suhde on 26 dB.

Työssä käsitellään 120 GHz:n heijastusantenniryhmää. Antenniryhmät ovat tarkoitettu käytettäviksi keilanohjauksessa, ja niiden valmistustekniikka soveltuu myös mikroelektromekaanisten komponenttien valmistukseen. Kolmea heijastusantenniryhmää, joiden keilat ovat pysyvästi fokusoitu, on karakterisoitu lähikenttämittauspaikalla. Mitatut keilanleveydet vastaavat 10 %:n tarkkuudella simuloituja. Heijastusantenniryhmien peiliheijastusta kuvaamaan on määritelty hyötysuhde. Hyötysuhteeksi saatiin kokeellisesti 0,11, kun teoreettinen hyötysuhde on keskimäärin 0,54.

Heijastus- ja läpäisytyyppisiä vaihehologrammeja on käytetty tasomaisen kentän eli hiljaisen alueen luomiseen kompaktissa mittauspaikassa. Mitattu amplitudi- ja vaihevaihtelu hiljaisessa alueessa on ±1,5 dB ja ±5° 310 GHz:llä sekä ±3 dB ja ±25° 650 GHz:llä. Hologrammeja voidaan käyttää tutkapoikkipinta-alan mittaukseen. Tässä työssä verrattiin tarkoitusta varten valmistettujen vaimennusmateriaalien ja muiden materiaalien heijastavuutta. Takaisinheijastavuus mitattiin 45°:n ja 12°:n kulma-alueessa 310 ja 650 GHz:llä. Matoille mitattiin heijastavuuksia −60 dB:stä −30 dB:iin, joten ne soveltuvat vaimennusmateriaaliksi.

Kuvantamisessa käytettäviä NbN -bolometrejä on tutkittu taajuusalueessa 321-782 GHz. Antennikytkettyjä bolometrejä on karakterisoitu huoneenlämpötilassa tehonmittaukseen perustuvassa antennimittauspaikassa. Bolometrit on kytketty spiraali-antenniin piisubstraattilinssin pinnalla. Bolometri-ilmaisimien keilanleveys noudattaa 8,5°/THz –lakia mitatulla taajuusalueella. Edullista infrapunailmaisinta on verrattu tarkoituksenmukaisiin tehomittareihin. Ilmaisimen kokeellisesti mitattu herkkyys ja kohinaekvivalentti teho ovat 1700 W/V ja $0.4\ \mu\mathrm{W}/\sqrt{\mathrm{Hz}}$, joten se soveltuu ad hoc tehonilmaisuun alimillimetriaaltoalueella.

Avainsanat bolometri, heijastavuus, heijastusantenniryhmä, hologrammi, kuvantaminen

ISBN (painettu) 978-952-60-5300-4 **ISBN (pdf)** 978-952-60-5301-1

ISSN-L 1799-4934 **ISSN (painettu)** 1799-4934 **ISSN (pdf)** 1799-4942

Julkaisupaikka Helsinki **Painopaikka** Helsinki **Vuosi** 2013

Sivumäärä 177 **urn** http://urn.fi/URN:ISBN:978-952-60-5301-1

Preface

My warmest thanks go to my supervisor, Professor Antti Räisänen, who has offered me the opportunity to work on such interesting research topics over the past several years. Very warm thanks go also to my instructor, Dr. Juha Ala-Laurinaho, whose guidance and impressive knowledge on science have supported my work.

I am grateful for the support from colleagues at the department and elsewhere: Aki, Amin, Anne, Antti, Arttu, Eero, Eino, Eric, Erich, Janne H., Janne I., Jari, Juha, Juho, Jussi, Katsu, Krista, Matti, Mikko, Olli, Pablo, Patrick, Pekka A., Pekka P., Pekka R., Pekka R., Päivi, Risto, Sampo, Tero, Tom, Tomi, Veli-Matti, Viktor, Ville, and Zhou, and from all the personnel at the department. Thank you all.

I appreciate the extensive work carried out by the pre-examiners of this thesis, Professors Yuri Alvaréz and Sergey Pivnenko. Their insightful notions on the manuscript have been extremely valuable.

The work reported in this thesis has been done at the Aalto University School of Electrical Engineering, in the Department of Radio Science and Engineering. This work has been supported by the Graduate School in Electronics, Telecommunications and Automation (GETA), from the Academy of Finland through its Centre of Excellence program SMARAD and from the Finnish Funding Agency for Technology and Innovation (TEKES). I am especially grateful for the financial support from the Association for Electronics Engineers, Emil Aaltonen Foundation, Finnish Foundation for Technology Promotion, HPY Research Foundation, Jenny and Antti Wihuri Foundation, and Nokia Foundation.

Along all the years, my friends from both academia and elsewhere have supported and encouraged me in my expedition. I cherish you. Lopuksi haluan kiittää perhettäni, joka on pitänyt minusta huolen.

Espoo, 27th August 2013,

Aleksi Tamminen

Contents

List of publications

This thesis is based on the following publications, which are referred to in the text by their Roman numerals:

[I] A. Tamminen, J. Ala-Laurinaho, and A. V. Räisänen, “Indirect holographic imaging at 310 GHz,” in *Proceedings of the 5th European Radar Conference*, Amsterdam, the Netherlands, 2008, pp. 168-171.

[II] A. Tamminen, J. Ala-Laurinaho, and A. V. Räisänen, “Indirect holographic imaging: evaluation of image quality at 310 GHz,” in *Proceedings of SPIE, Passive Millimeter-Wave Imaging Technology XIII*, vol. 7670, Orlando, FL, USA, 2010, publication no. 76700A.

[III] A. Enayati, A. Tamminen, J. Ala-Laurinaho, A. V. Räisänen, W. D. Raedt, G. A. Vandenbosch, “THz holographic imaging: a spatial-domain technique for phase retrieval and image reconstruction,” in *IEEE International Microwave Symposium Digest*, Montreal, Canada, 2012, publication no. TU1A-5.

[IV] A. Tamminen, S. Mäkelä, J. Ala-Laurinaho, P. Koivisto, P. Rantakari, J. Säily, J. Häkli, A. Luukanen, and A. V. Räisänen, “Reflectarray design for 120-GHz radar application: measurement results,” *IEEE Transactions on Antennas and Propagation*, accepted for publication, 2013.

[V] A. Tamminen, A. Karttunen, M. Vaaja, E. Noponen, J. Ala-Laurinaho, J. Mallat, and A. V. Räisänen, “Reflection-type phase hologram for beam shaping: experimental results at 310 GHz,” in *Proceedings of the 30th ESA Antenna Workshop on Antennas for Earth Observation, Science, Telecommunication and Navigation Space Missions*, Noorwijk, The Netherlands, 2008, pp. 470-473.

[VI] A. Lönnqvist, A. Tamminen, J. Mallat, and A. V. Räisänen, “Monostatic reflectivity measurement of radar absorbing materials at 310 GHz,” *IEEE Transactions on Microwave Theory and Techniques*, vol. 54, no. 9, pp. 3486-3491, 2006.

[VII] A. Tamminen, A. Lönnqvist, J. Mallat, and A. V. Räisänen, “Monostatic reflectivity and transmittance of radar absorbing materials at 650 GHz,” *IEEE Transactions on Microwave Theory and Techniques*, vol. 56, no. 3, pp. 632-637, 2008.

[VIII] A. Tamminen, J. Ala-Laurinaho, J. Mallat, A. Luukanen, E. N. Grossman, and A. V. Räisänen, “Wide-band measurements of antenna-coupled microbolometers for THz imaging,” *Journal of The Korean Institute of Electromagnetic Engineering and Science*, vol. 10, no. 3, pp. 132-137, 2010.

[IX] A. Tamminen, J. Ala-Laurinaho, and A. V. Räisänen, “Submillimeter-wave power measurements with commercial infra-red detectors,” in *Proceedings of the 5th European Radar Conference*, Paris, France, 2010, pp. 288-291.

Author's contribution

[I] This work was mainly done by the author. The method of indirect holographic imaging was proposed by Prof. Antti Räisänen. The author designed the measurement procedure, carried out the measurements, processed the measurement data, and was responsible for writing the publication. Dr. Juha Ala-Laurinaho and Prof. Antti Räisänen supervised the work.

[II] This work was mainly done by the author. The methods to evaluate the quality of millimeter-wave images were proposed, designed, and applied by the author. The measurements and data processing were carried out by the author. Furthermore, the author was responsible for writing the publication. Dr. Juha Ala-Laurinaho and Prof. Antti Räisänen supervised the work.

[III] This is the result of collaborative work. The idea of the spatial-domain technique was proposed by the author. The author carried out the measurements and helped in writing the publication. Mr. Amin Enayati processed the measurement data, formulated the technique in detail, and was responsible for writing the publication. Dr. Juha Ala-Laurinaho, Prof. Antti Räisänen, Dr. Walter De Raedt, and Prof. Guy Vandenbosch supervised the work.

[IV] This is the result of collaborative work. The author designed and simulated the reflectarray element, processed the measurement data, and was responsible for writing the publication. The measurements were carried out together by the author and Mr. Sampo Mäkelä. Dr. Päivi Koivisto, Dr. Jussi Säily, and Dr. Janne Häkli designed the phasing patterns and the general specifications of the reflectarrays. Mr. Pekka Rantakari designed and measured the MEMS phase shifter. Dr. Juha Ala-Laurinaho helped with the simulations and measurement data processing. Prof. Arttu Luukanen and Prof. Antti Räisänen supervised the work.

[V] This is the result of collaborative work. The author carried out the measurements and was responsible for writing the publication. The co-authors were involved in designing and simulating the hologram as well as developing the measurement routines for hologram characterization. Prof. Antti Räisänen supervised the work.

[VI] This work was mainly done by the author. The method of reflectivity measurement was proposed by Dr. Anne Väänänen (née Lönnqvist). The author carried out the measurements, processed the measured data, and was responsible for writing the publication. Dr. Juha Mallat and Prof. Antti Räisänen supervised the work.

[VII] This is the result of collaborative work. The author carried out the measurements and processed the data for the publication. The method of reflectivity measurement was proposed by Dr. Anne Väänänen (née Lönnqvist) and she was responsible for writing the publication. Dr. Juha Mallat and Prof. Antti Räisänen supervised the work.

[VIII] This work was mainly done by the author. The author designed the measurement procedure, carried out the measurements with bolometers, and was responsible for writing the publication. The bolometers were designed by Dr. Erich Grossmann and Prof. Arttu Luukanen. Dr. Juha Ala-Laurinaho and Prof. Antti Räisänen supervised the work.

[IX] This work was mainly done by the author. The idea for detector characterization was proposed by the author. Design of the measurement setup, and measurements were done by the author. The author was responsible for writing the publication. Dr. Juha Ala-Laurinaho and Prof. Antti Räisänen supervised the work.

List of abbreviations

AC	Alternating current
AUT	Antenna under test
BWO	Backward-wave oscillator
CATR	Compact antenna test range
CMOS	Complementary metal oxide semiconductor
CNC	Computerized numerical control
DC	Direct current
DUT	Device under test
ESA-1-FC	Extended source association, transmitter
ESA-2-FC	Extended source association, receiver
ESF	Edge spread function
FMCW	Frequency-modulated-continuous-wave
FoV	Field of view
FPA	Focal plane array
HA	Hologram aperture
HFSS	High frequency structural simulator
ITU-R	Radiocommunication sector of the International Telecommunication Union
LSF	Line spread function
MATLAB	Matrix laboratory
MEMS	Microelectromechanical system
MVNA-8-350	Millimeter-wave network analyzer 8-350
NEP	Noise-equivalent power
NERD	Noise-equivalent reflectivity difference
NSI	Near-field Systems Inc.
PSF	Point spread function
PTFE	Polytetrafluoroethylene
PVC	Polyvinyl chloride
PWS	Plane wave spectrum
QZ	Quiet zone
RA	Reflectarray
RAM	Radar absorbing material
RCS	Radar cross section
RF	Radio frequency
SNR	Signal-to-noise ratio

TEB	Transition-edge bolometer
USAF	Unites States Air Force
VTT	Valtion Teknillinen Tutkimuskeskus, Technical Research Centre of Finland

List of symbols

A_e	Effective aperture
AF	Array factor
A_N	Gaussian-distributed random number
A_R	Amplitude of the reference wave
a	Absorption
a_eq	Opening rate of the spiral of the equi-angular antenna
a_m	Amplitude weight
B	Bandwidth
B_R	Spatial bandwidth of the reference wave
B_T	Spatial bandwidth of the target wave
b	Number of bits
C	Intermediate variable
c	Speed of light
D	Largest dimension of a focusing element
D_H	Diameter of the hologram
D_proj	Projected diameter
D_T	Diameter of the target
d	Element spacing
$\mathbf{E}$	Electric field density
$\mathbf{E}_0$	Electric field density of the reflection from background
$\mathbf{E}_\mathrm{I}$	Electric field density of the illuminating wave
$\mathbf{E}_\mathrm{R}$	Electric field density of the reference wave
$\mathbf{E}_\mathrm{T}$	Electric field density of the target wave
$\mathbf{E}_\mathrm{u}$	Electric field density of a plane-wave mode
$\hat{\mathbf{E}}_\mathrm{u}$	Plane wave spectrum
E_a	Electric field density at the aperture
$E_\mathrm{R,M}$	Modeled reference wave
$E_\mathrm{T,E}$	Erroneous target wave
e	Emissivity
F	Focal length
$f\#$	f-number
f_r	Frame rate
G	Scalar Green's function
G_0	Gain of a reflectarray with continuous phase shift
G_f	Focusing gain
G_q	Gain of a reflectarray with quantized phase shift
G_RA	Gain of the reflectarray

$\mathbf{H}$	Magnetic field density
H	Height of aperture
h	Height of lens
h_{hyper}	Hyper-hemispherical height
I	Interference pattern
I_{N}	Interference pattern with added noise
$\mathbf{J}$	Electric current density
$\mathbf{J}_{\mathrm{m}}$	Magnetic current density
$\mathbf{J}_{\mathrm{ms}}$	Magnetic surface current density
$\mathbf{J}_{\mathrm{s}}$	Electric surface current density
j	Imaginary unit
k	Free-space wave number
k_{crit}	Critical wave number
k_{x}	x-component of the wave vector
$k_{\mathrm{x}_{\mathrm{p}}}$	Indexed x-component of the wave vector
k_{y}	y-component of the wave vector
$k_{\mathrm{y}_{\mathrm{w}}}$	Indexed y-component of the wave vector
L_{eq}	Arm length of an equi-angular spiral antenna
$\mathbf{n}$	Normal vector
N	Integer number
N_{d}	Number of detectors
N_{P}	Number of pixels
n	Index
m	Index
p	Index of the x-component of the wave vector
q	Quantization step of the phase shift
$\mathbf{r}$	Position vector of the observation point
$\mathbf{r}'$	Position vector on surface
$\mathbf{r}_{\mathrm{e}}$	Position vector of the reflectarray element
$\mathbf{r}_{\mathrm{f}}$	Position vector of the reflectarray focus
$\mathbf{r}_{\mathrm{s}}$	Position vector of the reflectarray source
$\hat{\mathbf{r}}_{\mathrm{f}}$	Directional vector of the reflectarray focus in spherical coordinate system
R	Distance
R_{l}	Radius of curvature of a lens
R_{R}	Reduction ratio in sampling
R_{RCS}	Largest of the target or quiet-zone diameter
r	Reflectivity
r_0	Starting radius of the equi-angular spiral antenna
r_{eq}	Radius of the equi-angular spiral antenna
r_{ff}	Far-field distance
r_{max}	Maximum radius of the equi-angular antenna spiral

r_{min}	Minimum radius of the equi-angular antenna spiral
r_{tot}	Total of the reflection coefficient
S	Surface
S_{ff}	Power density of the far-field focused reflectarray
S_{nf}	Power density of the near-field focused reflectarray
T	Physical temperature
T_{B}	Brightness temperature of the background
T_{S}	Brightness temperature of the surroundings
T_{T}	Apparent brightness temperature of the target
t	Transmittance
$\mathbf{u}_{\mathrm{\rho}}$	Radial unit vector in spherical coordinate system
$\mathbf{u}_{\mathrm{x}}$	Unit vector for Cartesian x-coordinate
$\mathbf{u}_{\mathrm{y}}$	Unit vector for Cartesian y-coordinate
$\mathbf{u}_{\mathrm{z}}$	Unit vector for Cartesian z-coordinate
U_{amp}	Uncertainty in amplitude
U_{phase}	Uncertainty in phase
u	x-component of the spatial frequency, directional cosine
u_0	Directional cosine
u_n	Indexed x-component of the spatial frequency, indexed directional cosine
u_{R}	Spatial frequency of the reference wave
v	y-component of the spatial frequency, directional cosine
w	Index of the y-component of the wave vector
x	Cartesian coordinate
x'	Cartesian coordinate on surface
x_{e}	x-coordinate of the reflectarray element
x_{f}	x-coordinate of the reflectarray focus
x_m	Indexed x-coordinate
x_{R}	Cartesian x-coordinate of the reference wave feed
$x_{\mathrm{R,M}}$	Cartesian modeled x-coordinate of the reference wave feed
x_{s}	x-coordinate of the reflectarray source
y	Cartesian coordinate
y'	Cartesian coordinate on surface
y_{e}	y*-coordinate* of the reflectarray element
y_{f}	y-coordinate of the reflectarray focus
y_m	Indexed y-coordinate
y_{R}	Cartesian y-coordinate of the reference wave feed
$y_{\mathrm{R,M}}$	Cartesian modeled y coordinate of the reference wave feed
y_{s}	Cartesian y-coordinate of the source
Z_{SC}	Input impedance of a self-complementary antenna
z	Cartesian coordinate
z'	Cartesian coordinate on surface

z_{f}	z-coordinate of the reflectarray focus
z_{R}	Cartesian z-coordinate of the reference wave feed
$z_{\mathrm{R,M}}$	Cartesian modeled z-coordinate of the reference wave feed
z_{s}	z-coordinate of the reflectarray source
z_{T}	Cartesian z-coordinate of the target

Γ	Reflection coefficient
Γ_{e}	Reflection coefficient of the reflectarray element
Γ_{m}	Re-radiated component of the reflection coefficient
Γ_{model}	Modeled reflectivity
Γ_{RAM}	Reflectivity of the radar-absorbing material sample
Γ_{s}	Specular component of the reflection coefficient
ΔR	Reflectivity measurement error
Δ_r	In-range resolution
Δb	Misalignment of the bolometer
δ	Pulse width
ε	Permittivity
ε_0	Permittivity of vacuum
$\varepsilon_{\mathrm{eff}}$	Effective relative permittivity
ε_{r}	Relative permittivity
$\varepsilon_{\mathrm{Si}}$	Relative permittivity of silicon
η_{diff}	Diffraction efficiency of the hologram
η_{e}	Reflectarray element efficiency
η_{l}	Efficiency due to dielectric and resistive loss
η_{q}	Quantization efficiency
η_{s}	Spillover efficiency
η_{t}	Amplitude taper efficiency
θ	Incident angle
θ_{-3dB}	−3-dB antenna beamwidth
θ_{Bragg}	Angle of Bragg's diffraction maximum
θ_{max}	Maximum beam steering angle, maximum angle of propagation
θ_{off}	Offset angle of the main beam
θ_{R}	Reference wave angle
$\theta_{\mathrm{T\,max}}$	Greatest incidence angle of the target wave
λ	Free-space wavelength
μ	Magnetic permeability
μ_0	Magnetic permeability of vacuum
τ	Integration time
Φ	Opening angle of the equi-angular spiral antenna
φ_0	Phase constant
φ_{R}	Reference wave phase
φ_{T}	Target wave phase
$\varphi_{\mathrm{T,E}}$	Error of the target wave phase
ψ	Quantization error
ω	Angular frequency

1 Introduction

Millimeter and submillimeter waves are loosely defined designations for the part of electromagnetic spectrum, where the free space wavelength ranges from 10 millimeters down to 0.1 millimeter [1]. In frequency, these waves range from 30 GHz to 3000 GHz. This designation is used throughout the thesis. Another designation for the submillimeter-wave range is terahertz waves, and it is used to describe electromagnetic radiation from 300 GHz, sometimes even from 100 GHz, to near infrared [2].

The electromagnetic spectrum from the gamma rays to the extremely-low frequencies is crowded with applications, some are more every-day some less so. The conventional technologies used at the extremes of the spectrum, optical and radio-frequency technology, struggle to provide cost-effective solutions at millimeter and submillimeter waves [3]. Technology is now being strongly driven towards this spectral range due to promises it gives to wireless communication systems [4], radio astronomy [5], [6] and other sciences, as well as due to its suitability in imaging applications [7].

Currently, millimeter-wave technology is replacing the microwave technology in wireless systems, whereas submillimeter waves are still utilized mostly in scientific applications. Security imaging for illicit hidden objects [8] and medical use [9] are foreseen as the first commercial applications, which will exploit the submillimeter waves. In commercial applications, trend is towards ever higher wireless data rates with technology packed in ever more compact form. Data rate can be increased due to the larger absolute bandwidth available at millimeter waves. Also, important to the wireless technologies, at millimeter waves the footprint of components is smaller compared to similar devices operating at lower frequencies. Pursuing to millimeter waves is in this case motivated by the benefit from scaling.

In addition to the advantage of penetrating some materials that are opaque at optical wavelengths, imaging at submillimeter wavelengths is also motivated by scaling. In a typical imaging scheme, submillimeter wavelength propagation can be approximated to be ray-like, and high-resolution imaging with convenient-sized apertures is possible. Also, some physical phenomena exist only at submillimeter waves and attract developing technology for that part of the electromagnetic spectrum. E.g., the unique rotational, vibrational, and phonon resonances of chemicals of interest take place at high end of submillimeter waves [7].

1. 1 Motivation and scope of the thesis

Despite of the advances in millimeter- and submillimeter-wave technology, many of the foreseen applications are neither at a mature, nor an affordable level. As this wavelength range lies between the microwaves and far-infrared, both electrical and optical approaches are adapted in realization of the applications. Unfortunately, scaling the technology for the wavelength range faces barriers due to the limited fabricating accuracies and unfavorable material properties [3]. Today, the coherent submillimeter-wave transmitters and receivers are bulky laboratory instruments rather than commercial products. Especially, the low level of integration in the devices prohibits compact-sized applications. Also, inadequate knowledge of material electrical properties at the wavelength ranges discourages for new applications. The ever-present limitation due to the atmospheric attenuation limits number of sea-level applications to few.

This thesis discusses the developments in millimeter- and submillimeter-wave range, especially in imaging. The research topics with brief descriptions are listed in Table 1-1. The work is motivated by the need to find cost-effective solutions both in measurement techniques and in realization of systems, such as a submillimeter-wave imager. The expected cost-effectiveness is based on minimizing the detector count and implementing only relatively simple technology, such as bolometers in passive imaging or MEMS in a reconfigurable reflectarray. Especially, the indirect holographic imaging technique allows for phase detection from amplitude measurement only, reducing the receiver complexity compared to conventional heterodyne detection. The thesis is organized as follows: Chapter 2 discusses the background of the research and introduces the numerical and experimental methods used to achieve the findings reported in publications [I]-[IX]. Chapter 3 discusses the novel indirect holographic technique and the experimental work reported in publications [I]-[III]. Chapter 4 discusses the design aspects of millimeter-wave reflectarrays, introduces the application of millimeter-wave reflectarray, and the related measurements reported in publication [IV]. Submillimeter-wave holograms, [V], and their application in reflectivity measurements in a RCS-measurement range, [VI], [VII], are discussed in Chapter 5. Chapter 6 discusses on characterization of bolometers for passive submillimeter-wave imaging [VIII]. Also, the application of an ad hoc power detector is described. Finally, Chapters 7 and 8 summarize the related publications, lay down conclusions, and describe the future directions of the research.

Table 1-1. The research topics discussed in Chapters 3-6.

Chapter	Topic / Application	Description	Frequency (GHz)
3	Indirect holographic imaging	Experimental target wave retrieval with Fourier- [I], [II] and spatial-based [III] techniques	310
4	Reflectarray for near-field focusing	Development and characterization of a reflectarray antenna. Aperture field analysis.	120
5	Characterization of a reflection-type phase hologram	Quiet zone characterization in a hologram-based compact range.	310
5	Monostatic reflectivity measurements of RAM	Reflectivity and transmittance measurements of different RAM using a hologram-based RCS range.	310 & 650
6	Characterization of antenna-coupled micro-bolometers and an ad hoc power detector	Radiation pattern measurement. Sensitivity and NEP of bolometers and an ad hoc power detector.	321-782

1.2 Scientific contributions of the thesis

The scientific achievements in this thesis are listed below. The thesis contributes to experimental work in the field of millimeter- and submillimeter-wave imaging and near-field measurements.

[I] The indirect holographic method with spherical reference wave is verified experimentally for the first time at submillimeter wavelengths. The methods to evaluate the image quality of millimeter-wave images are presented. The image quality metrics are used to characterize the image quality for the indirect holographic method. A novel spatial-domain technique for indirect holographic imaging is presented.

[II] The first reflectarrays for near-field focusing at 120 GHz have been developed and characterized. The specular reflection from reflectarrays is described quantitatively.

[III] Reflection-type phase hologram is characterized at 310 GHz for the first time. The monostatic reflectivity of radar absorbing materials is measured in far-field conditions in a compact radar-cross-section measurement range at 310 and 650 GHz.

[IV] Antenna-coupled microbolometers are experimentally characterized at 321-782 GHz. The wide-band behavior of the bolometer beam patterns is measured. The sensitivity and noise-equivalent power of an ad hoc submillimeter-wave power detector is measured.

2 Background of research

The technological development at submillimeter wavelengths faces challenges both of technical and fundamental nature, when compared to the microwave technology already at a mature level. As the wavelength gets smaller, loss and parasitic reactance increase in the components. At the same time, manufacturing tolerances become ever more difficult to meet. As a result, the designers of submillimeter-wave components have to resort to exotic materials and fabrication methods. Use of novel materials and techniques can dramatically increase the cost of submillimeter-wave applications. Despite of the great effort, the efficiency of submillimeter-wave devices is far from what is expected in RF and optical devices. Typical submillimeter-wave device converts less than 1 % of the DC power to electromagnetic radiation, whereas mobile RF amplifiers convert about 50 % and light-emitting diodes convert about 30 % [10]. Due to these limitations, submillimeter-wave applications are currently hardly cost-effective.

2. 1 Submillimeter-wave propagation

In addition to technological barriers, atmospheric attenuation increases towards the shorter wavelengths – challenging the link budget in submillimeter-wave applications. The atmospheric attenuation is mainly governed by the absorption lines of molecular oxygen and water. At submillimeter waves, the peak attenuation due to the absorption lines varies from about 40 dB/km at 325 GHz to more than 10000 dB/km at 557 GHz and 752 GHz, as is shown in Figure 2-1. In practice, the submillimeter-wave applications are designed to operate at the window frequencies between the absorption lines, where the attenuation is tolerable. Still, the attenuation due to the atmosphere is very limiting when considering the operation range of a submillimeter-wave system. The window frequencies can be utilized to large extent in active submillimeter-wave imaging, where the frequency band can be chosen freely, given the availability of technology. In passive imaging, detection is wide-band and there are only little possibilities to utilize the window frequencies. Typically, passive imaging systems are designed to have a cut-off frequency of few hundreds of gigahertz in order to avoid the opacity of the atmosphere at the high end of the submillimeter-wave range.

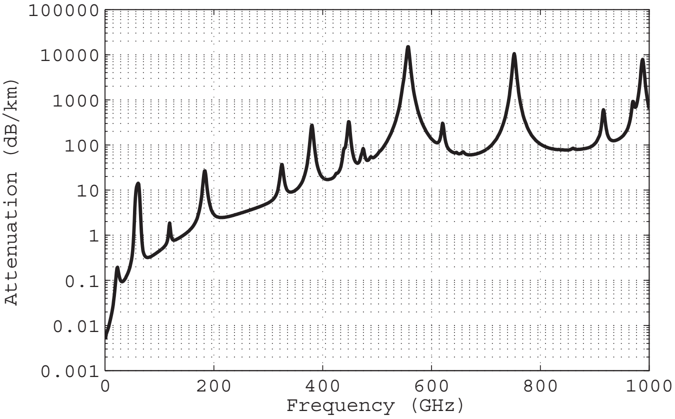

Figure 2-1. Atmospheric attenuation calculated based on the ITU-R P.676-9 recommendation [11]. The atmospheric conditions are: temperature of 300 K, water vapor density of 7.5 g/m^3, and air pressure of 1013 hPa.

2. 1. 1 *Hologram-based compact range*

The atmospheric attenuation is especially limiting factor in diagnostics of large millimeter-and submillimeter-wave antennas. Such antennas are operated outside of the sea-level atmosphere, either in high-elevation location or in space. They are used for radio astronomy missions or observation of the upper parts of the atmosphere. In their operational environment, atmospheric attenuation is not significant, but the antennas need to be assembled and tested in sea-level conditions. In conventional antenna measurement, the antenna needs to be measured at least at its far-field distance

$$r_{\mathrm{ff}} = \frac{2D^2}{\lambda}, \tag{2.1}$$

where D is the largest dimension of the antenna aperture and λ is the free-space wavelength. The parabolic antennas used in scientific satellites have typically a diameter of about 1 meter. E.g., at 650 GHz, the far-field distance is impractical 4.3 kilometers, leading to intolerable attenuation in the propagation path. The far-field conditions can be created in a compact antenna test range (CATR) within only short distance compared to the far-field distance. CATR allows for direct radiation pattern measurements for large antennas without the unbearable high atmospheric attenuation. CATRs based on reflectors have been used for antenna measurements since 1950's [12]. CATRs based on holograms were suggested in [13], and a lot of theoretical and experimental work has been done since, and it is discussed in [14], [15], [16]. An amplitude hologram has been successfully used in CATR at 39, 119, 322, and 650 GHz in [17], [18], [19], [20], respectively. The compact test range was suggested for radar-cross-section (RCS) measurements in [21], [22]. RCS measurements with scale models are reported in [23], [24], [25], [26]. There, phase holograms can be used to create a planar wave front. Phase holograms have higher efficiency than amplitude holograms. In this work, the RCS range with a phase hologram is used in reflectivity measurements at 310 and 650 GHz [VII],

[VI], and [27]. The holograms and reflectivity measurements are discussed more in detail in Chapter 5.

2. 2 Phenomenology in imaging

Submillimeter-wave imaging can be implemented both in active and passive scenarios. In passive imaging, only naturally occurring radiation is detected, whereas in active imaging, the target is illuminated from an artificial source [28]. In the literature, the established terminology for incoherent passive imaging describes the image as a map of brightness temperature across the scene. In coherent active imaging, the image is considered as a map of reflectivity. Both active and passive imaging can be realized by using simple wide-band detectors or narrow-band coherent receivers designated to track the spectral characteristics of the scene. As the availability of sensitive detectors at the high end of submillimeter waves is very limited, typical passive imager is designed to be very wide-band to collect as much as possible of the energy from the atmospheric window. In active imaging, coherent detection allows for high dynamic range and, if wide-band, for range determination. Also, imaging methods with computational focusing are possible.

In both active and passive scenarios, the return from the target is according to its emissivity e, reflectivity r, and transmittance t. The quantities depend on each other as

$$e + r + t = 1. \tag{2.2}$$

Emissivity describes the natural radiation from the target in passive imaging. In active imaging, term emissivity is usually replaced with absorption ($e = a$) in (2.2). Measured values of emissivity, reflectivity, and transmittance for certain materials are listed in Table 2-1.

Table 2-1. Emissivity, reflectivity, and transmittance of different materials at 100-1000 GHz [28]. The color coding emphases low values with dark and high values with light.

	Emissivity or absorption			*Reflectivity*			*Transmittance*		
	100 GHz	500 GHz	1 THz	100 GHz	500 GHz	1 THz	100 GHz	500 GHz	1 THz
Metal	0.0	0.0	0.0	1.0	1.0	1.0	0.0	0.0	0.0
Skin	0.65	0.91	0.93	0.35	0.09	0.07	0.0	0.0	0.0
Denim	0.09	0.49	0.85	0.01	0.01	0.05	0.90	0.50	0.10
T-shirt	0.04	0.20	0.30	0.00	0.00	0.05	0.96	0.80	0.65

0.00-0.25 ■ 0.25-0.50 ▨ 0.50-0.75 ▒ 0.75-1.00 □

Figure 2-2 shows the incoherent passive and coherent active imaging scenarios. In incoherent case, when the transmittance of the obscuring material is assumed to be unity, the apparent brightness temperature of the target is

$$T_{\mathrm{T}} = eT + rT_{\mathrm{S}} + tT_{\mathrm{B}}, \tag{2.3}$$

where T is the physical temperature of the target, T_{S} is the brightness temperature of the surroundings, and T_B is the brightness temperature of the background, on which the target lies. In addition to the temperatures, the contrast in passive imaging depends on emissivity, reflectivity, and transmittance of the target. In coherent active imaging, the return from the target is

$$E_{\mathrm{T}} = r_{\mathrm{tot}} E_{\mathrm{I}}, \tag{2.4}$$

where r_{tot} is the reflectivity of the target and E_{I} is the artificial illuminating field. The contrast in the images is due to reflectivity differences. In case of layered material, such as clothing, the reflection from the target is a combination of reflections from multiple interfaces of materials.

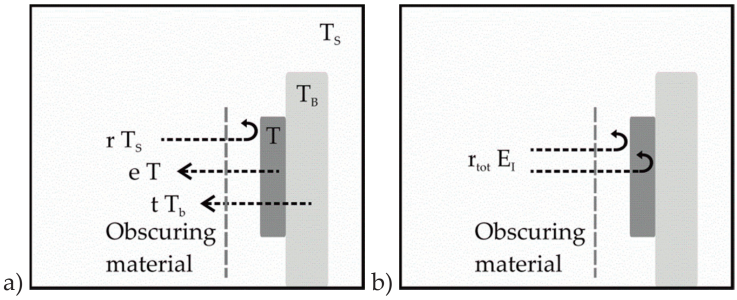

Figure 2-2. Contribution to image in a) passive imaging and b) active imaging. The obscuring material is assumed transparent at the imaging wavelengths.

2. 2. 1 Differences in active and passive imaging

At 100 GHz, clothing is almost transparent and reflectivity varies depending on the material. Many of the millimeter-wave images published at the 94-GHz atmospheric window have high contrast because of the difference how materials reflect the brightness temperature of the surroundings. Especially, the hot or cold brightness temperature of the sun or sky introduces high contrast in outdoor images. At higher frequencies the emissivity increases and transmittance drops. For example, a 2.2-mm layer of wool has increasing attenuation of ca. 1.5 dB/100 GHz [29]. Also, the reflectivity of materials decreases and becomes more independent on the material. As a consequence, the observed brightness temperature is less dependent on the surroundings and it resembles closer to the physical temperature of the target. Targets against any background tend to have similar physical temperature in equilibrium, and the contrast in the image decreases at high end of the submillimeter-wave range. Also, the emissivity of clothing is increased and even high-reflectivity metallic targets may not be detected, if they are obscured by the bright and opaque clothing. The detection in passive imaging is typically low-pass limited with cut-off frequency of few hundred gigahertzes so that the obscuring material would have reasonable transmittance. The detectors used in passive imaging include, e.g., cryogenic bolometers [30], [31], [32], kinetic inductance detectors [33], or square-law detectors [34]. The detectors in passive imaging are designed to be wide-band, and the detector is often directly connected to terminal of a wide-band antenna. Antenna-coupled microbolometers used in the imaging system described in [31] are discussed more in Chapter 6 and references [VIII], [IX].

In coherent active imaging (Figure 2-2 b), the receiver noise bandwidth is much narrower than in incoherent passive imaging, and the thermal noise from the target and surroundings have insignificant effect on the image. The image resembles mostly the reflectivity of the target. The transmission through the obscuring material is a complex process, and it depends on both the dielectric properties of the material as well as thickness and surface structure of the bulk. When the surface of the material is smooth, i.e., the surface roughness is much smaller than the wavelength, a specular reflection according to Fresnel's law occurs and transmission through material is free of scattering. When the wavelength is of the same order as the surface roughness, reflection from the target becomes more diffuse in nature. The diffuse reflection manifests itself in image artifacts typically in active narrow-band imaging, where it is called speckle [35], [36]. The reflectivity of that kind of materials cannot be predicted based on the known dielectric material parameters, rather than it is a sample-specific property depending on the internal structure. E.g., a smooth target with underlying material discontinuities may appear distorted in the image. In active imaging, the target is illuminated mostly from one direction only, and part of the target is always shadowed. Both spatial and frequency diversity in the illumination are used to reduce the effect of the narrow bandwidth [37], [38], [39]. Speckle is insignificant in wide-band passive imaging, since it utilizes "self-illuminating" targets and wide-band, incoherent signals. Also, shadowing is much less a problem in passive imaging.

In addition to the advantages mentioned above, passive imaging is often preferred since the power detection of thermal radiation is in principle simpler than using coherent receivers with down conversion and detection of the baseband signal. However, as the image is defined by the apparent brightness temperature (2.3), it is possible that the target does not have any contrast with its background, i.e., $T_\mathrm{T} \approx T_\mathrm{B}$. With this condition, the target is not detected at all. In addition, varying brightness temperature in the surroundings may result in varying appearance of images of similar targets. It is suggested that brightness temperature resolution of 1 K is required in order to discern typical details in passive indoor imaging [40].

In coherent active imaging, it is possible to detect targets by the reflectivity difference, or if ranging capability is available, by the actual three-dimensional shape of the target [41]. Another advantage of active imaging is the high dynamic range, which is a system-dependent property rather than fundamentally limited, as in passive imaging [39], [28]. Active imaging is often more complex process than passive, since generation of millimeter-/submillimeter-wave power and preferably coherent detection is needed. Coherent detection typically involves reference signal and possibly multiple intermediate-frequency stages are needed prior base-band detection, whereas direct detection can be used in passive imaging [42]. Despite of great effort to miniaturize the heterodyne receivers and adapt them to conventional fabrication processes, such as in

[43], [44], and [45], they are bulky and relatively expensive. Typically the detector count in coherent active imager is therefore limited to a few.

2. 3 Focusing in submillimeter-wave imaging

In imaging, the frame rate and signal-to-noise ratio are contradictory qualities. As the frame rate is increased, the integration time per pixel, τ, naturally decreases. The signal-to-noise ratio in an imaging system is

$$\mathrm{SNR} \propto \sqrt{\tau} = \sqrt{\frac{N_{\mathrm{d}}}{N_{\mathrm{P}} f_{\mathrm{r}}}}, \tag{2.5}$$

where N_{d} is the number of detectors, N_{P} is the number of pixels in the image, and f_{r} is the frame rate. In current imaging systems, the number of detectors is typically smaller than the number of pixels and the integration time is limited due to the need to scan the detectors to form the image. The ideal case would be to have a detector per each pixel in the imaging system.

As discussed in the previous section, especially in case of coherent active receivers, large arrays to count for each pixel in the image are not available at submillimeter waves. Several source-detector arrangements have been suggested for submillimeter-wave imaging, and three examples are seen in Figure 2-3. In a single receiver/transceiver – system (Figure 2-3 a), the image formation is entirely a mechanical process, where focusing element, lens or a mirror, or the target is moved for each pixel. The first submillimeter-wave images, and many others, were obtained in this manner [46]. The coherent active imager in [8] has only one transceiver based on FMCW submillimeter-wave radar. The image is formed by actuating a subreflector in an offset reflector system. Effort to combine an array of a few transceivers into the imager is described in [45].

2. 3. 1 Focal plane arrays

A focal plane array (FPA) is depicted in Figure 2-3 b). There, the focusing element is stationary and each receiver corresponds to a pixel in the image. FPA is directly adapted from the conventional camera technology, and it has been applied especially in incoherent passive imaging at millimeter waves [47]. Passive submillimeter-wave imagers can have pixel count from thousands to tens of thousands. The system described in [48] has a linear array of 128 bolometers and that in [32] has 20 bolometers in a circular arrangement at the focal plane. Those imagers are combinations of the scanned and FPA designs, since both of the systems use dedicated fast-rotating mirrors to deviate the ensemble of detector beams across the field-of-view (FoV). A 700-1100 GHz FPA with 1024 power detectors has been described in [49], [50]. The FPA is located on the back side of a 15-mm hyper-hemispherical silicon lens and the detectors are fabricated based on the conventional CMOS technology.

The major issues in constructing FPA are the strict requirements for detector spacing as well as the complexity of the readout and biasing circuitry. At submillimeter waves, the realized FPAs use direct detection receivers only. The fundamental limitations with FPAs are related to the f-number of the system [51]. The f-number is the geometrical ratio of the diameter and the focal length of the focusing element

$$f\# = \frac{F}{D}, \tag{2.6}$$

where F is the focal length and D is the diameter of the focusing element (Figure 2-3 b). For convenience, small f-number is preferred, since it results in compact-size imaging systems. If f-number is small, the detectors can have wide beamwidth. The detectors can be small and they can be closely packed. However, focusing elements with small f-number may be complex as they may be assembled together from several components. Also, the FoV may be limited due to the increasing beam degradation in directions far from boresight. For large f-numbers, the elements in the FPA are more directive, i.e., their size is larger and the elements must be more sparsely packed. In this case, the FPA might become impractically large. The focusing element in FPA can be either a lens or a mirror. Typically, the lens is preferred in millimeter-wave systems, since it provides straight-forward axial quasioptics, and it does not suffer from aperture shadowing, as in, e.g., folded Cassegrain-type systems. However, many materials with mechanical properties suitable for constructing focusing elements have high dielectric losses in the submillimeter-wavelength range [52], and all-reflective mirrors are used instead.

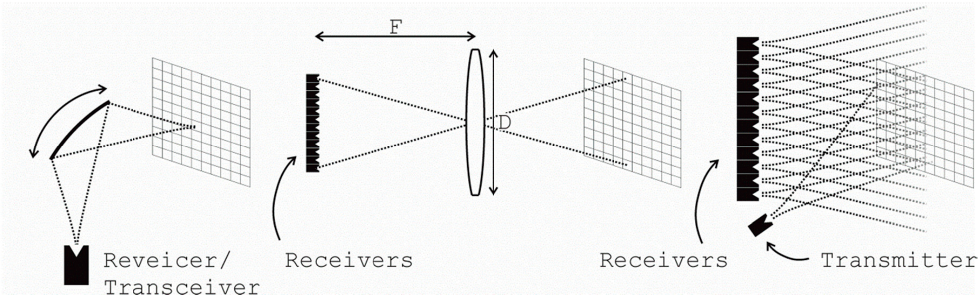

a) b) c)

Figure 2-3. Different types of imaging systems: a) a single receiver or transceiver is focused on the target and image is formed by scanning the focal point mechanically, b) an array of receivers is located in the focal plane of a focusing element, and image is the direct output of the detectors, and c) a non-focused array of receivers, that detect coherently the reflection from the target. The image is focused computationally in non-focused arrays.

2. 3. 2 *Non-focused arrays*

In a non-focused array in Figure 2-3 c, an array of detectors is used without the focusing element. Instead, focusing is a post-detection computational task. The wave reflected from the target must be detected coherently, so that both amplitude and phase information is acquired. In principle, non-focused array can be used both in active and passive imaging. However, coherent narrow-band detection of the thermal radiation is not possible with the achievable sensitivity of current detectors, and use of non-focused arrays is limited to coherent active systems. Omitting the focusing elements is an advantage, as focusing to the target is no longer fixed by the quasioptical design, but it can be chosen in the computational process. The focusing algorithms are based on Fourier techniques, such as the plane-to-plane transform with plane-wave spectrum [53], [I], [II] or the tomographic image reconstruction [54], [55], [56], [57].

In a non-focused array, typically an equi-spaced array of coherent detectors sample the field reflected from the target. Also, the elements in the array may be transceivers, so that the target is illuminated from multiple directions to reduce problems related to speckle, high specular reflections, and shadowing [37], [53]. For wide-band non-focused arrays, it is possible to achieve in-range resolution of

$$\Delta_r = \frac{c}{2B} = \frac{c\delta}{2}, \tag{2.7}$$

where c is the speed of light, B is the bandwidth of a frequency-swept system, and δ is the pulse width in a pulsed system. The FoV of non-focused array depends on the element spacing and the beamwidth of an individual element. A non-focused array can also form, e.g., a cylindrical surface, so that the target is enclosed by the array [58].

The receiver count and spacing in the non-focused array is selected so that a grating-lobe-free array factor results [59]. The array factor for a two-dimensional array lying in the x-y -plane is defined as

$$AF(k_x, k_y) = \sum_{m=0}^{N-1} a_m e^{-j\frac{2\pi}{\lambda}(ux_m + vy_m)}, \tag{2.8}$$

where a_m is an amplitude weight, and the directional cosines are $u = \sin\phi\cos\theta$ and $v = \sin\phi\sin\theta$. Since the exponent function has a period of 2π, the array factor repeats itself (in u-dimension) for every

$$u_n = u_0 + n\frac{d}{\lambda}, \tag{2.9}$$

where $-1 \le u_0 \le 1$, n is an integer number, and d is the array spacing. If $d = \lambda/2$, an array with main beam at $u = -1$ would have another beam to $u = 1$. In case of $d = \lambda$, the grating lobe appears at $u = \pm 1$ for boresight main beam. Typically, the element pattern in an array is designed so that the grating lobes are suppressed at large angles and sparser arrays than $d = \lambda/2$ can be used. In imaging, the required field-of-view is limited to less than the half space, and the grating-lobe-free spacing is

$$d = \frac{\lambda}{1 + \sin\theta_{\max}}, \tag{2.10}$$

where $\theta_{\max}$ is the greatest angle on the array from the FoV.

2. 3. 3 Simplifications to non-focused arrays

As coherent receivers are needed in non-focusing arrays, they are more complex than, e.g., the FPA with direct detectors. The complexity related to the coherent detectors can be avoided by using an indirect holographic method, where only direct detection receivers are needed. There, the coherent detection is achieved computationally with help of a reference wave. Indirect holographic method is discussed more in detail in Chapter 3 and in references [I], [II], and [III]. The receiver count in non-focused arrays is reduced by using techniques related to compressive sensing [60], [61], and interferometric methods [62], [63], [64], [65], [66]. These methods simplify the imaging system to some extent, since they have fewer detectors than there are pixels in the final image and the sampling of the wave reflected from the target is sparser than the grating-lobe-free case (2.10). However, both interferometric and compressive-sensing-based methods have handicaps, such as a limited FoV and reduced signal-to-noise ratio.

A sparse transceiver array has been developed at millimeter waves [67], [68]. There, instead of an equi-spaced array, the transmitters and receivers are arranged in clusters. The clusters have linear arrays of receivers and transmitters so that receivers are sparser in one dimension and transmitters are sparser in the other dimension, as is shown in Figure 2-4. Since the arrays are sparse, their beam patterns have grating lobes. The grating lobes are opposite so that the maxima of the transmitter array grating lobes coincide with the close-to-null pattern of the receiver array (Figure 2-5 a and b). The back-reflected energy does not couple to the receivers through the grating lobes, rather than through the convolution result of the two array factors, which is not much degraded compared to an array factor of a similar array with a grating-lobe-free spacing [69]. In [67], the selected array design resulted in more than 60-dB suppression of the grating lobes as well as 17-fold reduction in detector count compared to the full array.

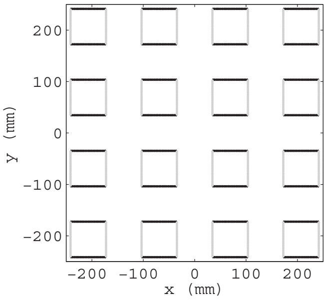

Figure 2-4. Sparse array geometry. Black horizontal lines represent the transmitters and grey vertical lines represent the receivers. Figure is repeated from [67].

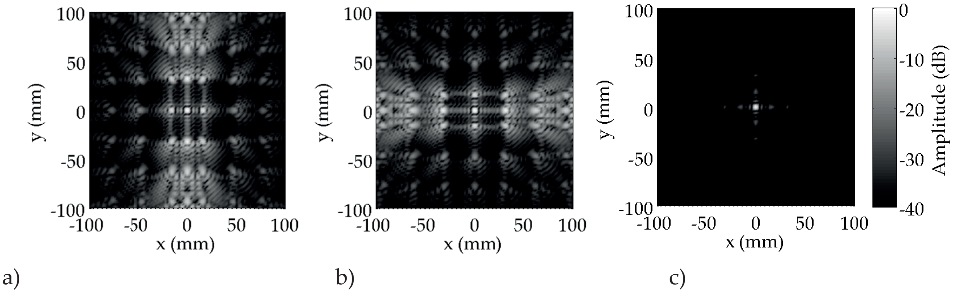

a) b) c)

Figure 2-5. The array factor for a) transmitter elements, b) receiver elements, and c) the two-way array factor. The patterns are repeated from [67].

The saving in cost by using only one transceiver and some benefits of the non-focused array can be combined in a reconfigurable reflectarray. There, an array with phase-shifting elements is used to modulate the incident wave in such a way, that the energy is reflected and refocused on the target. A lot of reflectarrays are realized with static phase shifting, up to 1000 GHz in [70]. When the reflection phase of each element in the reflectarray can be controlled, beam patterns can be created in a rapid fashion. The benefit of the reflectarray over, e.g., a phased array is that no distributing network, with likely high loss, is needed in order to feed the elements. The elements are fed quasioptically from a transceiver. Since only one transceiver is needed, the system is potentially cost efficient and the reflectarray can directly be a front end of, e.g., an elaborate radar system. A reconfigurable millimeter-wave reflectarray for imaging has been developed in [71]. There, pin-diodes are coupled to microstrip patch antennas so that when biased the re-radiated field has 180° phase shift compared to the non-biased condition. The reflectarray is used in a near-real-time imaging system.

The millimeter-wave reflectarrays are discussed in more detail in Chapter 4, and in references [IV], [72]. The development work presented here is about static reflectarrays, but the final goal is to achieve reconfigurability with MEMS-based phase shifters [73], [74]. Also, similar work has been done at submillimeter waves, and those reflectarrays are characterized in [75].

2. 4 Numerical methods

The numerical tools used in this work are the numerical computing environment MATLAB from MathWorks, [76], and the finite element method solver HFSS from Ansys Corporation, [77]. MATLAB is used for data processing, presenting the experimental data, and for numerical modeling of the radiation in indirect holographic imaging and reflectarrays. HFSS is used in full-wave simulations and optimization of the reflectarray antenna and phase shifter structures.

2. 4. 1 *Radiation from apertures*

In Chapter 4 and in reference [IV] radiation from apertures of reflectarrays is considered. The radiation is described by Maxwell's equations

$$\nabla \times \mathbf{E} = -j\omega\mu\mathbf{H} - \mathbf{J}_{\mathrm{m}}, \tag{2.11}$$

$$\nabla \times \mathbf{H} = j\omega\varepsilon\mathbf{E} - \mathbf{J}, \tag{2.12}$$

where $\mathbf{E}$ and $\mathbf{H}$ are the electric and magnetic fields, ε and μ are the dielectric permittivity and permeability, ω is the angular frequency of the time-harmonic field, and $\mathbf{J}$ and $\mathbf{J}_{\mathrm{m}}$ are the electric and magnetic current densities. According to Huygens' principle, an antenna can be enclosed by surface S, and the radiating antenna structure can be replaced by equivalent surface current densities, $\mathbf{J}_\mathrm{s}$ and $\mathbf{J}_\mathrm{ms}$, without changing the radiating field. In calculating the radiating properties of an antenna, the current densities are either solved from the electromagnetic theory for simple structures, or they are approximated with numerical methods for complex structures, where closed form expression cannot be found.

Following the pioneering work by Stratton and Chu [78], the current densities are induced by the incident electric and magnetic field:

$$\mathbf{J}_\mathrm{s} = \mathbf{n} \times \mathbf{H}, \tag{2.13}$$

$$\mathbf{J}_\mathrm{ms} = -\mathbf{n} \times \mathbf{E}, \tag{2.14}$$

where $\mathbf{n}$ is the surface normal of S. The radiating fields of the antenna are accurately derived from these current sources. To simplify, either (2.13) or (2.14) can be eliminated, and the other can be used in calculating the fields. If S is an infinite plane, as is convenient for aperture antennas, the other half space can be filled with either perfect electric or magnetic conductor. Then, $\mathbf{J}_\mathrm{s} = 0$ for the electric conductor and $\mathbf{J}_\mathrm{ms} = 0$ for the magnetic conductor. In case of electric conductor, surface currents become

$$\mathbf{J}_\mathrm{s} = 0, \tag{2.15}$$

$$\mathbf{J}_\mathrm{ms} = -2\mathbf{n} \times \mathbf{E}. \tag{2.16}$$

The electric field outside the plane S can be calculated with Green's function by integrating:

$$\mathbf{E}(\mathbf{r}) = -\oint_S \nabla G(\mathbf{r} - \mathbf{r}') \times \mathbf{J}_\mathrm{ms}(\mathbf{r}') dS', \tag{2.17}$$

where G is the scalar Green's function and dS' is the aperture surface differential element. The scalar Green's function is

$$G(\mathbf{r} - \mathbf{r}') = \frac{e^{-jk|\mathbf{r}-\mathbf{r}'|}}{4\pi|\mathbf{r} - \mathbf{r}'|}, \tag{2.18}$$

where $\mathbf{r}$ is location at the observation point and $\mathbf{r}'$ is location in plane S. In this work, the magnetic current density is $\mathbf{J}_\mathrm{ms} = -2\mathbf{u}_\mathrm{z} \times \mathrm{E}_a\mathbf{u}_\mathrm{y}$, i.e., the aperture normal is along the z-axis and the polarization of the electric field is assumed to be along the y-axis. The coordinate system is shown in Figure 2-6, where aperture is used to designate the area where most of the radiating field originates from, and screen is used to designate the rest of the plane S.

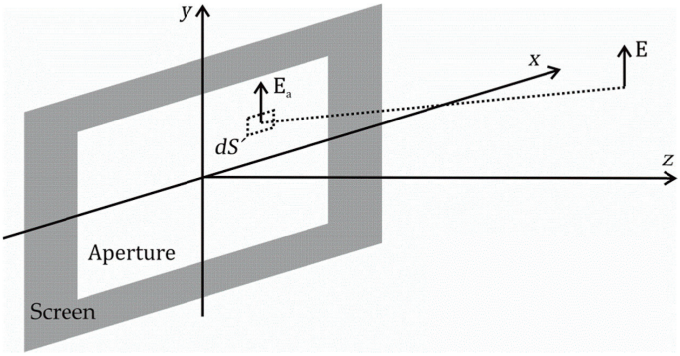

Figure 2-6. The geometry of planar aperture covered with plane S. The screen is assumed infinite and divides the half spaces.

The gradient of the scalar Green's function is

$$\nabla G(\mathbf{r}-\mathbf{r}') = \left(\frac{1}{R}+jk\right)\frac{e^{-jkR}}{4\pi R}\mathbf{u}_\rho, \tag{2.19}$$

where $R = |\mathbf{r}-\mathbf{r}'|$, and $\mathbf{u}_\rho = (\mathbf{r}-\mathbf{r}')/|\mathbf{r}-\mathbf{r}'|$. Integral (2.17) becomes

$$\mathbf{E}(\mathbf{r}) = \oint_S \left(\frac{1}{R}-jk\right)\frac{e^{-jkR}}{4\pi R}\mathbf{u}_\rho \times 2\mathbf{u}_z \times \mathrm{E}_a\mathbf{u}_y dS'. \tag{2.20}$$

The radial unit vector is written in Cartesian coordinates

$$\mathbf{u}_\rho = \sin\theta\cos\varphi\,\mathbf{u}_x + \sin\theta\sin\varphi\,\mathbf{u}_y + \cos\theta\,\mathbf{u}_z, \tag{2.21}$$

$$\mathbf{u}_\rho = \frac{x-x'}{R}\mathbf{u}_x + \frac{y-y'}{R}\mathbf{u}_y + \frac{z-z'}{R}\mathbf{u}_z, \tag{2.22}$$

where the dotted coordinates are in plane S. Substituting the Cartesian formulation in (2.20) results in

$$\mathbf{E}(\mathbf{r}) = \oint_S \mathrm{E}_a \frac{(1-jkR)e^{-jkR}}{2\pi R^3}\Big((y-y')\mathbf{u}_z - (z-z')\mathbf{u}_y\Big)\, dS'. \tag{2.23}$$

If the aperture is large compared to the wavelength, the electric field can be approximated to be non-zero in the aperture and zero elsewhere. In the approximation, plane S is finite, and integration (2.23) extends over the aperture of the antenna only.

2. 4. 2 Fourier optics

Fourier optics is dualistic with Huygens' Principle. In Huygens' principle, each infinitesimal surface element acts as a source of a spherical wave. Initial work on Fourier optics has been made by Ratcliffe [79]. In Fourier optics, space is regarded as sourceless and all that exists is an infinite number of plane wave modes. Fourier optics is discussed in detail in [80], [81]. The modes are solutions of the Helmholtz equation

$$\nabla\mathbf{E} + k^2\mathbf{E} = 0, \tag{2.24}$$

and they are of the form

$$\mathbf{E}_\mathrm{u}(x,y,z) = E_0 e^{-j(k_\mathrm{x}x+k_\mathrm{y}y)} e^{\pm jz\sqrt{k^2-{k_\mathrm{x}}^2-{k_\mathrm{y}}^2}}\mathbf{u}_\mathrm{y}, \tag{2.25}$$

where k_x and k_y are the x- and y-components of the wave vector and y-polarized field is considered. When $k^2 > {k_\mathrm{x}}^2 + {k_\mathrm{y}}^2$, the solutions represent propagating plane waves, and when $k^2 < {k_\mathrm{x}}^2 + {k_\mathrm{y}}^2$, they represent strongly attenuating solutions. The attenuating solutions are analogous to the evanescent waves. The "+" sign in (2.25) is related to propagation to the direction of the negative z-axis and the "−" sign to the positive axis. As with Huygens' principle, propagation is not considered in the direction of the negative z-axis, and "+" –solution is disregarded. As the solutions of the Helmholtz equation are separable, each polarization can be solved independently and similarly to (2.25).

Integrating the superposition of the plane waves gives the electric field in the Cartesian coordinates:

$$\mathbf{E}(x,y,\mathrm{z}) = \iint_{-\infty}^{\infty} \hat{\mathbf{E}}(k_\mathrm{x},k_\mathrm{y}) e^{-j(k_\mathrm{x}x+k_\mathrm{y}y)} e^{\pm jz\sqrt{k^2-{k_\mathrm{x}}^2-{k_\mathrm{y}}^2}}\, dk_\mathrm{x}dk_\mathrm{y}, \tag{2.26}$$

where $\hat{\mathbf{E}}(k_\mathrm{x},k_\mathrm{y})$ is the plane wave spectrum (PWS) of the electric field:

$$\hat{\mathbf{E}}(k_\mathrm{x},k_\mathrm{y}) = \iint_{-\infty}^{\infty} \mathbf{E}(x,y,\mathrm{z}=0) e^{j(k_\mathrm{x}x+k_\mathrm{y}y)}\, dxdy, \tag{2.27}$$

For simplicity, it is assumed that the PWS is calculated at $z = 0$. Integrals (2.26) and (2.27) have close resemblance to the Fourier transforms, and they are widely used in describing plane-to-plane propagation in antenna measurements [82] and imaging [53].

2. 4. 3 *Discrete plane wave spectrum*

Fourier optics is favored due to its direct application with the Fast Fourier transform, and hence efficient calculation. In the numerical implementation, a $M \times N$ point sampling grid over the aperture width W and height H is assumed. The electric field is defined in discrete coordinates:

$$x_\mathrm{m} = m\Delta x - W/2, \qquad m = 0 \ldots M-1, \tag{2.28}$$

$$y_\mathrm{n} = n\Delta y - H/2, \qquad n = 0 \ldots N-1, \tag{2.29}$$

where the spacing is $\Delta x = W/M - 1$ and $\Delta y = H/N - 1$. The discrete and finite PWS has spatial frequency spacing of

$$k_{\mathrm{x}_\mathrm{p}} = p\, 2\pi/\mathrm{W} - \pi/\Delta x, \qquad p = 0 \ldots M-1, \tag{2.30}$$

$$k_{\mathrm{y}_\mathrm{w}} = w\, 2\pi/\mathrm{H} - \pi/\Delta y, \qquad w = 0 \ldots N-1. \tag{2.31}$$

The transform pair (2.26) and (2.27) becomes

$$\mathbf{E}(x_\mathrm{m},y_\mathrm{n},\mathrm{z}) = \sum_{p=0}^{M-1}\sum_{w=0}^{N-1} \hat{\mathbf{E}}_\mathrm{u}\left(k_{\mathrm{x}_\mathrm{p}},k_{\mathrm{y}_\mathrm{w}}\right) e^{-j\left(k_{\mathrm{x}_\mathrm{p}}x_\mathrm{m}+k_{\mathrm{y}_\mathrm{w}}y_\mathrm{n}\right)} e^{\pm jz\sqrt{k^2-{k_{\mathrm{x}_\mathrm{p}}}^2-{k_{\mathrm{y}_\mathrm{w}}}^2}}, \tag{2.32}$$

$$\hat{\mathbf{E}}_{\mathrm{u}}\left(k_{\mathrm{x_p}},k_{\mathrm{y_w}}\right)=\sum_{m=0}^{M-1}\sum_{n=0}^{N-1}\mathbf{E}(x_{\mathrm{m}},y_{\mathrm{n}},\mathrm{z}=0)e^{j\left(k_{\mathrm{x_p}}x_{\mathrm{m}}+k_{\mathrm{y_w}}y_{\mathrm{n}}\right)}. \tag{2.33}$$

2. 5 Experimental methods

2. 5. 1 Near-field range

The experimental work discussed in Chapters 3, 4, and 5 involves a near-field range. The measurement range consists of a millimeter-wave vector network analyzer, AB Millimètre MVNA-8-350, with millimeter-/submillimeter-wave extensions, ESA-1-FC and ESA-2-FC. ESA-1-FC is the transmitter with Gunn-diode pumped frequency multiplier and ESA-2-FC is the receiver with Gunn-diode pumped sub-harmonic mixer [83]. The network analyzer is phase locked to a stabilized microwave source.

The vector measurements presented in this thesis are done at 120 GHz, 310 GHz, and 650 GHz. The typical maximum signal-to-noise ratio (SNR) in these measurements is 60 dB, 54 dB, and 37 dB, respectively. In case of the RCS range in Section 5. 3, the reflection is re-focused to the receiver, and the maximum SNR is 79 and 72 dB at 310 and 650 GHz, respectively. The uncertainty in amplitude and phase due to the electrical noise is [84]:

$$U_{\mathrm{gain}}=20\times\log\left(1\pm10^{\frac{-SNR}{20}}\right), \tag{2.34}$$

$$U_{\mathrm{phase}}=\tan^{-1}\left(\pm10^{\frac{-SNR}{20}}\right), \tag{2.35}$$

and they are listed in Table 2-2. The flange-to-flange SNR of the network analyzer is approximately 115-120 dB at 120 and 310 GHz [85], and at least 90 dB at 650 GHz.

Table 2-2. Amplitude and phase uncertainty in near-field measurements due to the electrical noise.

Frequency (GHz)	**SNR (dB)**	**Uncertainty**	
		Amplitude (dB)	Phase (°)
120	60	0.01	0.06
310	54	0.02	0.11
650	37	0.12	0.81

In the measurements presented in Chapters 3, 4, and 5, the receiver is placed on a planar near-field scanner, which carries out a planar raster scan in x-y -direction. The planar scanner used in the experiments is the millimeter-wave near-field scanner NSI 200V–5×5 from Nearfield Systems Inc. [86].

The scanner is intended for millimeter-wave measurements, but it is used up to 650 GHz. The mechanical inaccuracies in the scanner result in non-planar and non-equi-spaced sampling of the field. High accuracy is important especially in the direction of the wave propagation since in that case planarity error converts to phase error of the full 360° per wavelength. The planar wave fronts measured in Section 5. 2 are highly directed and propagation is strictly confined in to the normal from scan direction. The scanner is equipped with an active *z*-positioning system that compensates for the error. The planarity of the scanner is determined with a theodolite measurement, and the position of the receiver is corrected accordingly. In addition to the real-time position correction, the profile of the scanner after the correction is taken into account in the processing of the measurement data. The scanner profile after the position correction is measured with a laser tracker. The laser-tracker data are shown in Figure 2-7 a). In addition to the planarity error, also the *x*-*y* –position of the receiver is inaccurate and cannot be corrected reliably. However, the effect of this error does not typically couple as strongly to the measurement results as that of planarity error. The *x*-position error is shown in Figure 2-7 b).

In addition to the electrical noise and the mechanical inaccuracies in the planar scanner, drift and bending of the connecting cables affect especially the phase measurement accuracy. The drift becomes an issue with long data-acquisition times. The drift affects mostly phase measurement, and it can be compensated by a fast one-dimensional tie scan. The tie scan provides a phase reference across the scanning area, and the slow two-dimensional measurement is compensated based on it [14]. The cable providing the microwave local oscillator signal to the remote receiver on the moving planar scanner bends, and introduces phase error due to the change in its electrical length. Phase error due to bending is counteracted with a real-time system measuring the electrical length of the cable with a pilot signal [87]. In [85], phase error reduction is reported to be from 85° to less than 5° in a 0.5-m raster scan at 310 GHz, when the pilot-signal correction is applied. The pilot-signal correction is used in 310- and 650-GHz quiet-zone measurements presented in Section 5. 2.

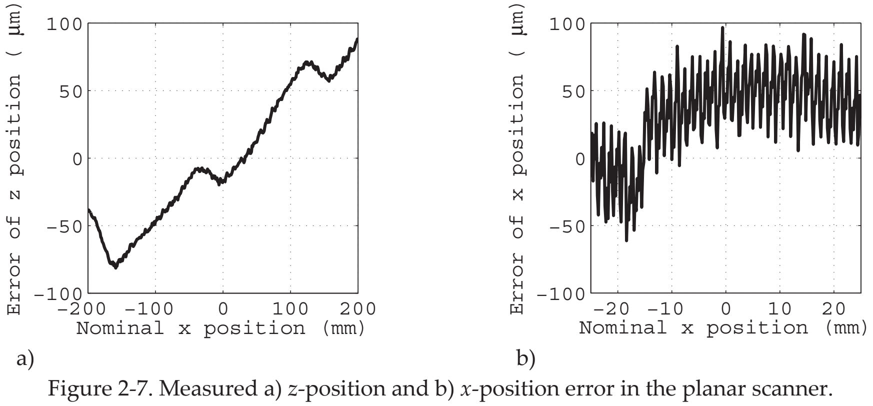

Figure 2-7. Measured a) *z*-position and b) *x*-position error in the planar scanner.

In near-field measurements in Chapter 4, the radiating field is typically measured with an open-ended waveguide as the near-field probe. Probe correction is used to compensate the reduced directivity at high incident angles. The approximate numerical models for open-ended waveguide probe are described in [88] and they have since become standard models in near-field probing [89]. The probe correction is included in the near-field measurements of the reflectarrays, and it takes into account the co-polar directivity of the probe. The directivity is also determined from full-wave simulation with a realistic model of the probe, and it follows accurately that one presented in [88].

2. 5. 2 Power-measurement range

In Chapter 6, the bolometers and the ad hoc power detector are characterized in an antenna measurement setup at room temperature. The setup consists of a backward-wave oscillator (BWO) as the source, differential and lock-in amplifier chain, and a quasi-optical power meter as is shown in Figure 2-8. Due to the insensitivity of the bolometers at room temperature, high output power of the BWO is required. The BWOs have an over-sized output waveguide connected to an over-sized horn antenna.

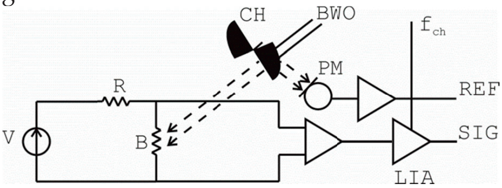

Figure 2-8. The power measurement setup. V = isolated voltage source, R = shunt resistor, B = bolometer, CH = chopper, f_{ch} = chopping frequency, LIA = lock-in amplifier, BWO = backward-wave oscillator, PM = power meter, REF = signal relative to the output power of the BWO, and SIG = voltage over the bolometer at 20 Hz.

Due to the inherent properties of the BWOs, their output power and polarization vary rapidly as a function of frequency [90]. Both stability measurement and frequency sweep of a BWO are shown in Figure 2-9. After warm-up time of less than five minutes, the output power drifts about 0.1 dB. Rate of the power drift can be up to ±0.3 dB per hour. Also, the output power of the BWO varies of the order of ±3 dB per 100 MHz. A quasioptical power meter, from Thomas Keating Ltd. [91], is used to find optimum output power and compensate for drift in real time.

In order to reduce the noise in the detected signal, the illumination from the BWO is chopped and detected at 20 Hz. The bolometers are biased from an isolated voltage source SIM928 and lock-in amplifier SR830 is used in read out – both from Stanford Research Systems Inc. [92].

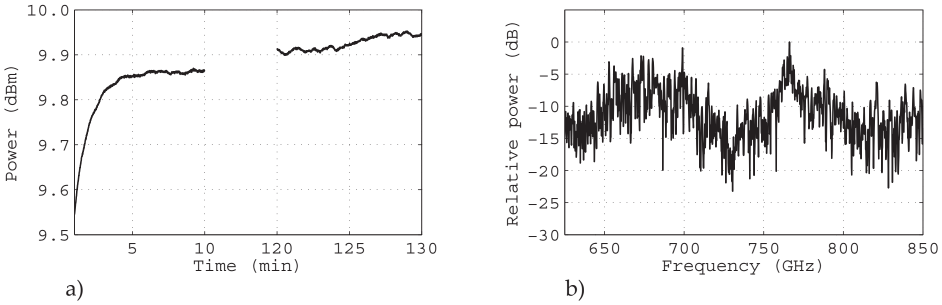

a)

b)

Figure 2-9. Behaviour of BWO output power a) during 130 minutes, and b) when frequency is swept from 625 to 850 GHz.

3 Holographic imaging methods

The term holography is used to describe a process of storing phase information of a target wave into an interference pattern, a hologram. The phase information could be retrieved by applying original reference wave, which was used in recording the hologram. The idea of holography was invented by Gabor [93], and it was further developed by Leith and Upatnieks [94]. Later, the term has been used to refer to imaging methods where the phase information of the target wave is recorded directly, i.e., the reference wave is the electrical reference associated to base-band detection in any phase-coherent radio system. Often, term *holographic imaging* is used to refer to methods involving computational focusing by a plane-to-plane transform with PWS [95], [96].

The imaging method presented in [97], [98], [99], [100], [I], [II], and [III] and discussed in this chapter follow the original definition of holography as is presented in [93] and [94]. Here, the method is called *indirect holographic imaging*, as the phase information is retrieved from a hologram and not measured directly.

3. 1 Indirect holographic imaging

Phase retrieval is a technique where the phase of electric field is determined indirectly from amplitude measurement. Phase retrieval has been widely used in antenna diagnostics. It is used in situations where direct measurement of phase is not possible or when the direct phase measurement uncertainty is greater than what is expected from phase retrieval. The phase of the electric field is typically obtained from multiple amplitude measurements or by using a reference wave [101], [98]. In work presented here, phase retrieval is applied in indirect holographic imaging. Without direct measurement of the phase, the method allows for significantly reduced complexity compared to, e.g., transceiver arrays.

Figure 3-1 illustrates the geometry of indirect holographic imaging. There, the aperture of a detector array (scanned receiver is used in experiments) is illuminated with an offset reference wave $\mathbf{E}_\mathrm{R}$. The target is illuminated coherently from the same source at the same polarization. The back-reflected wave, the target wave $\mathbf{E}_\mathrm{T}$, forms an interference pattern with the reference wave at the detector array

$$I = |\mathbf{E}_\mathrm{R} + \mathbf{E}_\mathrm{T}|^2. \tag{3.1}$$

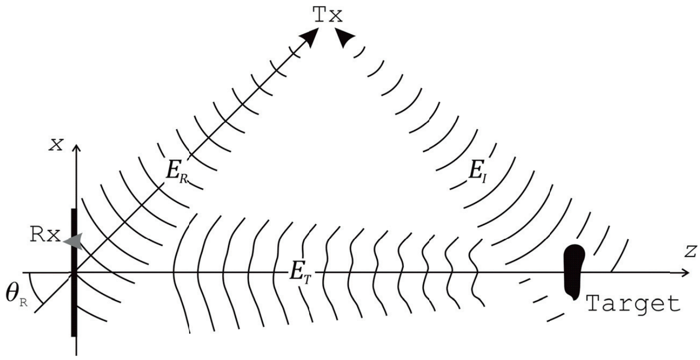

Figure 3-1. Indirect holographic imaging. The transmitter power is divided in to reference and illumination waves. The interference pattern of the reference and target waves is measured at the aperture.

3. 1. 1 Fourier-domain technique

When co-polar electric field are assumed and the vector notation is omitted, the power density of the interference pattern can be written as

$$I = |E_\mathrm{R}|^2 + |E_\mathrm{T}|^2 + E_\mathrm{R}\overline{E_\mathrm{T}} + E_\mathrm{T}\overline{E_\mathrm{R}}. \tag{3.2}$$

Where $\overline{E_\mathrm{T}}$ and $\overline{E_\mathrm{R}}$ are the complex conjugates of the target and reference waves. Several methods can be used to retrieve the target wave. In offset holography, the reference wave is applied in a sufficiently large reference angle

$$\theta_\mathrm{R} = \tan^{-1}\frac{x_\mathrm{R}}{z_\mathrm{R}}, \tag{3.3}$$

where x_R and z_R are the coordinates of the reference feed. A corrugated horn antenna is used and its directional pattern is approximated based on the fundamental Gaussian beam mode. For simplicity, the reference feed is assumed to be in *x-z* –plane, i.e., $y_R = 0$. Rewriting (3.2) gives:

$$I(x,y) = |E_\mathrm{R}|^2 + |E_\mathrm{T}|^2 + 2|E_\mathrm{R}E_\mathrm{T}|\cos(\varphi_\mathrm{R} - \varphi_\mathrm{T}), \tag{3.4}$$

where phase of the reference wave is

$$\varphi_\mathrm{R}(x,y) = k\sqrt{(x-x_\mathrm{R})^2 + (y-y_\mathrm{R})^2 + {z_\mathrm{R}}^2}, \tag{3.5}$$

and φ_T is the phase of the target wave. In the original idea of offset holography, the reference wave is approximated as a plane wave. Then the phase of the reference wave becomes

$$\varphi_\mathrm{R}(x,y) = k\sin\theta_\mathrm{R}\,x, \tag{3.6}$$

In Fourier domain, the interference pattern (3.2) becomes

$$\hat{I} = \mathcal{F}|E_\mathrm{R}|^2 + \mathcal{F}|E_\mathrm{T}|^2 + \mathcal{F}E_\mathrm{R} * \mathcal{F}\overline{E_\mathrm{T}} + \mathcal{F}E_\mathrm{T} * \mathcal{F}\overline{E_\mathrm{R}}, \tag{3.7}$$

where operators $\mathcal{F}$ and $*$ are the Fourier transform and convolution. The last two convolutions in (3.7) are centered at spatial frequency of

$$u_{\mathrm{R}} = \pm k \sin \theta_{\mathrm{R}} / 2\pi, \tag{3.8}$$

in case of a planar reference wave. With a spherical reference wave, the spectral content of the reference wave depends on the location of the feed and the size of the hologram. Generally, the spectral content of a spherical reference wave is over the same spatial frequency as in case of the planar reference wave. A close-up example of a measured interference pattern and its spatial spectrum are shown in Figure 3-2. The measurement is carried out by a 2-dimensional raster scan in the x-y –plane.

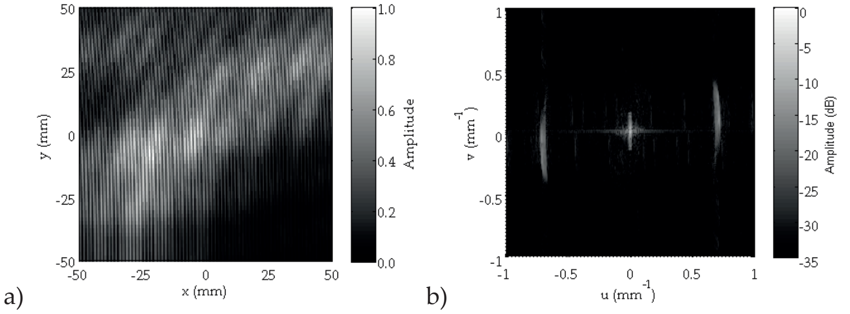

Figure 3-2. a) A close-up of a 310-GHz interference pattern. Due to offset reference wave, interference pattern has high spatial frequency component. b) Spatial spectrum of the interference pattern. The convolution terms of (3.7) are located at spatial frequency of $u \approx \pm 0.7$ mm^{-1}.

Finally, the convolution term in (3.7) is computationally band-pass filtered and the target field is retrieved:

$$E_{\mathrm{T}} = \frac{\mathcal{F}^{-1}(\mathcal{F}E_{\mathrm{T}} * \mathcal{F}\overline{E_{\mathrm{R}}})}{\overline{E_{\mathrm{R}}}}, \tag{3.9}$$

where $\mathcal{F}^{-1}$ is the inverse Fourier transform. The Fourier-domain technique is used in [I] and [II].

3. 1. 2 Spatial-domain technique

In [III], the target field is retrieved from hologram without Fourier transforms and filtering. The method involves additional measurement of the target-field power density:

$$|E_{\mathrm{T}}|^2 = \mathrm{Re}(E_{\mathrm{T}})^2 + \mathrm{Im}(E_{\mathrm{T}})^2, \tag{3.10}$$

The real part of the target wave can be written as

$$\mathrm{Re}(E_{\mathrm{T}}) = \pm\sqrt{|E_{\mathrm{T}}|^2 - \mathrm{Im}(E_{\mathrm{T}})^2}, \tag{3.11}$$

and inserted in to the interference pattern (3.2):

$$I = |E_{\mathrm{T}}|^2 + |E_{\mathrm{R}}|^2 + 2\left(\pm\mathrm{Re}(E_{\mathrm{R}})\sqrt{|E_{\mathrm{T}}|^2 - \mathrm{Im}(E_{\mathrm{T}})^2} + \mathrm{Im}(E_{\mathrm{R}})\mathrm{Im}(E_{\mathrm{T}})\right). \tag{3.12}$$

After shortening $C = I - |E_{\mathrm{T}}|^2 - |E_{\mathrm{R}}|^2$ and re-arranging

$$C - 2\mathrm{Im}(E_{\mathrm{R}})\mathrm{Im}(E_{\mathrm{T}}) = \pm 2\mathrm{Re}(E_{\mathrm{R}})\sqrt{|E_{\mathrm{T}}|^2 - \mathrm{Im}(E_{\mathrm{T}})^2}, \tag{3.13}$$

$$C^2 - 4C\mathrm{Im}(E_\mathrm{R})\mathrm{Im}(E_\mathrm{T}) + 4\mathrm{Im}(E_\mathrm{R})^2\mathrm{Im}(E_\mathrm{T})^2 = 4\mathrm{Re}(E_\mathrm{R})^2(|E_\mathrm{T}|^2 - \mathrm{Im}(E_\mathrm{T})^2), \tag{3.14}$$

$$4\mathrm{Re}(E_\mathrm{R})^2\mathrm{Im}(E_\mathrm{T})^2 - 4C\mathrm{Im}(E_\mathrm{R})\mathrm{Im}(E_\mathrm{T}) - 4\mathrm{Re}(E_\mathrm{R})^2|E_\mathrm{T}|^2 + C^2 = 0. \tag{3.15}$$

The imaginary part of the target wave can be solved from the quadratic equation (3.15):

$$\mathrm{Im}(E_\mathrm{T}) = \frac{C\mathrm{Im}(E_\mathrm{R}) \pm \sqrt{\left(C\mathrm{Im}(E_\mathrm{R})\right)^2 + \mathrm{Re}(E_\mathrm{R})^2(4\mathrm{Re}(E_\mathrm{R})^2|E_\mathrm{T}|^2 - C^2)}}{2\mathrm{Re}(E_\mathrm{R})^2}. \tag{3.16}$$

The target wave is retrieved by calculating the imaginary and real parts (3.11) and (3.16), and it is free from the limitations to the reference feed location, since no separation in spatial frequency domain is needed. The sampling of the hologram must be done according to the extent of the target, which leads to reduced number of required sample points compared to the Fourier-domain technique. The method is verified with experimental data at 310 GHz in [III].

3. 1. 3 Holography and compressive sensing

On-axis holography, or Gabor holography, involves zero reference angle, i.e., the feed illuminating the target is behind it (Figure 3-3). The target is partly transparent and the reference and target wave originate from the same feed. The advantage of on-axis holography is that the sampling interval is smaller than in case of an offset reference wave. Disadvantage of on-axis holography is that the terms in the spatial spectrum (3.7) are overlapping and only the component of the reference wave, $\mathcal{F}|E_\mathrm{R}|^2$, can be subtracted from it directly. In compressive holography presented elsewhere in literature, the target is retrieved from an on-axis hologram [102], [103]. The method involves an algorithm, which correlates the hologram with diffracted fields from different target planes. The target contributes only to the plane it lies in, which enables in-range resolution. Since the power density term, $|E_\mathrm{T}|^2$, contains no phase information, its contribution to any focus plane is minimal, i.e., diffraction from any focus plane does not correlate with $|E_\mathrm{T}|^2$. Similarly, the conjugate term $E_\mathrm{R}\overline{E_\mathrm{T}}$, or mirror image, correlates with diffraction from the negative z-axis, and is suppressed from images with $z > 0$. In conventional offset holography, the targets outside the focus plane appear as a blurred contribution in the images. In-range resolution can only be achieved with frequency-swept systems, such as that in [95]. Compressive on-axis holography has been experimentally verified in [61] at 94 GHz. In addition to compressive target retrieval, the sample count was reduced to less than half of the Nyqvist requirement with only modest reduction in image quality. The computational burden of the algorithm used in compressive holography is not discussed in [61]. However, the algorithm is iterative, and especially the retrieval of large images may be computationally heavy.

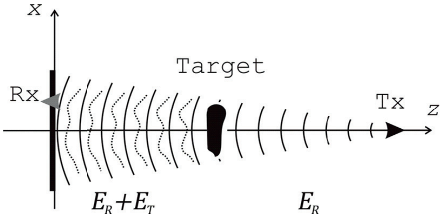

Figure 3-3. On-axis holographic setup.

3. 1. 4 Indirect holographic imaging experiment

In [I], the indirect holographic method with spherical reference wave is experimentally verified for the first time at 310 GHz. Figure 3-4 shows the setup. A corrugated horn antenna is used as the reference feed. In offset holography, the reference wave must be known. In [I] and [II], a semi-empirical reference wave is used: the amplitude is measured and the phase is calculated from (3.5). For distortion-free image, the location of the phase center of the reference feed must be known. In practice, it is possible to position the reference feed with accuracy of the order of 1 mm (~1 λ in experiments in [I] and [III]). For better accuracy, the reference phase may be measured and modeled with a least squares fit to (3.5).

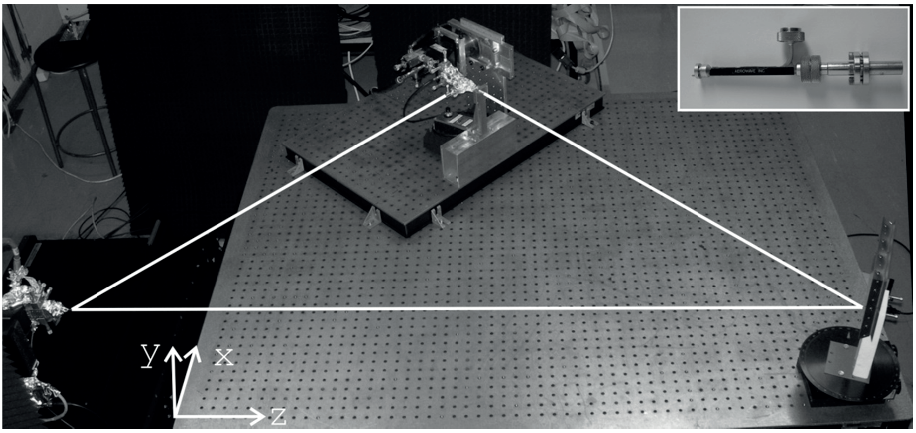

Figure 3-4. The indirect holographic setup. The target in located in the lower right corner, the transmitter is located in the center at top, and the receiver on the planar scanner in the lower left corner. The reference and illumination waves are divided with a directional coupler (shown in the inset) from the source.

3. 1. 5 Sources of error

Compared to those imaging methods with direct measurement of the phase, the difference in the assumed and true position of the reference feed contributes for an additional error. Also, successful target wave retrieval sets restrictions on the reference wave incident angle.

3. 1. 5. 1 Error due to reference feed position

The error between the actual and modeled reference feed position, ($x_{\mathrm{R,M}}$, $y_{\mathrm{R,M}}$, $z_{\mathrm{R,M}}$), leads to an erroneous target wave:

$$E_{\mathrm{T,M}} = \frac{E_{\mathrm{T}}\overline{E_{\mathrm{R}}}}{\overline{E_{\mathrm{R,M}}}}, \tag{3.17}$$

where $E_{\mathrm{R,M}}$ is the modeled reference wave:

$$E_{\mathrm{R,M}} = A_{\mathrm{R}} e^{-jk\sqrt{\left(x-x_{\mathrm{R,M}}\right)^2+\left(y-y_{\mathrm{R,M}}\right)^2+z_{\mathrm{R,M}}{}^2}}, \tag{3.18}$$

and the target wave becomes

$$E_{\mathrm{T,M}} = E_{\mathrm{T}} e^{jk\varphi_M}, \tag{3.19}$$

where φ_M is the phase error due to modelled reference wave:

$$\varphi_M = k\left(\sqrt{(x-x_{\mathrm{R}})^2+(y-y_{\mathrm{R}})^2+z_{\mathrm{R}}{}^2} - \sqrt{\left(x-x_{\mathrm{R,M}}\right)^2+\left(y-y_{\mathrm{R,M}}\right)^2+z_{\mathrm{R,M}}{}^2}\right). \tag{3.20}$$

Figure 3-5 shows the normalized phase error resulting from 3-λ error in the modeled location of the reference feed in case of the geometry in the experiment in [I]. The error is normalized to the center of the hologram, since a constant phase error does not affect the image. The phase errors are slightly curved tilted surfaces. Depending whether the feed is dislocated in *x*-, *y*-, or *z*-coordinate, the tilt is 227°, 428°, and 210°, respectively. The curvature of the surfaces results in deviation from plane by 27°, 29°, and 12°, respectively. As the phase error is mainly planar, the error in the reference wave model leads to mainly a shift in the apparent position of the target instead of loss in the image quality otherwise. As such, the indirect holographic method is robust against the errors due to misalignment of the reference feed, and if needed, the position of the feed can be recalibrated with, e.g., a point-like calibration target.

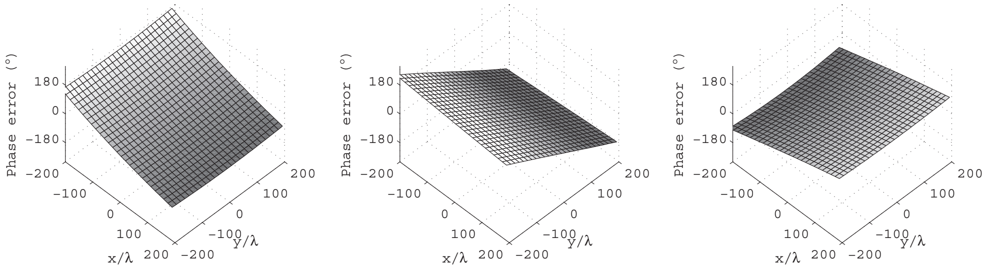

a) b) c)

Figure 3-5. The target wave phase error. The error to the actual reference feed location is 3 λ in a) *x*-, b) *y*-, and c) *z*-coordinate.

3. 1. 5. 2 Restrictions on the reference wave

In offset holography, a sufficiently large reference angle is needed for successful band-pass filtering of the target wave [94]. The critical wave number related to the reference angle is

$$k_{\mathrm{crit}} = \max(2B_{\mathrm{T}}, 2B_{\mathrm{R}}) + B_{\mathrm{T}} + B_{\mathrm{R}}, \tag{3.21}$$

where B_{T} and B_{R} are the bandwidth of the target and reference wave. The bandwidth of the target is

$$B_{\mathrm{T}} = k\frac{D_{\mathrm{H}} + D_{\mathrm{T}}}{\sqrt{\left(\frac{D_{\mathrm{H}} + D_{\mathrm{T}}}{2}\right)^2 + {z_{\mathrm{T}}}^2}}, \tag{3.22}$$

where D_{H} and D_{T} are the dimensions of the hologram and target and z_{T} is the distance from the hologram to the target. A planar reference wave is used in [98], [99], and B_{R} approaches zeros. The spherical reference wave has significant bandwidth:

$$B_{\mathrm{R}} = k\left(\frac{D_{\mathrm{H}}/2 + |x_{\mathrm{R}}|}{\sqrt{(D_{\mathrm{H}}/2 + |x_{\mathrm{R}}|)^2 + {z_{\mathrm{R}}}^2}} - \frac{D_{\mathrm{H}}/2 - |x_{\mathrm{R}}|}{\sqrt{(D_{\mathrm{H}}/2 - |x_{\mathrm{R}}|)^2 + {z_{\mathrm{R}}}^2}}\right). \tag{3.23}$$

From (3.21)-(3.23), it results that the greater the bandwidths, the greater the critical wavenumber is. As a consequence, the closer to the hologram the target and reference feed are, the greater reference angle is needed. Also, the reference angle increases as the target and hologram dimensions increase. The condition is limiting both the field of view and the cross-range resolution in indirect holographic imaging, since both hologram and target size are constrained.

3. 1. 6 Coarse sampling

The offset reference wave defines the required spatial sampling interval in the hologram, if Nyqvist sampling is enforced. The sampling criterion of the hologram is suggested to be relaxed by coarse sampling [104]. There, it is shown that the Nyqvist sampling is required according to the target wave and not according to the reference wave. As a result of coarse sampling, the spatial spectrum (3.7) is aliased, but the aliased content is not overlapping with the convolution terms and target wave retrieval is possible. In case of a planar reference wave, coarse sampling allows for sample spacing reduction in ratio of

$$R_{\mathrm{R}} = \frac{\sin\theta_{\mathrm{R}}}{2\sin\theta_{\mathrm{T_{max}}}}, \tag{3.24}$$

where $\theta_{\mathrm{T_{max}}}$ is the maximum angular extent of the target. The coarse sampling involves rather elaborate selection of sampling and limitations to the target geometry, and the method has not yet been experimentally verified. The requirements for the reference wave angle do not exist in the spatial-domain technique introduced in [III], and there, sampling of the hologram can be done directly according to the maximum extent of the target, $\theta_{\mathrm{T_{max}}}$. Compared to the Fourier-domain technique, the sampling requirement is relaxed by factor R_{R} in the spatial-domain technique.

3. 2 Image quality considerations

In literature, the millimeter-/submillimeter-wave image quality is typically estimated based on the subjective experience, e.g., on how much details of the target are discernible in the image. Few references, such as [31], [40], [39], [105], and [106] assess the image quality also in quantitative means. In [II], the images are assessed based on their spatial resolution, noise, and contrast. The standardized image-quality metrics enable fair comparison between different imaging systems.

3. 2. 1 Test targets

Laser-cut test targets have been fabricated for image quality evaluation in the experiment [II]. The targets are made of 100-µm thick stainless steel sheets and they are tensioned on PVC frames. Both a 1.5-times scale-up of the USAF 1951 resolution test target [107] and a knife-edge target are used. Figure 3-6 shows the targets. USAF 1951 is a collection of horizontal and vertical rectangular openings cut to the sheet, and their size ranges from 1.5 × 0.4 mm^2 to 20 × 4 mm^2. The knife-edge target has a 140-mm long edge suspended in the air.

The images in the experiment are focused to the target distance of $z_T = 1.53$ m by using the Fourier-optics-based transforms (2.32)-(2.33). The 310-GHz image of the USAF 1951 is repeated from [II] in Figure 3-7. Due to the illumination from one source at a point frequency only, the highly reflective flat target must be oriented optimally for successful imaging. However, purpose of this work is to evaluate the holographic imaging, and for that a single source is sufficient. For non-optimally positioned targets, spatial and frequency diversity is needed for high-quality images [37], [39].

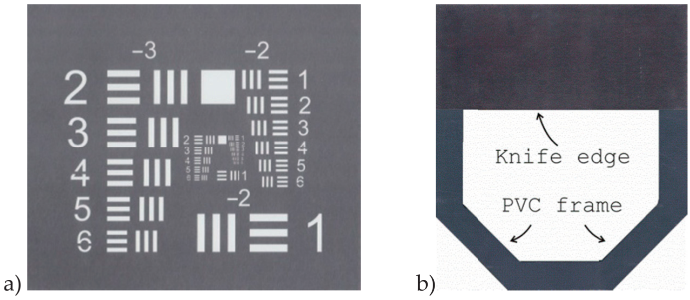

Figure 3-6. Test targets made of 100-mm stainless steel sheets. a) 1.5-times scale-up of the USAF 1951 resolution test target and b) the knife-edge target. Both targets are tensioned on a solid PVC frame to ensure flatness.

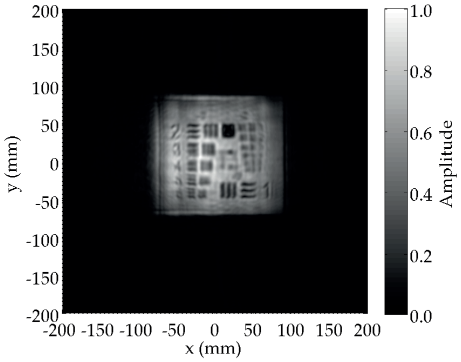

Figure 3-7. 310-GHz image of the USAF 1951 resolution test target. The target wave amplitude is normalized to the maximum at the target distance. The figure is produced with the color map option "gray" and shading option "interp" in MATLAB.

3. 2. 2 Point spread function

The point spread function (PSF) is the spatial impulse response of the imaging system and/or the computational processing of the image. It describes how a point target appears in the image. Due to the finite aperture, the PSF follows typically either the sinc or Bessel function for rectangular or circular apertures, respectively. In passive incoherent imaging, the PSF is estimated as a Gaussian function [51]. An analogous approach to the imaging system response can be presented in terms of the radiation properties of an antenna, such as beamwidth and sidelobe level. However, since imaging is typically a near-field process, antenna terminology is ill-suited. Also, rather than in angular domain, PSF is typically defined in the spatial domain suitable for Fourier optics in the Cartesian presentation.

3. 2. 2. 1 Slanted-edge method

The point-like targets are difficult to measure due to SNR limitations at millimeter- and submillimeter-wave range. In the experiment in [VI], the knife edge target is used to provide a strong reflection and high-SNR image. The slanted-edge method provides a one-dimensional estimate of the PSF, the line spread function (LSF). The knife edge is slightly tilted in order to super-sample it (Figure 3-8). The cut over the edge is called the edge spread function (ESF), and LSF is

$$\mathrm{LSF} = \frac{d}{dn}\mathrm{ESF}, \tag{3.25}$$

where the derivation is taken in the direction of the edge normal in the image plane.

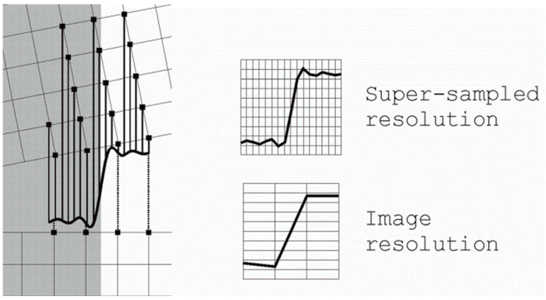

Figure 3-8. Super-sampling in the slanted-edge method. When the edge (grey) is tilted with respect to the image pixel grid, the pixel locations are distributed denser over the edge than in case of edge parallel to the pixels.

The cross-range resolution is given by the half-power beamwidth of the PSF. The estimated resolution of the PSF is repeated from [II] in Table 3-1. Compared to the theoretical half-power width of the PSF, that from the indirect holographic experiment is 15-30% larger. The resolution is better in case of the vertical edge. Since the used polarization is also vertical, the improved resolution can be explained by the stronger scattering from edges parallel to the polarization [24].

Table 3-1. The theoretical and estimated point spread function and resolution in the imaging experiment in [II].

Point spread function	**Half-power width at 1.53 m (mm)**	**Resolution (°)**
Theoretical	3.3	0.14
Vertical LSF estimate	3.8	0.17
Horizontal LSF estimate	4.3	0.18

3. 2. 3 Signal-to-noise ratio

The experiment of indirect holographic imaging is done with a high-dynamic-range vector network analyzer. In order to study the required system SNR in the interference pattern detection, a Monte Carlo –method is used. There, white Gaussian noise is added to the measured interference pattern data:

$$I_{\mathrm{N}}(\mathrm{SNR}) = I + A_{\mathrm{N}} \times 10^{-\frac{\mathrm{SNR}}{10}}, \tag{3.26}$$

where A_{N} is a Gaussian-distributed set of random numbers. The image is computed ten times with SNR ranging from −20 to +70 dB with 1-dB increments. The image signal-to-noise ratio ($\mathrm{SNR_{img}}$) and noise-equivalent reflectivity difference (NERD) is plotted in Figure 3-9. The image SNR starts to drop below the 40-dB system SNR, and it is about half of the maximum at the system SNR of 15 dB. The NERD starts to increase significantly when SNR is reduced to about 20 dB. As a consequent, the sufficient system SNR is estimated to be 10-20 dB [VI]. The contrast difference detected visually is 5 × NERD according to Rose's criterion [108].

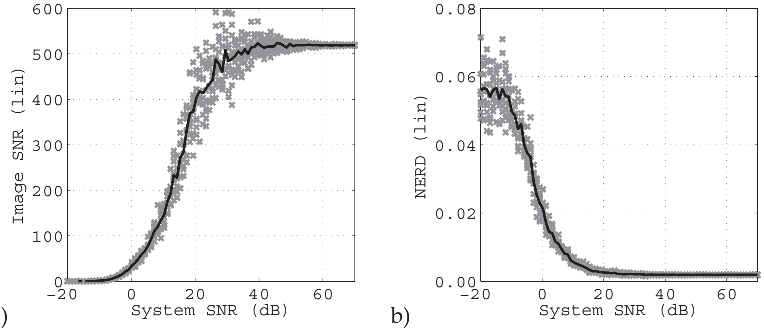

Figure 3-9. Image a) SNR and b) NERD as a function of the system SNR. A mean (black) of ten Monte-Carlo –runs (grey).

3. 3 Summary

The indirect holographic method is discussed in this chapter. Different methods used in the holographic imaging are discussed. The experimental work by the author is based on the Fourier- and spatial-domain techniques. The methods based on compressive sensing and coarse sampling are described in the literature [60], [61], [104]. The method based on a Fourier-domain technique is based on full sampling of the interference pattern, and the target wave is retrieved with numerical band-pass filtering of the target wave. The spatial-domain technique circumvents the requirement of Nyqvist sampling of the reference wave. However, it involves an additional measurement of the target wave amplitude – thus increasing the data-acquisition time. Both Fourier- and spatial-domain techniques are verified experimentally at 310 GHz. The Fourier-domain technique has some limitations to the reference wave direction and element spacing in the receiver array. The spatial-domain technique can be used without such limitations, but an additional measurement is required, leading to longer data acquisition time.

The method based on compressive sensing, [61], is based on a different approach than the Fourier-optics-based focusing. There the possible target geometry is correlated with the measured interference pattern. Since the target wave contributes to propagation from the target distance, the image can be focused to the wanted distance without distortions from elsewhere. This is not possible with the Fourier- or spatial-domain methods. However, algorithms related to compressive sensing are iterative and possibly computationally heavy. In coarse sampling, the aliasing of the reference wave is selected so that the aliased content does not overlap with the target wave. However, coarse sampling nevertheless involves restrictions on the reference wave.

Finally, the image quality is evaluated in the 310-GHz experiment. Quantitative metrics are measured by using the slanted-edge method. The image resolution with indirect holographic method is close to the theoretical diffraction limit. Also, the robustness of the indirect holographic method is assessed with SNR as a parameter in Monte Carlo –runs. With the experiment presented here, SNR can be as low as 10-20 dB for adequate image quality.

4 Millimeter-wave reflectarray

The concept of reflectarray was published by Berry et al. in 1963 [109]. There, the original theory of reflectarrays was derived and verified experimentally by using an array of rectangular waveguide sections. The phase shift of the reflected field was controlled by using shorting plugs at different depths in the waveguide sections. Also, the concept of active control of the reflectarray element was proposed. The waveguide array still had considerable depth and, as such, did not offer great improvement over the traditional reflector antenna. The idea of a planar reflectarray based on microstrip patch antennas was introduced separately by Malagisi [110] and Montgomery [111] in 1978.

In addition to the advantage of its planar form, microstrip reflectarrays are preferred due to their structural simplicity. Lithographic fabrication may be used in their fabrication, and as light-weight structures they are suitable for applications, where size and mass are critical parameters. In this chapter and in references [IV], [72], [73], [75], the reflectarray is considered as a front end of a millimeter-wave imaging radar. The reflectarrays discussed here are static, i.e., their phase shifting patterns are fixed. The reflectarrays are based on conductor-backed coplanar technology, and the final goal of the development is to couple the reflectarray elements with MEMS-based phase shifters controlled by a distributed CMOS-circuitry. The future reconfigurable reflectarrays will be combined with a millimeter-wave radar system for rapid imaging.

4. 1 Focusing of reflectarray

Figure 4-1 shows a scenario of an offset-fed reflectarray focused to a certain location $x_\mathrm{f}, y_\mathrm{f}, z_\mathrm{f}$. In the imaging application considered here, the reflectarray is focused to a near-field distance of few meters. The reflectarray phase pattern is optimized for each focusing distance separately in order to achieve optimal resolution and strongest reflection back from the target. The reflectarray is illuminated from an offset location, $x_\mathrm{s}, y_\mathrm{s}, z_\mathrm{s}$, with a spherical wave. The focusing in a reflectarray is introduced by suitable phase shift in the re-radiated wave from each element on the reflectarray at $x_\mathrm{e}, y_\mathrm{e}, z_\mathrm{e}$.

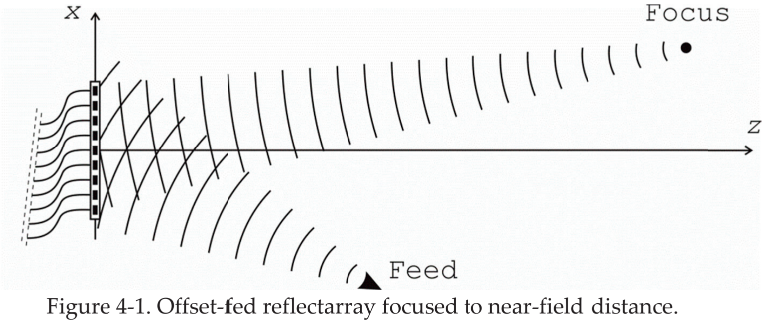

Figure 4-1. Offset-fed reflectarray focused to near-field distance.

Here, the electrical path length difference through reflectarray elements is compensated by a phase shift

$$\varphi(x_\mathrm{e}, y_\mathrm{e}) = \varphi_0 - k(|\mathbf{r}_\mathrm{e} - \mathbf{r}_\mathrm{s}| + |\mathbf{r}_\mathrm{f} - \mathbf{r}_\mathrm{e}|), \tag{4.1}$$

where the distance from the feed to an element on the reflectarray is

$$|\mathbf{r}_\mathrm{e} - \mathbf{r}_\mathrm{s}| = \sqrt{(x_\mathrm{e} - x_s)^2 + (y_\mathrm{e} - y_s)^2 + z_\mathrm{s}{}^2}, \tag{4.2}$$

and the distance from the element of the reflectarray to the focus is

$$|\mathbf{r}_\mathrm{f} - \mathbf{r}_\mathrm{e}| = \sqrt{(x_\mathrm{f} - x_\mathrm{e})^2 + (y_\mathrm{f} - y_\mathrm{e})^2 + z_\mathrm{f}{}^2}. \tag{4.3}$$

In [112] and in most of literature, the phase shift of the reflectarray element is written as

$$\varphi(x_\mathrm{e}, y_\mathrm{e}) = \varphi_0 - k(|\mathbf{r}_\mathrm{e} - \mathbf{r}_\mathrm{s}| + \mathbf{r}_\mathrm{e} \cdot \hat{\mathbf{r}}_\mathrm{f}), \tag{4.4}$$

or similarly, where $\mathbf{r}_\mathrm{e} = x_\mathrm{e}\mathbf{u}_\mathrm{x} + y_\mathrm{e}\mathbf{u}_\mathrm{y}$, $\hat{\mathbf{r}}_\mathrm{f} = \mathbf{r}_\mathrm{f}/|\mathbf{r}_\mathrm{f}|$, and

$$\mathbf{r}_\mathrm{f} = r(\sin\theta\cos\varphi\,\mathbf{u}_\mathrm{x} + \sin\theta\sin\varphi\,\mathbf{u}_\mathrm{y} + \cos\theta\,\mathbf{u}_\mathrm{z}). \tag{4.5}$$

The phase shift (4.4) only depends on the directional cosines of the focus. In this case, the reflectarray is focused to the far field. The reflectarray discussed in [IV] is designed for the center frequency of 120 GHz and it has a diameter of 138 mm. The far-field distance of the RA is about 15 meters. For imaging application, the future reconfigurable reflectarray will be focused to a near-field distance of few meters. The phase shift pattern of the RA is calculated from (4.1), which also takes into account the distance to the target.

4. 1. 1 Focusing gain

Focusing gain is used to describe the difference of the two phase shift schemes [75]. The focusing gain is defined as

$$G_\mathrm{f} = \frac{S_\mathrm{nf}}{S_\mathrm{ff}}, \tag{4.6}$$

where S_nf and S_ff are the electric field power densities when the phase shift is calculated from (4.1) and (4.4). Figure 4-2 shows the calculated focusing gain and beamwidth up to $z_\mathrm{f} = 7$ m, when $x_\mathrm{f} = 0$ and $y_\mathrm{f} = 0$, and the phase shift of the far-field focused reflectarray remains constant. Otherwise, the reflectarray is as described in [IV]. In this case, focusing gain is higher than 15 dB at a close distance to the reflectarray. The focusing gain falls of rapidly and it is 1 dB at 3.6 meters. At greater distance, the benefit of focusing becomes minimal.

For the near-field focused reflectarray, beamwidth is a linear function of distance, starting from about $\lambda/2$ near to the reflectarray. In the far-field focused case, the beamwidth changes rapidly in the near-field region and converges to the focused beam at greater distance. The rapid changes in the focusing gain and beamwidth can be described with the higher order modes of the Gaussian beam propagation [113]. The −3-dB beamwidth is in the both cases similar from approximately 1.6 meters on. Far-/near-field focusing of a reflectarray is discussed also in [71]. There, a reconfigurable 60-GHz reflectarray is focused to 1.5-5 m.

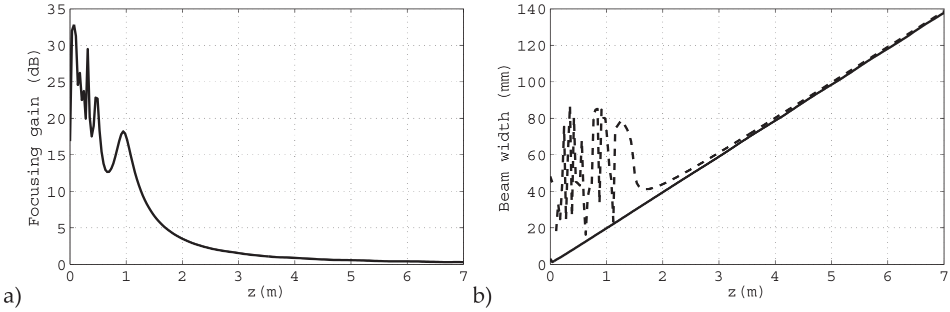

Figure 4-2. a) Focusing gain of RA focused to near field. b) The -3-dB beamwidth of focused (solid) and non-focused (dashed) RA. The focusing gain and beamwidth are considered for similar reflectarrays as described in [IV].

4. 2 Discretized reflectarray

The static reflectarrays presented in [IV] have discrete phase shifting. The discrete phase shift is chosen, since the final goal of the research is to couple the reflectarray elements with reconfigurable MEMS phase shifters [72], [74]. The static reflectarrays are fabricated for testing the radiation characteristics and advising the design of the final reconfigurable reflectarray, and therefore they have discrete phase shifts. The quantization step of the phase-shift is typically noted as:

$$q = \frac{360°}{2^b}, \tag{4.7}$$

where b is the number of bits used to control the phase shift. The phase quantization error due to discretization leads to gain reduction and increase in sidelobe level. The quantization error is bound to interval

$$-\frac{q}{2} \leq \psi \leq \frac{q}{2}. \tag{4.8}$$

4. 2. 1 Quantization efficiency

The gain reduction due to quantization error is described with the quantization efficiency

$$\eta_{\mathrm{q}} = \frac{G_{\mathrm{q}}}{G_0} = \left| \int_{-\frac{q}{2}}^{\frac{q}{2}} e^{j\psi} d\psi' \right|^2, \tag{4.9}$$

where ψ is the phase error due to quantization [114]. Figure 4-3 a) shows the quantization error in case of the 2-bit reflectarray presented in [IV]. The error results in a gain reduction of 0.9 dB. Typically, reconfigurable reflectarrays are designed for 1- or 2-bit phase shifters. Experiments with more phase states have been reported, such as that in [115], although the complexity of an increased number of digital signal lines may outweigh the slight increase in the reflectarray gain. Figure 4-3 b) shows the calculated quantization efficiency with the number of phase shift values from 2 to 9 and in case of the offset-fed geometry described in [IV]. The quantization efficiency is very close to that presented in [114], when a triangular phase quantization error is assumed. It is calculated for ideal phase shifters, when the beam is focused to boresight at 3-m distance. The efficiency depends also on the focusing scenario, and is typically lower when the steering angle is increased from boresight [116]. As the complexity of the phase shifter increases along the number of phase shift states, the loss increases also: resistive, dielectric, and radiation loss in the phase shifter may reduce the efficiency more than could be gained with increasing the bit count [117], [118].

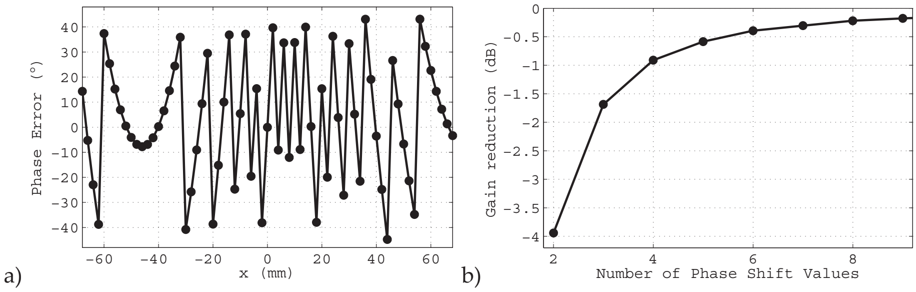

Figure 4-3. a) Phase quantization error in a 2-bit reflectarray. The maximum error is ±45°. b) Gain reduction due to quantized phase shifters for beam focused to boresight.

The gain reduction in the steered beam is due to the power being scattered to unwanted directions. Figure 4-4 shows beam patterns for an offset-fed reflectarray with continuous, 1-bit, and 2-bit phase shifting. The nature of the unwanted scattering depends on whether either or both the illuminating and re-radiated wave have a spherical wave front (Figure 4-4 a) or the reflectarray is used to divert a planar wave (Figure 4-4 b). Planar waves are involved, e.g., when RA is used as a subreflector in a beam-steering antenna system [119], [120]. In that case, the phase error is periodic, and grating-lobe-like erroneous beams emerge (Figure 4-4 a). The directions and amplitude of the erroneous beams depend on the number of phase states in the phase shifter [121]. In the case of most reflectarrays, the illuminating wave has spherical wave front, and the phase quantization error is aperiodic across the reflectarray. In this case, the quantization error results in rise of sidelobe level without high-directivity quantization lobes (Figure 4-4 b). As the phase error is not periodic, the radiation into sidelobes is spread into a large area and the sidelobe level is rather modest compared to that of reflectarrays dealing with planar wave fronts and directive quantization error lobes.

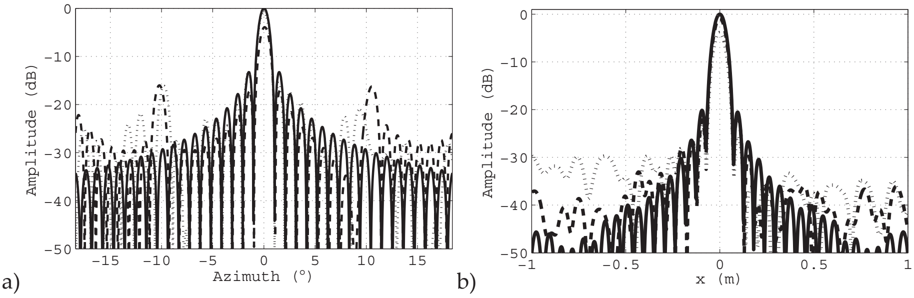

Figure 4-4. Calculated beam patterns for a) far-field- and b) near-field-focused reflectarray. The azimuth range in b) corresponds to the same field of view as in a). Continuous (solid), 2-bit (dashed), and 1-bit (dotted) phase shifting are used in the calculations.

4. 2. 2 *Element spacing and specular reflection*

The more phase states there are in the phase shifters, the larger area must be allocated both for the phase shifter and the signal lines controlling them in a reconfigurable RA. As the center-to-center spacing of the elements is increased from half a wavelength, the grating lobes enter the visible region and a smaller part of the illuminating wave is re-radiated by the elements. The reflectarray elements in this work have spacing of 0.8 λ, as space is allocated for the future MEMS-based phase shifter and its bias lines. In this case, the number of the elements is also specified by the parallel work on the high-voltage CMOS circuit controlling the individual elements. The 138-mm reflectarray has approximately 3700 elements on it. The grating lobes are avoided by limiting the scanning area as a part of standard design process. The part the illuminating field, which is not re-radiated from the element phase shifter, is reflected from the structures between the elements, typically from substrate or metallization [112]. Also, if the impedance matching between the antenna and phase shifter is poor, part of the illuminating power is reflected from the antenna without being phase shifted [122]. Both of these components contribute to the specular reflection from the reflectarray [74], [123], [124], [125].

In [126], it was concluded that the specular reflection is small by selecting the element spacing so that the area occupied by the element is smaller or equals the effective area of the element antenna. In the work presented in [IV], the element spacing is 2 mm and the antenna gain is $G \approx 3$, resulting in an effective area of $A_\mathrm{e} \approx 1.5\,\mathrm{mm}^2$ at 120 GHz. The effective area is 38 % of the area occupied by the element, and the specular reflection occurs. Figure 4-5 shows the calculated beam pattern at 3 m for the reflectarray. The level of the specular reflection is 25 dB below the main beam, at similar level than reported in [126].

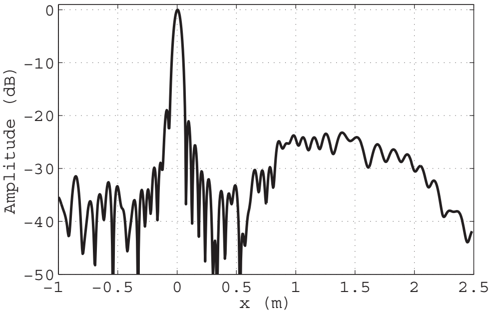

Figure 4-5. Calculated beam pattern for offset-fed reflectarray with element spacing of 2 mm and element antenna effective area of $A \approx 1.5\ \mathrm{mm}^2$. Distance to the RA is 3 m.

4. 2. 3 *Reflectarray efficiency*

Similarly to the conventional reflector antenna, the reflectarray antenna efficiency is defined by aperture illumination efficiency or taper efficiency η_t and spill-over efficiency η_s [112]. In addition to the quantization efficiency, η_q, the specular reflection in the reflectarray reduces the antenna efficiency. The reflectarray element efficiency is defined as

$$\eta_\mathrm{e} = \frac{|\Gamma_\mathrm{m}|^2}{|\Gamma_\mathrm{m}|^2 + |\Gamma_\mathrm{s}|^2}, \tag{4.10}$$

where Γ_m and Γ_s are the re-radiated and specular components of the reflection coefficient of the reflectarray element [IV]. The efficiency describes how much of the power reflected from the reflectarray is re-radiated from the phase shifter compared to the total power reflected from the reflectarray. The reflectarray maximum gain can be estimated as

$$G_\mathrm{RA} = \eta_\mathrm{q}\eta_\mathrm{t}\eta_\mathrm{s}\eta_\mathrm{e}\eta_\mathrm{l}\frac{4\pi A_\mathrm{e}}{\lambda^2}, \tag{4.11}$$

where η_l accounts for the dielectric and resistive loss in the reflectarray. Note that the reflectarray gain is defined only in the case of far-field focusing. In the case of near-field focusing, the far-field quantity (4.11) is not well defined and additional contribution from focusing gain must be taken into account. The reflectarray element efficiency can be determined from radiation patterns by comparing the levels of the steered beam and the specular reflection. The theoretical element efficiency is determined with a parametric simulation in [IV]. There, the reflectarray element is based on a conductor-backed coplanar antenna coupled with an open-ended or short-circuited stub. As the length of the stub is increased, the phase of the re-radiated wave is decreased according the phase curve in Figure 4-6 a).

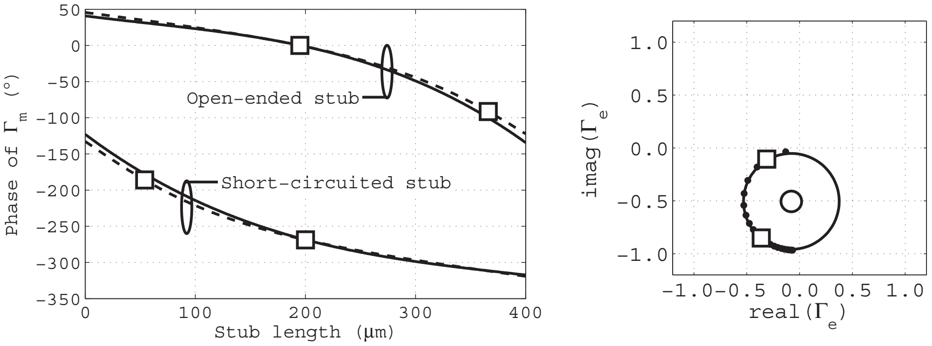

a)

b)

Figure 4-6. a) Simulated phase curve of reflectarray elements. Analytical model (solid) based on simulation and full-wave simulation (dashed). b) Simulated reflection coefficient (dots) of the reflectarray element in the complex plane. Squares show the stub lengths used in the fabricated reflectarrays [IV]. The locus of reflection coefficient is a circle, when the stub length is varied.

In [IV] the efficiency (4.10) is determined from simulation with the software Ansoft HFSS. There, the reflectarray is idealized as an infinite array of identical elements. The incident wave used in the simulation is the Floquet mode representing normally incident plane wave. The generalized scattering matrix of the Floquet-port modes is then used to extract the reflection from the element:

$$\mathit{\Gamma}_{\mathrm{e}} = \mathit{\Gamma}_{\mathrm{m}} + \mathit{\Gamma}_{\mathrm{s}}. \tag{4.12}$$

Figure 4-6 b) shows the reflection coefficient in complex plane as the stub length is varied. The locus of the reflection coefficient is a circle. Its radius equals to $|\mathit{\Gamma}_{\mathrm{m}}|$ and its center is at distance of $|\mathit{\Gamma}_{\mathrm{s}}|$ from the origin. The re-radiated and specular components of (4.10) are found by least squares fit of a circle to the simulated data. From simulations, it is found that the efficiency of reflectarrays element varies from 0.22 to 0.68 when the size of the element is varied [74]. Note that the method to find the efficiency in [IV] applies in cases, where the specular reflection is nearly constant and only the phase-shifted component is changing. This is not the case with, e.g., reflectarrays with varying sized patch antennas. In our case, the change in the phase shifter length does not change the specular reflection significantly. It is expected, that the specular reflection with the reconfigurable RA elements remains nearly constant as well, since the phase shifter structure is designed not to radiate.

4. 2. 4 Phase-shift assignment

In [IV], the different stub configurations are selected so that the desired relative phase difference occurs in $\mathit{\Gamma}_{\mathrm{m}}$ (Case A). In most published works on reflectarrays, such as in [112], the phase difference is optimized for $\mathit{\Gamma}_{\mathrm{e}}$ (Case B). In those works the re-radiated and phase-shifted component includes the specular reflection. The different kinds of phase shifting are illustrated in Figure 4-7. When efficiency is high, the phase shifts can be found correctly in both ways.

If the efficiency is small, after a certain limit, the phase shift cannot cover the desired range in Γ_{e}, and a suitable phase shift is no longer available. However, the correct phase shift is always found for Γ_{m}. Figure 4-8 shows the available phase shift in Γ_{e} as a function of the efficiency. Naturally, at higher efficiency than $\eta_{\mathrm{e}} = 0.5$ the phase range abruptly goes to 360°.

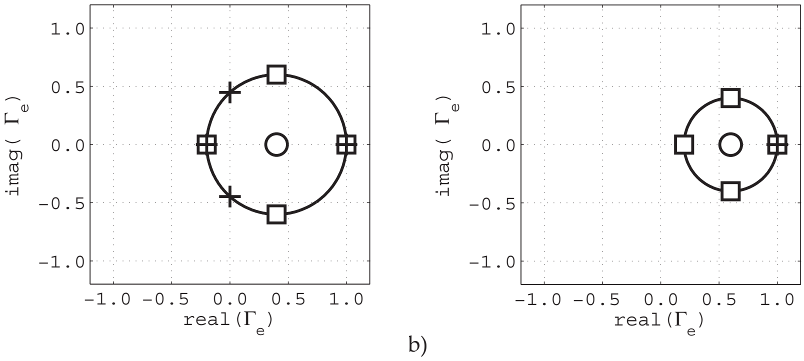

a) b)

Figure 4-7. Sketch of reflectarray element phase shift when a) $\eta_{\mathrm{e}} = 0.6$ and b) $\eta_{\mathrm{e}} = 0.4$. Squares show the phase shift assignment scheme used in [IV] (Case A) and crosses show the phase shifts used, e.g., in [112] (Case B). Only one correct phase shift can be found in the latter case when $\eta_{\mathrm{e}} = 0.4$.

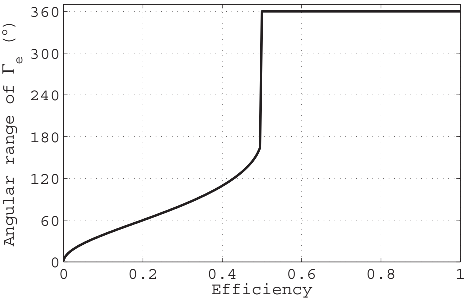

Figure 4-8. The phase range of Γ_{e}.

Figure 4-9 a) shows the mean level of the specular reflection compared to the level of the steered beam for Case A and B. The mean ranges from $x = 1$ to 2 m (see Figure 4-5). At efficiency of $\eta_{\mathrm{e}} = 0.5$, the specular reflection level is the same in both of the phase optimizations scenarios. At higher efficiency, Case B overcomes Case A by 3.6 dB at maximum. The specular-reflection level becomes the same again at efficiency of $\eta_{\mathrm{e}} = 1.0$. For $\eta_{\mathrm{e}} < 0.5$, Case B is no longer correct, and the mean level of the specular reflection becomes higher than that for Case A. The maximum difference is about 3.6 dB. Figure 4-9 b) shows the normalized gain in both cases. The gain for Case A is always higher than that for Case B. At $\eta_{\mathrm{e}} = 0.5$, the gain for Case B is 4 dB lower than for Case A. The gain decrease for Case B results from the unintended amplitude modulation at lower than unity efficiency. At $\eta_{\mathrm{e}} = 0.5$, the reflection coefficient varies between $|\Gamma_{\mathrm{e}}| = 0$ and 1. Note that the specular reflection is assumed to have zero imaginary part, and two of the desired phase states lie on the *x*-axis. In a general case the reflectarray element is designed for any equi-spaced configuration of the phase shifts, and not necessarily 0°, 90°, 180°, and 270°. This gives a slightly different result from those presented in Figure 4-9 for Case B, but the trend is similar.

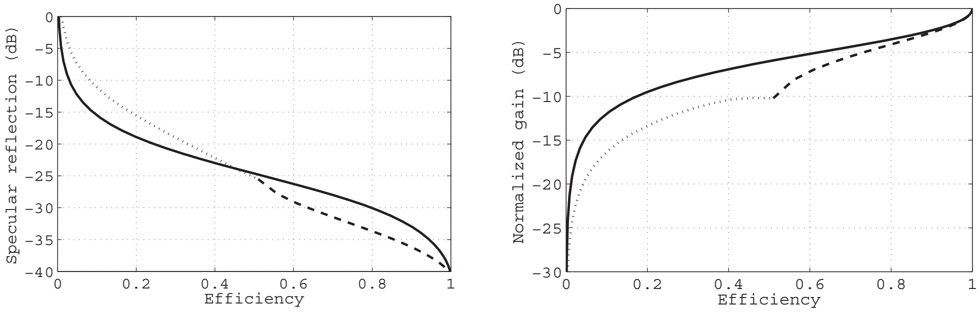

a) b)

Figure 4-9. a) Level of the specular reflection normalized to the steered beam. b) Normalized gain as a function of the efficiency. Phase optimization on Γ_m (solid, Case A) and Γ_e (dashed, Case B). Dotted line is for the case when the phase range is less than 360°, and thus correct phase assignment fails.

4. 3 Fabricated reflectarrays

The reflectarrays in [IV] are realized based on Case A –phase shifting. Three differently focused prototypes are fabricated. The reflectarray elements are based on a conductor-backed coplanar patch antenna, which was patented by Greiser in 1976 [127]. The properties of the antenna are similar to a microstrip patch antenna [128]. Figure 4-10 shows the simulation model of the antenna. The patch size is 1.23 mm by 0.60 mm, and it is fed with a CPW line at its edge. Aperture-coupled coplanar patch antennas are suggested to be used due to their easy matching and possibility to design the radiating and feeding structure separately [129], [130]. However, in the case presented here, the reflectarray will be fabricated on a silicon wafer with distributed high-voltage CMOS electronics on the other side, leaving only one surface for the millimeter-wave components. The optimal aperture-coupled design cannot be used, and both the antenna and the phase shifter are located on the top metallization of the coplanar structure.

4. 3. 1 Reflectarray element design

The patch is surrounded by the upper conductor, which is connected to the ground plane with vias. The substrate between the conductor planes is a 50-µm thick layer of polyimide. Polyimide is chosen, since it allows for deposition of uniform substrate layers with spin coating [131]. Also, polyimide is suitable for trough-substrate vias, since it can easily be etched [132]. Coplanar waveguides with loss of the order of 0.5 dB/mm at 60 GHz have been fabricated in [133] and [134]. In simulations with the reflectarray element, loss tangent of the substrate is assumed to be $\tan\delta = 0.008$. This results in 0.24-dB of dielectric loss, when the reflectarray is simulated for normal-incidence reflection.

Figure 4-10 a) shows the simulation model of the reflectarray element antenna. The antenna dimensions are optimized for 120 GHz. Also, the arrangement of the vias surrounding the antenna patch is a critical design parameter [135]. The vias appear as a short circuit to the parallel-plate mode in the substrate, and they form a resonant cavity. The cavity is strongly coupled to the antenna, and position and spacing of the vias must be optimized together with the antenna. Figure 4-10 b) shows the reflectarray element with the open-ended stub as a phase shifter. The simulation result presented in Figure 4-6 b) is in the case, when the stub length is varied from 0 µm to 400 µm. The reflectarray element has a simulated efficiency of $\eta_\mathrm{e} = 0.45$ or 0.62, depending whether an open-ended or short-circuited stub is used. The simulated antenna bandwidth is about 5 GHz, which can be considered also as the overall bandwidth of the reflectarray [136]. The −3-dB beamwidth of the antenna is 78° and 80° for the E- and H-plane, which allows for scanning the whole grating-lobe-free range (Figure 4-11).

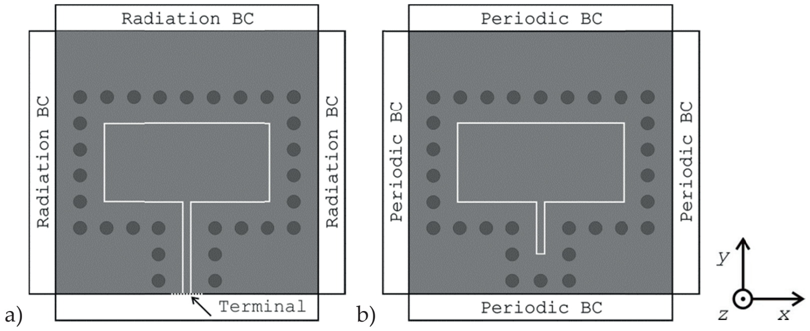

Figure 4-10. Simulation models of a) conductor-backed coplanar patch antenna with radiation boundary conditions, and b) RA element Floquet-port excitation with y-polarization. Periodic boundary conditions "Master-Slave" are used in HFSS, i.e., an infinite array of identical elements is assumed.

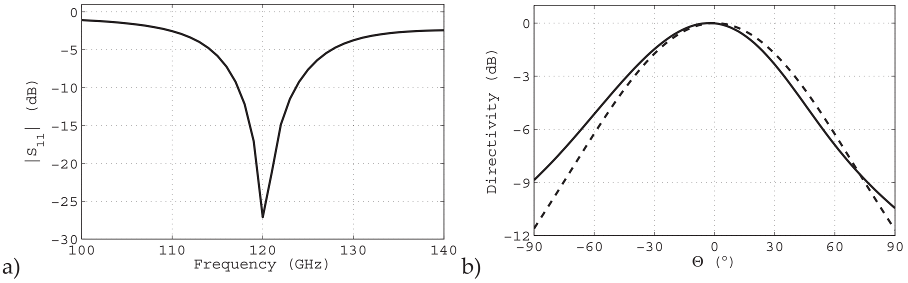

Figure 4-11. a) Simulated amplitude of the S_{11}-parameter of the antenna. b) The normalized directivity of the antenna in E- (solid) and H-plane (dashed).

4. 3. 2 Near-field measurements of reflectarrays

Three different variations of the reflectarray are characterized in the near-field measurement range. The fabricated reflectarrays are focused to boresight and offset direction at near-field distance (RA#1 and RA#2) as well as to boresight at far-field distance (RA#3).

4. 3. 3 Beam patterns

The key figures of the measured beam patterns are listed in Table 4-1. The reflectarrays are found to steer the beams closely as planned and the beamwidth is within 10 % of the theoretical. The results are the first near-field beam pattern measurements at this high frequency for reflectarrays, and demonstrate the feasibility of the polyimide-based coplanar structure for use with the future reconfigurable design.

Table 4-1. Key figures of reflectarray beam patterns. The beam patterns are evaluated both in x- and y-directions, separated by "/" [IV].

		Simulated, ideal	**Simulated, curved**	**Measured**
RA#1	3-dB BW (mm)	58 / 64	58 / 64	58 / 67
	Level of the 1st sidelobes (dB)	–21 / –23	–19 / –18	–15 / –25
	Main beam deviation (mm)	-	-	–2 / 17
RA#2	3-dB BW (mm)	62 / 62	62 / 64	61 / 66
	Level of the 1st sidelobes (dB)	–19 / –18	–18 / –15	–16 / –18
	Main beam deviation (mm)	-	-	14 / –19
RA#3	3-dB BW (mm)	60 / 64	60 / 62	62 / 70
	Level of the 1st sidelobes (dB)	–13 / –16	–16 / –20	–12 / –13
	Main beam deviation (mm)	-	-	–2 / –13

After fabrication, it was found out that the reflectarrays were curved due to internal contraction. The reflectarray goes through five coating-curing periods before the substrate is of the desired thickness. As the fabrication proceeds, the contraction increases in the substrate layer by layer. The reflectarrays are concave, and their deviation from planar is up to 320 μm, or 89° in the aperture phase. Figure 4-12 shows the measured reflectarray profile and the resulting phase error across the reflectarray aperture. The phase error is a least squares fit of a fourth-order polynomial surface to the measured profile, and it is used in calculating the beam patterns. The shape of the reflectarray partly explains the observed level of the first sidelobes. In case of the reflectarray focused to far field, the calculated sidelobe level is decreased, since the concave shape introduces unintended focusing. However, in this case, the measured sidelobe level is not reduced.

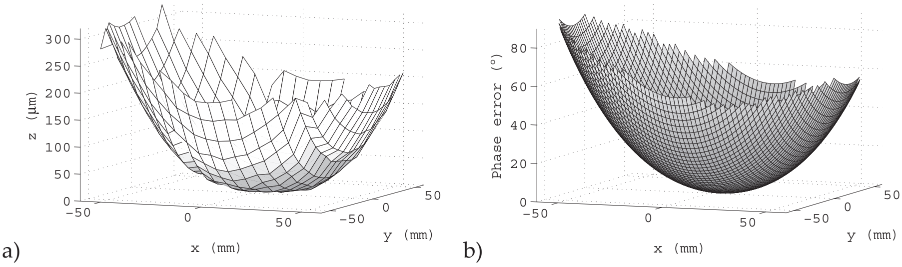

Figure 4-12. a) Measured reflectarray shape as depth from the RA aperture. Note the different scale in the *z*-axis. b) Phase error due to reflectarray curvature. The phase error is calculated at the reference plane, where the planar reflectarray would be.

4. 3. 4 Aperture field imaging

In addition to beam pattern measurements, the efficiency of the reflectarrays is experimentally determined in [IV]. As the phase shifters in the reflectarrays are fixed, the specular, Γ_s, and re-radiated, Γ_m, reflection components cannot be found directly. The reflectarrays are focused to few meters at least, and the specular reflection diverges to offset direction from the reflectarray. In order to measure both the specular reflection and the main beam, the measurement area would be several meters in the offset direction (Figure 4-5). Instead, the efficiency is determined from near-field measurement of the reflectarray. In a typical near-field measurement range, the radiating near-field is measured in a plane parallel to the aperture of the antenna [82], [84]. In most cases the field is measured in a rectangular raster scan over the area, where the radiating field is at significant level. The specular reflection from the reflectarray in [IV] propagates to an offset direction at a maximum angle θ_max as is shown in Figure 4-13. The scanning area is located so that both the steered beam to boresight direction and the specular reflection are covered. The feeding structure allows for measurement distance of 0.6 m, which results in scanning area of 0.7 m × 0.4 m in [IV].

The tangential component of the measured near-field is transformed to the aperture of the reflectarray with the Fourier-transform pair (2.32) and (2.33). This kind of plane-to-plane transform has been widely used in diagnostics of large reflector antennas [137], [138]. For a fair comparison, the near field of the RA is simulated at the same scanning area as the measurement is done, and the same transform is used to model the aperture field at the RA surface. As a result, the theoretical and measured aperture fields can be compared so that unidealities due to spacing and limited scanning area are taken into account.

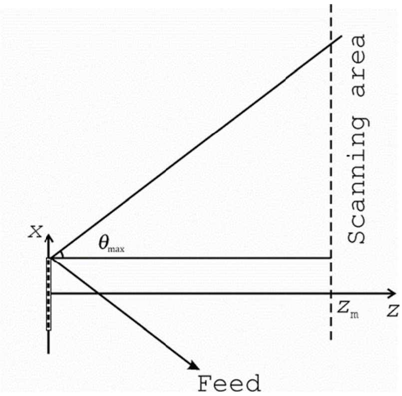

Figure 4-13. Near-field measurement arrangement.

The measured amplitude of the reflectarray aperture field is shown in Figure 4-14. The periodic amplitude of Γ_e is seen as a ripple in the RA aperture field. Cuts of both the measured and theoretical aperture field are shown in Figure 4-15. The measured and theoretical results are a close match at efficiency of 0.06-0.11. This is lower than the expected average efficiency. However, the excellent match in the RA aperture field amplitude and phase suggests that the method is very useful for evaluating the RA efficiency. Compared to beam pattern measurements, the method allows for local characterization of the RA elements. This could be very useful with reconfigurable RAs with MEMS, where it is difficult to verify the operation of the active elements otherwise. The lower than expected efficiency is most probably due to over-etching of the coplanar structures in the reflectarray element, as microscopic inspection reveals almost twice as wide coplanar waveguide gap of 14 μm compared to the design value of 8 μm. Over-etching reduces the dimensions of the element antenna by similar amount and increases the resonant frequency.

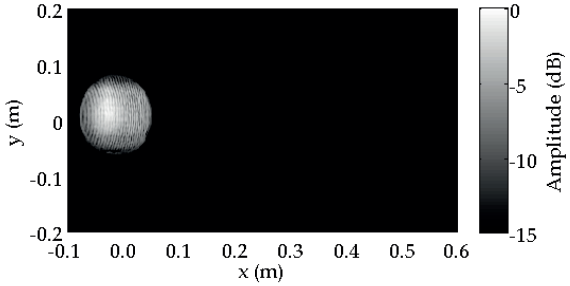

Figure 4-14. The amplitude of the reflectarray aperture field. The amplitude is transformed to the surface of the RA from near-field measurement at 0.6 m. The scanning area is mostly to the direction of the positive *x*-axis in order to measure the specular reflection. The re-radiated and specular parts introduce an interference pattern of the RA.

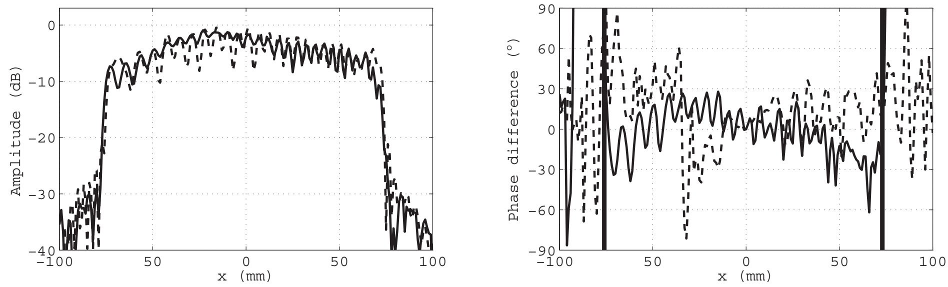

a) b)

Figure 4-15. a) The measured (solid) and simulated (dashed) aperture field amplitude of the RA. b) The difference of the measured and simulated aperture field phase in *x*-(solid) and *y*-directions (dashed). The vertical lines show the −20-dB amplitude of the aperture field. Efficiency of 0.11 is assumed in the simulation.

Similar effort to characterize the reflection at the surface of a RA is described in [139], [140], [141], and [142]. There, a high-resolution probe is used to measure the reflection phase across the reflectarray. The method allows characterizing the reflectarray element by element. The disadvantages of the method are possible element-probe interaction and shadowing of the spatially fed reflectarray. The challenges related to the close proximity of the probe and the elements are avoided in the near-field method in this work.

4. 4 Reconfigurable reflectarray

The open-ended and short-circuited stubs will be replaced with MEMS-based phase shifters in the reconfigurable reflectarray [72]. The phase shifters are closely related to the distributed transmission line phase shifter. There, a coplanar line is capacitively loaded with, e.g., varactor diodes [143] or with MEMS capacitive switches [144], [145]. The loading slightly changes the propagation constant of the line and introduces the phase shift. The digital phase shifter at microwave frequency was introduced in [146], where capacitive MEMS bridges have two distinct states, at the upmost position or against a thin layer of dielectric on the center line. Compared to the analog designs, advantage of the digital phase shifter is its stability against noise in the bias line. The MEMS switches in the reflectarray element have stronger capacitive loading than in the distributed transmission line. There, the loading impedance of the MEMS switch is tuned so that the transmission line is shorted in the down-state, whereas the line is not disturbed at the upmost position [147], [148]. The simulated phase shift is shown in Figure 4-16.

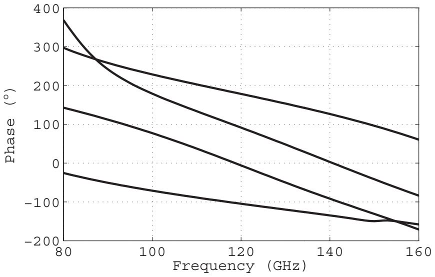

Figure 4-16. Simulated phase shift of the 2-bit MEMS phase shifter [72].

Figure 4-17 shows a fabrication sample of the top metallization of the reflectarray and the MEMS phase shifter. The sample has the antenna etched on the metallization and the bias-line paths for the MEMS are running between the elements. The sample is not functioning device, rather it is a fabrication trial. The MEMS phase shifter is fabricated separately. Instead of using the polyimide substrate, this test piece of the phase shifter is fabricated on a standard silicon wafer without the backing ground. The coplanar structure is isolated from the MEMS capacitors by a 200-nm thick layer of silicon dioxide. When in its upper position, there is a 1.2-μm air gap between the MEMS capacitor plate and the DC-grounded coplanar line. The gap of the transmission line is almost ten times wider under the MEMS structure than elsewhere. The wider gap compensates for the capacitive load due to the MEMS structure so that the characteristic impedance of the ensemble is 50 ohms. The phase shifters have been successfully tested at 75-110 GHz [74].

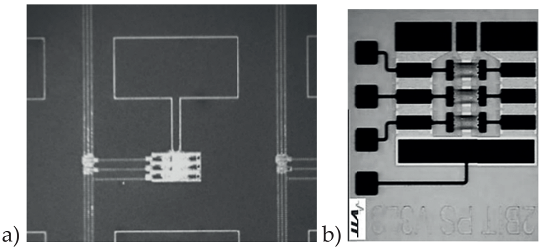

Figure 4-17. a) Fabricated sample of top ground of a reconfigurable reflectarray. The sample is an early trial of fabrication and it is not structurally intact. b) Functioning sample of the MEMS phase shifter. The three MEMS switches are biased through contact pads on the left and the coplanar port is atop. The RA structures are fabricated at the Technical Research Centre of Finland (VTT).

4. 5 Summary

In this chapter, the design considerations of a millimeter-wave reflectarray are presented. The near-field focusing of reflectarray can result in gain in link budget at close distance to the reflectarray. However, in the case presented here, at a distance of only ca. 20 % of the far-field condition, focusing to the near field does not improve the link budget compared to the case when the RA is focused to the far field. Different quantization scenarios affect the achievable gain and the level of the specular reflection from the RA. In case of the compromised condition with the RA element spacing greater than half a wavelength, the specular reflection is always present, and preferable quantization scenario must be chosen according to the re-radiated reflection from the RA elements (Case A in Section 4. 2. 4). The specular reflection from the reflectarray decreases its radiation efficiency since part of the transmitter power is lost. The loss can be taken into account in the efficiency of the reflectarray, which describes the ratio of the power in the steered beam and the total power reflected from the RA.

Differently focusing reflectarrays have been fabricated, and they have been characterized in a near-field measurement range. The reflectarrays have been fabricated based on the conductor-backed coplanar technology, which is compatible with microfabrication technology. When the found unidealities, substrate contraction and over-etching, are taken into account, the performance of the fabricated static RAs is found to be close to theoretical. The efficiency of the RAs is studied with a method based on aperture field imaging. By comparing the theoretical model to measured aperture field, it is possible to estimate the RA efficiency locally on the aperture surface.

5 Submillimeter-wave holograms

In compact antenna test ranges and radar-cross-section ranges, a planar wave front is needed in order to measure the directivity, gain, or RCS of the device under test (DUT). RCS measurements have been done in a compact range at millimeter- and submillimeter wavelengths in [149], [150]. Instead of carrying out the measurement at the far-field distance (2.1) from the feeding antenna, DUT is measured at much closer distance by artificially collimating the wave front.

The dimensions and quality requirements of the quiet zone vary depending on the application. A hologram-based CATR for high-gain reflector antennas may require QZ of several meters in diameter. For accurate antenna measurements, the QZ amplitude and phase ripple is generally required to be less than 1 dB and 10°, peak-to-peak [14]. The holograms considered in the following are suitable for reflectivity measurements of the order of 100-mm diameter samples. In this work, submillimeter-wave holograms are characterized and used in RCS ranges for radar absorbing material measurements.

In active imaging, the contrast between different materials is due to the differences in reflectivity. The reflectivity of homogeneous material samples is well known based on their dielectric properties [52]. However, at submillimeter wavelengths, the surface roughness and non-uniform material properties of every-day targets can have significant effect and their reflectivity must be determined case by case [28]. The hologram-based RCS range is well suited for measuring the reflectivity of general materials, such as clothing, and it could therefore be used as a tool for studying imaging phenomenology.

5. 1 Design aspects of holograms

The holograms modulate the amplitude and phase of the incident field $\mathbf{E}_\mathrm{i}$ in such a way that the desired wave front $\mathbf{E}_\mathrm{o}$ emerges. The modulation of the incident field can take place in transmission through the hologram or in reflection from it. The control of both the amplitude and phase of $\mathbf{E}_\mathrm{i}$ is difficult, and the holograms are realized either with amplitude- or phase-modulating structures. Amplitude holograms are fabricated by wet etching on metallized Mylar films, and in practice they can be considered as 2-dimensional structures. Compared to amplitude holograms, optimization and fabrication of phase holograms is more challenging as they are fabricated as 3-dimensional structures. In addition to the desired modulation, parasitic amplitude and phase distortions occur, and their minimization poses an optimization problem [151]. The advantage of the phase holograms in RCS ranges is their higher efficiency compared to the amplitude hologram [23].

5. 1. 1 *Phase holograms*

Figure 5-1 shows the hologram setups for both transmission- and reflection-type phase holograms. The feed is positioned on the hologram axis at distance of the hologram focal length and the planar wave front propagates in 33° angle relative to the normal of the hologram. The directly transmitted or reflected field can be significant into normal direction from the hologram. The angular separation is selected to avoid the overlap of the undesired wave front and the QZ. Due to projection of the hologram diameter, the greater the angle the larger hologram is needed. Also, the details on the hologram become smaller with a greater separation angle.

The phase holograms are fabricated by milling grooves on bulk material. In transmission- or reflection-type holograms the material is polytetrafluoroethylene (PTFE, Teflon, $\varepsilon_{\mathrm{r}} \approx 2.1$) or aluminum, respectively. The phase modulation is optimized by varying depth, width, and period of the groove pattern. With the configuration as shown in Figure 5-1, the period of the grooves in the holograms is about $\lambda - 3\lambda$ across the cut in the *x*-*z*-plane. The diameter of the holograms in this case is 24-26 cm and the feed is at 1-m distance from it, resulting in a focal ratio from 3.8 to 4.2. The maximum depth and width of the grooves are of the order of a wavelength. The fabrication tolerance for the phase holograms is of the order of $\lambda/20$, which allows for using cost-effective techniques, such as CNC milling, in hologram fabrication up to several hundreds of gigahertz [151]. A schematic view of the hologram and photograph of the fabricated 310-GHz hologram are shown in Figure 5-2.

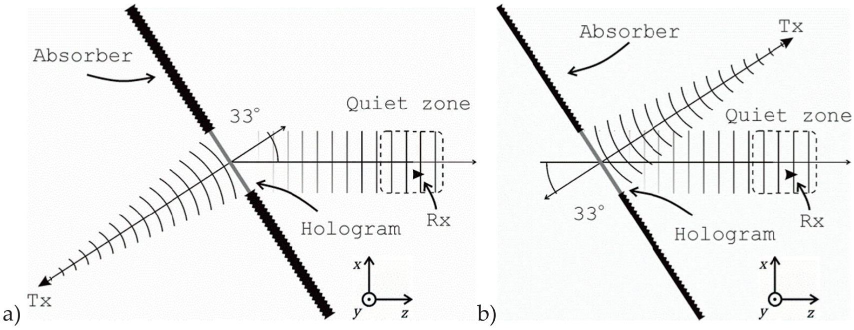

Figure 5-1. a) Transmission- and b) reflection-type holograms. The axis of the planar wave is in 33° angle to the normal of the hologram.

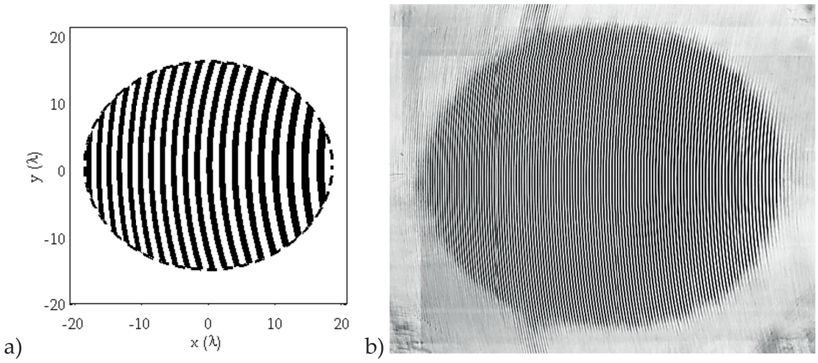

Figure 5-2. a) Schematic illustration of the hologram groove pattern. For the sake of clarity, the hologram dimensions are one tenth of the fabricated one. b) Photograph of the fabricated reflection-type phase hologram. The groove pattern is milled on a 20-mm thick aluminum plate.

5. 2 Measurement results

The standardized metrics for evaluating the hologram performance are the amplitude and phase ripple in the designed area of the quiet zone. The quiet-zone quality is measured for the transmission-type phase hologram at 650 GHz and reflection-type phase hologram at 310 GHz in the near-field range described in Section 2. 5. 1. Also, hologram diffraction efficiency and cross-polarization level are evaluated for the reflection-type phase hologram at 310 GHz.

5. 2. 1 Diffraction efficiency

The diffraction efficiency of a hologram is defined as

$$\eta_{\text{diff}} = \frac{\int_{\text{QZ}} S dA}{\int_{\text{HA}} S dA}, \tag{5.1}$$

where S is the electric field power density and the integrals are over the areas of the QZ and feed illumination at the location of hologram aperture (HA). The cross-polarization level is defined as ratio of electric field amplitudes in horizontal and vertical polarization. The polarization is defined according to Ludwig's first definition [152], since the propagation in the quiet zone is strictly confined in the direction of normal to the measurement plane.

Holograms introduce cross polarization due to the curved structure of the grooves. Cross-polarization level of an antenna is an important metrics, when the different polarizations are used as separate transmission channels or when polarization effects are studied in RCS or material reflectivity measurements. Compared to antenna and RCS ranges of other types, cross-polarization level with holograms can be higher. Polarizing grids have been suggested to reduce the cross-polarized level [14].

5. 2. 2 Quiet-zone quality

The measurement arrangement is as shown in Figure 5-1. A corrugated horn antenna is used as the feed and the receiver with an open-ended waveguide probe is positioned in the quiet zone at a distance of 1 meter from the hologram surface. The key results from [V], [151], [153], and [154] are listed in Table 5-1. With both the transmission- and reflection-type holograms, the amplitude ripple is close to the expected value. However, the phase distortions are up to three times larger than expected. The higher phase ripple is assumed to be due to fabrication errors and the relatively large uncertainty in the phase measurement in the near-field range.

Table 5-1. Key results of simulations and measurements of the phase holograms.

QZ quantity	**Transmission type**			**Reflection type**	
	Simulation	Measurement	Measurement	Simulation	Measurement
Frequency (GHz)	650		310	310	
1-dB width (mm)	100	100-120	100-120	100	120
Amplitude ripple (dB)	2	2 (6)	2	0.5	0.5
Phase ripple (°)	13	29 (50)	10	3	10
X-pol level (dB)	-	-	−28	-	< −21
Diffraction efficiency (dB)	−3.5	-	−4	−3	−3.6

In amplitude holograms, the modulation of the input wave is always relatively inefficient, since part of the energy is blocked with the metallized pattern. In phase holograms, most of the input wave is transmitted and modulated. Transmission-type phase holograms have losses related to the dielectric loss tangent and the mismatch at the free-space/dielectric boundaries. Also, as the transmission-type phase hologram is fabricated on a relatively thick plate of dielectric material, there may be resonant effects within the material, as well. The reflection-type phase hologram is free of the dielectric loss and resonant effects, and it has highest efficiency reported for beam-shaping holograms. Also, reflection-type hologram is convenient for its geometry: both the feed and the quiet zone are on the same side of the hologram, and the compact range can be constructed in a small space. With reflection-type holograms, the feed can radiate into the quiet zone either directly or by scattering from the supporting structure of the hologram, resulting in degraded quiet-zone quality. Careful elimination of unwanted scattering is therefore needed.

5. 3 Reflectivity of radar absorbing materials

A transmission-type phase hologram is used to construct a monostatic RCS range at 310 GHz [153]. There, calibrated RCS or relative reflectivity level of a target is measured. The reflectivity of different radar-absorbing materials is measured in [VI] at 310 GHz and at 650 GHz [VII], [27]. The work is motivated by need to find a cost-effective RAM for a hologram-based CATR. In addition to commercially available RAM, sheets of different low-cost carpet are measured. In the 310-GHz measurement, the reflectivity is measured at different polarizations as well.

5. 3. 1 Radar-cross-section measurement range

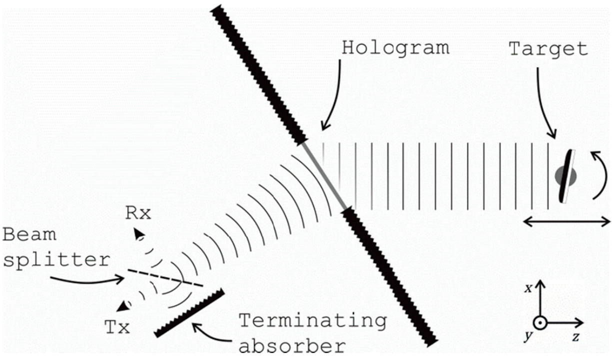

Figure 5-3. RCS setup for reflectivity measurements.

The RCS setup is shown in Figure 5-3. The target is placed in the quiet zone on a translational/rotational stage. The target consists of an aluminum plate with the absorber attached on one side of it. The target is placed on a pylon made of extruded polystyrene foam, which has low reflectivity at submillimeter waves. The monostatic configuration is achieved with a quasioptical beam splitter, which couples the transmitter and receiver to the hologram input wave. At the receiver, the total field $\mathbf{E}(z)$ is a sum of the two components with additional phase shift, due to the two-way propagation from the hologram to the target:

$$\mathbf{E}(z,\theta) = \mathbf{E}_0 + \mathbf{E}_\mathrm{T}(\theta)e^{-j(2kz+\varphi_0)}, \tag{5.2}$$

where θ is the rotation angle of the target and $\mathbf{E}_0$ is the background reflection including the directly coupled component, back-scattering from the hologram, and reflection from the surroundings of the setup. The direct coupling is possible through scattering from the quasioptical beam splitter. $\mathbf{E}_0$ is assumed to be constant during the measurement. $\mathbf{E}_\mathrm{T}(\theta)$ is the reflected component from the target and $2kz + \varphi_0$ is phase shift due to two-way propagation from the Rx/Tx to the target. For each rotation angle, the target is moved 3 λ in the z-direction. In Fourier domain, the reflection from the target appears at spatial frequency of $2k$ whereas the background reflection is at zero spatial frequency. The reflectivity is given as

$$|\Gamma(2k,\theta)| = \left|\frac{\mathcal{F}\{\mathbf{E}_{\mathrm{T}}(\theta)\}}{\mathcal{F}\{\mathbf{E}_{\mathrm{T}}(0^\circ)\}}\right|, \tag{5.3}$$

where $\mathcal{F}$ denotes the Fourier transform and $\mathbf{E}_{\mathrm{T}}(0^\circ)$ is the normal reflection from the aluminum plate. In references [150], [155], the RCS of the target is separated from the background reflection based on its Doppler-shifted radar return, which can be considered analogous to the Fourier technique presented here.

5. 3. 2 Reflectivity measurements

Figure 5-4 shows samples of absorbers and the reflection from commercial absorber TERASORB-500 [156] at 650 GHz. The normal reflection from the aluminum plate is at 0-dB level at zero angle. In case of the sample size of 100 × 100 mm^2, such as the TERASORB-500, the quiet zone diameter becomes larger than the projected diameter of the target

$$D_{\mathrm{proj}} = D|\cos(\theta)|, \tag{5.4}$$

when the incident angle θ is increased. For zero-thickness samples, this results in spill-over loss $|\cos(\theta)|$, and it is 3 dB at 45° incidence angle. The reflectivity is measured up to an incidence angle of 12.5° at 650 GHz and 45° at 310 GHz. At 12.5° the spill-over loss is 0.2 dB only. The sample thickness in case of TERASORB-500 is approximately 20 mm, and reflections at 90° and 270° are due to the vertical edge of the aluminum plate. The reflections at 50° and 310° are due to other exposed details of the sample.

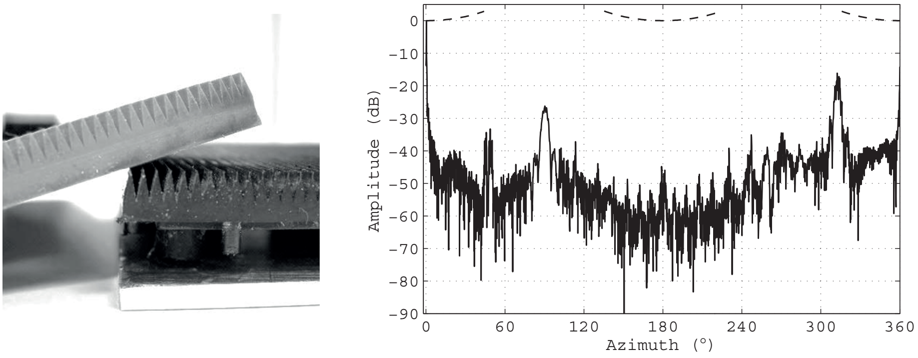

a) b)

Figure 5-4. a) Samples of commercial absorber: FIRAM-500 (on top) and TERASORB-500 (at bottom) [157]. The aluminum plate and TERASORB-500 have total height of 20 mm when prepared for measurement. b) The measured 650-GHz reflectivity of TERASORB-500. The amplitude is normalized to zero angle, i.e., to the full reflection from the aluminum plate. Normal incidence to the absorber occurs at 180°. The spill-over loss (dashed) is 3 dB with incidence angle of 45° to the normal of absorber or aluminum surface. The spill-over loss in valid only for zero-thickness target, in practice, considerable reflection occurs from the side of the target.

The measured materials in [VI] and [VII] include the commercial millimeter- and submillimeter-wave RAM as well as synthetic and wool carpet materials. The carpet materials are studied for use in a large-scale hologram-based CATR reported in [20]. When hundreds of square meters of radar absorbing material are used, the cost of the materials becomes a significant factor in a temporary CATR. Compared to the absorber especially tailored for submillimeter waves, carpet material is tens of times less expensive.

The measured reflectivity of the commercial RAM is found to be lowest of the measured samples. The maximum reflectivity is from −56 to −26 dB at 310 GHz and from −54 to −37 dB at 650 GHz. The commercial absorbers have their maximum reflectivity at normal incidence. For commercial absorbers with a wedged structure, the absorber behaves like a diffraction grating, and the maxima occur according to the directions of Bragg's diffraction maxima. The maxima occur only when the wedges are parallel to the rotation axis of the sample, and they are stronger at 310 GHz rather than at 650 GHz. Since the baseline of the reflectivity is similar at both frequencies, it is suspected that the wedges appear more aperiodic at 650 GHz due to imperfect fabrication. Also, Bragg's maxima are broadened at the higher frequency, suggesting less coherent reflection from the tips of the wedges. Bragg's maxima can be seen in Figure 5-4 b) close to the normal incident angle. The maxima occur with condition

$$n\lambda = 2d \sin\theta_{\mathrm{Bragg}}, \tag{5.5}$$

where $n = 0, \pm1, \pm2, \pm3 ...$, wedge spacing is $d \approx 1.5$mm, and θ_{Bragg} is the angle of Bragg's maximum defined from the normal of the sample surface. The measured Bragg's maxima occur, e.g., at $\theta_{\mathrm{Bragg}} \approx -26.9°, -17.6°, -9.7°, 0°, 8.9°, 17.9°$, and $27.4°$, which are on average closer than 0.5° to the theoretical values.

The measured reflectivity of the carpets is found to have a rapid variation of 10-15 dB as a function of the incidence angle at both frequencies. When the transmittance through the carpet is low, the maximum reflectivity is −40 and −50 dB at 310 and 650 GHz, respectively. In case of high transmittance, the reflection from the aluminum plate behind the sample increases the measured reflectivity.

In addition to measurements at 584 GHz in [158], the reflectivity studies reported here and in [VI], [VII], [27] are the only off-boresight measurements of RAM reflectivity at this high frequency. The measurements are done in far-field conditions, and coherent effects from periodic structures can therefore be measured. Polarimetric RCS-range measurements for absorbers are reported also in [159] at 160 GHz. There, the absorber surface is also imaged with synthetic aperture radar. Bistatic reflectivity measurements have been reported in at millimeter-wave in [160], and at submillimeter-wave in [161], [162]. Normal reflectivity of absorbers is studied at submillimeter waves in [163], [164].

5. 3. 3 Measurement dynamic range

The smallest measurable reflectivity level is limited by the dynamic range in the RCS range. The dynamic range is defined as the amplitude ratio of the full reflection from the aluminum plate and the noise floor. The unprocessed maximum SNR is 79 dB and 72 dB in the 310-GHz and 650-GHz measurements. The maximum SNR in the setup is limited by the spillover loss in the hologram illumination, and the two-way losses in the beam splitter and hologram. The maximum SNR in the setup is achieved in a condition, where the aluminum plate is directed for normal incidence with the quiet-zone field. The very high maximum SNR is possible due to the fact that the free-space loss applies only to the path from the feed to the hologram, and not to the path from the hologram to the target.

The minimum measurable reflectivity level is modeled numerically by calculating the reflection from (5.2) and (5.3) and adding Gaussian noise to adjust the SNR to the measured values. The reflectivity error is defined as

$$\Delta\Gamma = \frac{|\Gamma_{\mathrm{model}}|}{|\Gamma|}, \tag{5.6}$$

where Γ_{model} is the modeled reflectivity measurement and Γ is the assumed reflectivity. Figure 5-5 shows calculated average reflectivity error for the two frequencies. The error increases to 1 dB at the reflectivity level of −96 and −85-dB, at 310 and 650 GHz. Due to processing gain, the error is small well below the unprocessed dynamic range of the measurement.

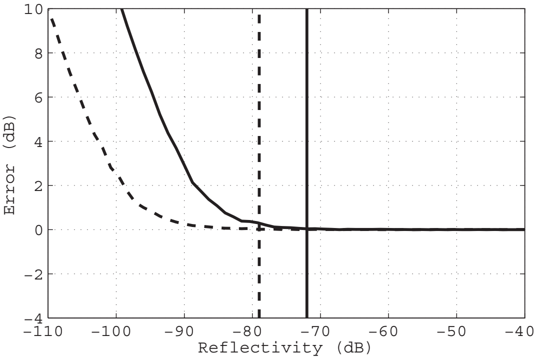

Figure 5-5. Estimated average error in measured reflectivity level as a function of the target reflectivity. The curves are from a Monte Carlo –run with 5000 repetitions. The vertical lines show the unprocessed dynamic range of the measurement system. The solid line marks the measurement at 650 GHz and the dashed line at 310 GHz.

5. 3. 4 Alignment accuracy

The reflection from the aluminum plate is highly directive, and even small errors in the alignment result in significant errors in the calibration of the reflectivity level. The reflection from a smooth plate varies as

$$|\mathbf{E}_{\mathrm{T}}(\theta)| \approx \mathrm{sinc}^2(kR_{\mathrm{RCS}}\sin(\theta)), \tag{5.7}$$

where R_{RCS} is the smaller of the radius of the quiet zone or the size of the plate. Figure 5-6 shows the amplitude of the back-reflected field as a function of the incidence angle. Depending on the size of the target and frequency, the amplitude drops 1 dB at an angle of 0.04° (650 GHz) and 0.10° (310 GHz).

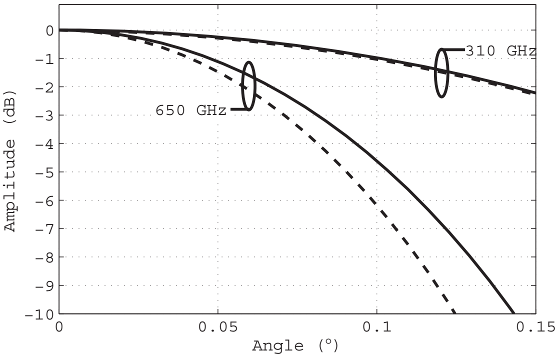

Figure 5-6. Amplitude of $\mathbf{E}_\mathrm{T}$ as a function of the incident angle. The amplitude is calculated using the measured quiet zone and the two plates used in the measurements at 310 and 650 GHz. The amplitude is shown both for azimuth (dashed) and elevation (solid). In the 310-GHz case the two coincide, due to the almost equal beamwidth in the both directions.

Figure 5-7 shows the measured amplitude at 650 GHz when the aluminum plate is aligned for normal incidence angle. The measurement is repeated for several samples. The amplitude is a periodic function of z-position due to the interference of the two components in (5.2). The amplitude is very similar between replacements of a new absorber sample. Figure 5-8 shows the amplitude of reflection from the plate at spatial frequency of $2k$. The results differ 2 dB at maximum. In addition to the alignment error, the deviation between the samples is caused by drift in the network analyzer. However, drift is not significant as the absorber sample measurement is immediately followed by the measurement of the aluminum plate.

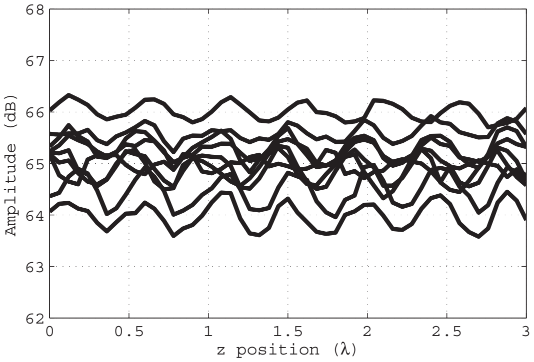

Figure 5-7. Repeated measurement of the reflection from the aluminum plate at normal incidence. The aluminum plate is taken away and put back each time between the measurements.

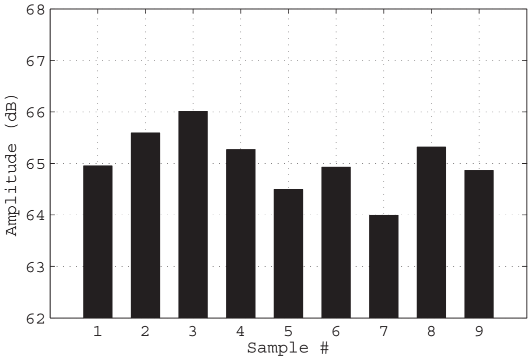

Figure 5-8. The processed reflection from the aluminum plate with normal incidence angle. The levels differ from each other 2 dB at maximum.

5. 4 Summary

In this chapter, the submillimeter-wave phase holograms are discussed. The holograms can be used to create a desired wave front from a given input beam. In this case, planar wave fronts are created from the Gaussian beam radiated by a corrugated horn antenna. The holograms can be used in a compact antenna or RCS measurement range. Two types of holograms are studied in this work: a reflection-type phase hologram at 310 GHz and a transmission-type phase hologram at 650 GHz. The phase holograms have excellent efficiency, and they are therefore suitable for RCS measurements.

The hologram-based RCS range is used to study the reflectivity of material samples. There, the sample is placed on an aluminum plate in the quiet zone of the hologram. The back-reflected signal is measured in a radar configuration. The small reflection from the RAM is separated from the background reflection by modulating it with a translational movement. The reflectivity measurement is calibrated by a comparison to the full reflection from an aluminum plate. The misalignment of the plate results to a systematic error in the reflectivity level. In the experiments presented here, the reflectivity measurement accuracy is estimated to be better than ±1 dB. The dynamic range of the reflectivity measurement is excellent due to high SNR and the additional processing gain.

The carpet materials compare well with the tailored commercial absorbers in reflectivity measurements: some of them reflectivity from −60 to −40 dB. Typically, carpet absorbers do not exhibit any kind of trend in the reflectivity; rather it is seemingly random function of the incidence angle. The commercial absorbers have low reflectivity from −60 to −50 dB, except to the direction of Bragg’s maxima in case of periodic structure on the RAM. The focus of the reflectivity studies presented here is in radar-absorbing materials for antenna measurements. However, the measurement technique is well suited also for studying imaging phenomenology at submillimeter wavelengths. Especially in case of every-day materials with varying material properties, the reflectivity of the targets must be experimentally determined.

6 Bolometers in submillimeter-wave imaging

Bolometers have been used for power detection across the electromagnetic spectrum. The pioneering work on bolometers took place in late 1870’s, when Langley observed resistance change in blackened platinum wires due to absorbed radiation. Since then, the bolometers have attracted a lot of interest as simple power detectors [165]. The integration time in bolometers is set by the thermal inertia of the device. Before introduction of the transition-edge bolometer (TEB) [166], [167], a typical integration time was too long for real-time applications, such as imaging. TEB is used in a passive submillimeter-wave imaging system [31], [168], [169].

To achieve wide-band operation, the bolometers are connected to an equi-angular spiral antenna [170]. The antennas and bolometers are fabricated on a silicon substrate, and the radiation is coupled to the detector through a silicon substrate lens. The bolometers are used as detectors in a focal plane array of a near real-time imaging system, and for transition-edge operation, they are cooled to cryogenic temperature.

In this chapter, and in [VIII], [171], the bolometers are characterized in room-temperature measurements at 321-782 GHz. The directional patterns of the bolometers are measured at submillimeter wavelengths. Also, an ad hoc power detector is characterized.

6. 1 Passive imaging system

The bolometers are used in a linear FPA in a passive submillimeter-wave imaging system. The FPA has 64 bolometers and the image is focused with a spherical mirror. In order to have a compact system, the quasioptics is folded with planar mirrors. A photograph of the system, sketch of the quasioptics, and a video snapshot are shown in Figure 6-1. The beams for each bolometer are rotated in the FoV so that approximately 10000 pixels result in the final image at up to 10-Hz frame rate. The rotation of the beams is realized with a conical scanner [172]. The camera has a 8-m stand-off range and 2 × 4-m^2 FoV with better than 3-cm cross-range resolution [31], [173]. The NEP in the video-rate images is 0.6 K. An improved system with a 128-element FPA is described in [48]. A concept of a 186-element FPA with bolometers tuned for three different sub-bands is presented in [174].

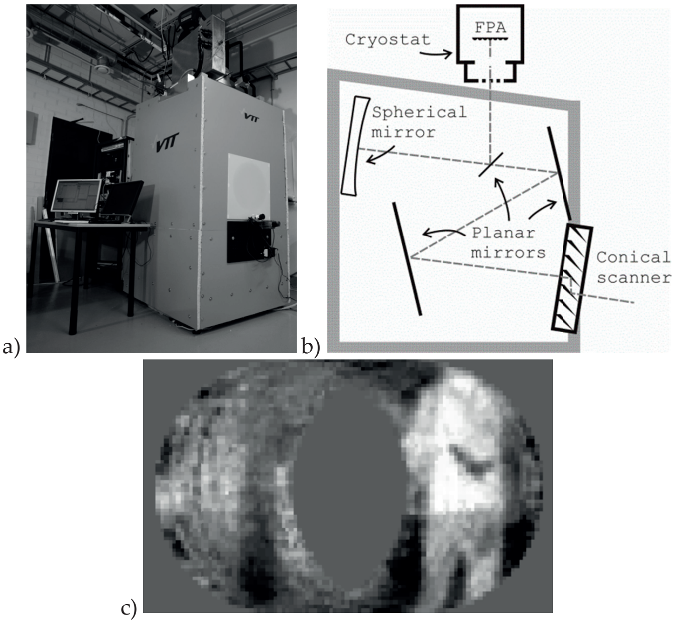

Figure 6-1. a) Passive real-time imaging system. b) The arrangement of the quasioptics in the system. The bolometers are in the cryostat atop. The conical scanner consists of parallel mirrors rotating in perpendicular to the optical axis [31]. c) A snapshot from a real-time video taken with the imaging system. The video-rate NEP in the image is 0.6 K, [173].

6. 2 Antenna-coupled microbolometer and substrate lens

The FPA in [31] consists of modules each including eight bolometers. A photograph of the modules is shown in Figure 6-2. The detector spacing in the module is 3 mm and the lens diameter, D, is approximately 2 mm. The lenses and substrate are enclosed in a metallic module so that mechanical pressure connects the biasing lines to the bolometers. Also, the module is designed to provide a thermal ground for the bolometers in the cryogenic operation.

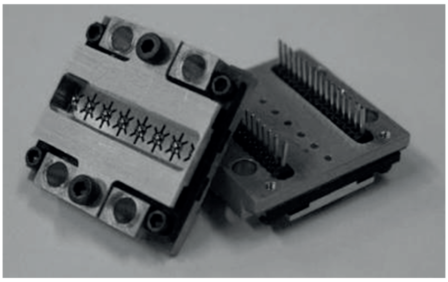

Figure 6-2. Photograph of the bolometer modules. The silicon substrate with bolometers and the substrate lenses are pressed together with a stainless steel sheet with openings for the lenses.

6. 2. 1 *Hyper-hemispherical lens*

The bolometers and antennas are fabricated on a silicon substrate. Due to the high permittivity, radiation from the antenna is directed into the substrate. As the substrate is substantially thick, substrate modes are possible and coupling from the free space to the antenna can be distorted. Excitation of the substrate modes can be avoided by adding a lens on the back side of the substrate [175]. A hyper-hemispherical lens design is preferred, since it allows for a good matching to the fundamental Gaussian mode, [176], [177]. The condition for the hyper-hemispherical lens height is

$$h_{\mathrm{hyper}} = \left(1 + \frac{1}{\sqrt{\varepsilon_{\mathrm{r}}}}\right) R_{\mathrm{l}}, \tag{6.1}$$

where $\varepsilon_{\mathrm{r}} = 11.9$ is the dielectric permittivity of silicon, and $R_{\mathrm{l}} = 1020$ µm is the radius of curvature of the lens surface. The lens array in the bolometer module is realized so that an additional lens cap is placed on top of the substrate. The substrate and the lens cap have total height of 1345 µm, so the lenses are close to the hyper-hemispherical height of $h_{\mathrm{hyper}} \approx 1316$ µm. The assembly of lenses, substrate, and antenna-coupled bolometers is shown in Figure 6-3.

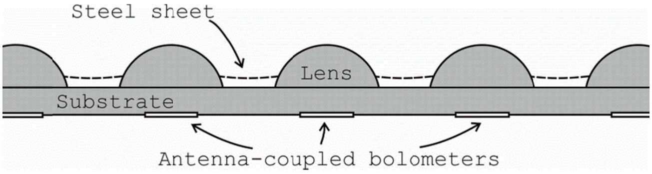

Figure 6-3. Lenses, substrate, and antenna-coupled bolometers inside the module. The steel sheet presses the lenses against the substrate.

6. 2. 2 *Equi-angular spiral antenna*

To achieve wide-band detection, a non-resonant antenna is used. The equi-angular spiral antenna is self-complementary, and thus has constant impedance over the bandwidth [170], [178]. The terminal impedance of the self-complementary antenna on the substrate-air interface is

$$Z_{\mathrm{SC}} = \sqrt{\frac{\mu_0}{4\varepsilon_0\varepsilon_{\mathrm{eff}}}} \approx 74\ \Omega, \tag{6.2}$$

where $\varepsilon_{\mathrm{eff}} = (\varepsilon_{\mathrm{Si}} + \varepsilon_{\mathrm{Air}})/2 \approx 6.45$ is the effective permittivity. The impedance is closely matched to the bolometer resistance in the cryogenic operation [168].

The equi-angular spiral antenna operates over a wide bend and is circularly polarized in the design band. The edge of the conductor spiral can be described with the radius

$$r(\Phi) = r_0 e^{a_{\mathrm{eq}}\Phi}, \tag{6.3}$$

where $r_0 \approx 36$ µm is the spiral starting radius, Φ is the opening angle, and $a_{\mathrm{eq}} \approx 0.37$ describes the opening rate of the spiral. The antenna is shown in Figure 6-4.

Circularly polarized antenna is compatible with the detection of non-polarized radiation in passive imaging. Outside the band, polarization becomes elliptical. The lower cut-off frequency of the equi-angular spiral antenna corresponds to the frequency, when the arm length of the spiral is one wavelength. The antenna arm length is given by

$$L_{\mathrm{eq}} = \sqrt{\alpha^{-2}+1}\,(r_{\mathrm{max}} - r_{\mathrm{min}}), \tag{6.4}$$

where α is spiral opening rate, and r_{max} , r_{min} are the maximum and minimum of the center radius of the arm [170]. In this work the arm length is 570 µm, and it corresponds to the effective wavelength at 200 GHz. The upper cut-off frequency depends on the fine structure of the antenna terminal, and it is expected to be of the order of 1000 GHz.

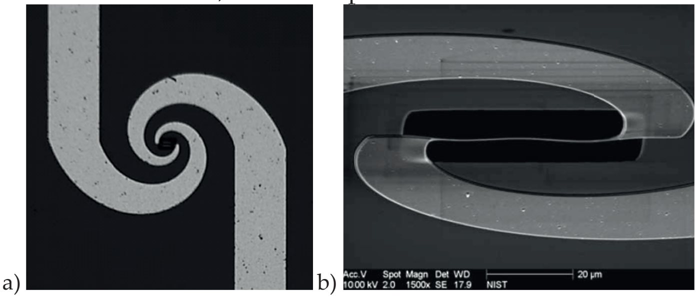

Figure 6-4. a) Equi-angular spiral antenna on the silicon substrate. The vertical strips are for biasing the bolometer. Co-polar direction is defined to be along the vertical. b) NbN-bolometer suspended across the antenna terminal. The antenna is made of aluminum.

6. 2. 3 Transition-edge bolometer

The bolometer is a lithographically fabricated niobium-nitride air bridge [179]. The bolometer is suspended in the terminal of the equi-angular spiral antenna. In its operation as a TEB, the bolometer modules are cooled down to below 10 K. The NbN-air-bridges are in superconducting state. When the bolometers are biased, the ohmic heating holds the center part of the bolometer in a resistive state. When the bolometers are voltage-biased, the dissipated power in it is nearly constant. When the heating due to incident radiation increases, the negative electro-thermal feedback reduces ohmic heating. The heat load on the air bridge remains constant. The bolometer noise-equivalent power (NEP) in cryogenic operation is down to 7 fW/Hz$^{1/2}$.

In room temperature, the sensitivity of the bolometers is significantly reduced. The detection of the incident radiation is based on the linear change of the resistance according to the temperature coefficient of the resistivity of the air bridge. The measured change in resistance is shown in Figure 6-5 as a function of biasing power, when no submillimeter-wave power is present.

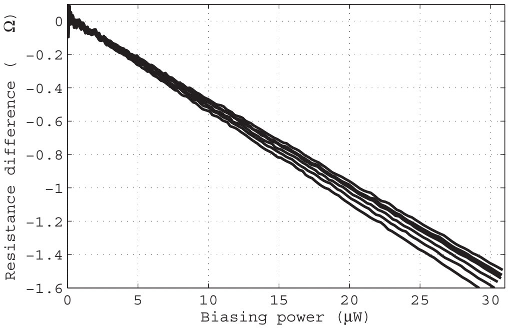

Figure 6-5. The change in the bolometer resistivity as a function of DC biasing power. Seven bolometers in one module are measured at room temperature.

6. 3 Beam-pattern measurements

The directional patterns of the bolometers are measured in the power measurement range described in Section 2. 5. 2. The modules are placed on an azimuth-elevation scanner so that the center of rotation coincides with the bolometer being characterized. Two separate modules are used in the measurements.

The beam patterns are measured from 321 to 782 GHz, with 2-dimensional measurements at selected frequencies and a frequency sweep for one-dimensional beam pattern cuts [VIII]. Table 6-1 lists the measured −3-dB beamwidth and dynamic range at selected frequencies. When normalized with factor λ/D, the beamwidth ranges from 0.85 to 1.20. This indicates that the beamwidth is not only according to the size of the free aperture of the lens, but also the structure surrounding the lens affects the beam patterns. The theoretical beamwidth for an uniformly illuminated circular aperture is $1.02\,\lambda/D$.

Table 6-1. The beamwidth and dynamic range of the measurement at selected frequencies for a central bolometer in the module.

Frequency (GHz)	**Beamwidth (°)**	**Normalized beamwidth (λ/D)**	**Dynamic range (dB)**
321	25.3	0.85	13
400	20.9	0.88	15
654	17.5	1.20	25
782	12.2	1.00	17

The trend of the beamwidth is measured in a frequency sweep from 321 to 500 GHz. The azimuth cut is measured at 19 different frequency points, and the beamwidth is determined for each cut. A function inversely proportional to the frequency is fitted to the measured beamwidth, and it results in a beamwidth-frequency –relation

$$\theta_{-3dB} \approx \frac{8.5^{\circ}\mathrm{THz}}{f}. \tag{6.5}$$

Similar trend in results are obtained also in [180] with slightly different bolometers. There, the lens diameter is 4 mm, and the measurement frequencies are 95, 238, and 650 GHz. The normalized beamwidth for those bolometers ranges from 0.52 to 1.00 as the frequency increases.

6. 3. 1 Bolometer-to-bolometer variation

The bolometers and lenses are intended to be centered. However, due to mechanical inaccuracy in assembling the bolometers, unintended beam steering occurs. The bolometer-lens misalignment can be approximated by Snell's law

$$\Delta b = h \times \tan\left(\sin^{-1}\left(\frac{\sin\theta_{\mathrm{off}}}{\sqrt{\varepsilon_{\mathrm{Si}}}}\right)\right), \tag{6.6}$$

where h is the height of the lens and θ_{off} is the offset angle from boresight [177]. Figure 6-6 a) shows the measured main beam directions. The offset angle can be up to 7° from the boresight, corresponding to misalignment of 47 µm. The beam offset occurs systematically for each bolometer in one module: the variation of the offset angle for different beams from one module is less than 3°. The alignment of the lens is made easier by etching a shallow pit to the substrate. However, for practical reasons, the pit must be larger than the lens, which leaves possibility for misalignment.

The amplitude ratio between the bolometer main beams in a single module is shown in Figure 6-6 b). The measured main-beam amplitude varies up to 2.2 dB peak-to-peak. The main beam amplitude corresponds to the amplitude measured in directions shown in Figure 6-6 a).

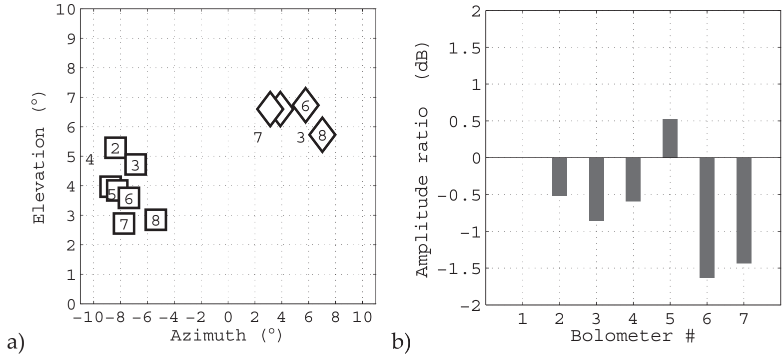

Figure 6-6. a) Main beam directions for bolometers in two different modules. Seven bolometers are characterized from one module (squares) and four from another (diamonds). b) Main beam amplitude ratio between seven bolometers in a single module. The amplitude is normalized to bolometer #1.

6. 3. 2 Measurement accuracy

The measurement of the beam pattern is repeated for a single bolometer at 779 GHz. The measurements are separate so that the bolometer module is taken apart from and put back to the measurement setup between the measurements. The difference between the two beam pattern measurements is less than 0.5 dB down to the −10-dB level of the measured pattern, as is shown in Figure 6-7.

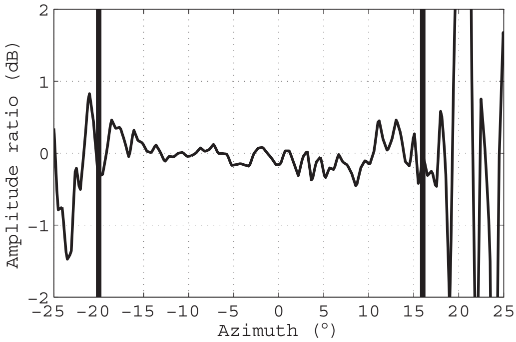

Figure 6-7. Difference of two beam pattern measurements for a central bolometer in a single module. The vertical lines mark the −10-dB level in the beam pattern.

6. 4 Ad hoc detector for submillimeter waves

In addition to bolometers, commercial mid-infrared detectors are studied for use in power detection [IX]. The detectors are originally intended for passive infrared (PIR) applications, such as motion detection at wavelengths of 5-15 μm. Few publications have pointed out the suitability of infrared detectors for submillimeter-wave detection, e.g., [181], [182], [183], [184]. The detectors are based on pyro- or thermoelectric effects.

6. 4. 1 Pyroelectric power detector

In this work, the pyroelectric detector is compared with two commercial power meters and room-temperature microbolometers. A pyroelectric detector Murata IRA-E700ST0 is studied [185]. The detector consists of pyroelectric material placed between the capacitor plates. The electrical potential across the capacitor changes on temperature change, so the detector is AC-coupled and can be used to detect chopped power. The pyroelectric detectors tailored for submillimeter-wave detection have the same principle of operation as the infrared detectors [186], [187]. The detectors differ only for their window materials and the absorbing properties. The operation principle and a photograph of the pyroelectric detector are shown in Figure 6-8.

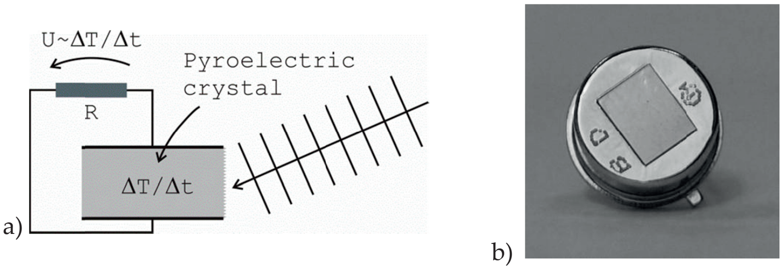

Figure 6-8. a) Operation principle of the pyroelectric detector. The incident radiation is absorbed to the pyroelectric crystal. The temperature of the crystal changes and the change induces an electric potential across the capacitor plates. The potential change is sensed across a large resistor integrated into the sensor. b) A photograph of the Murata IRA-E700ST0 detector.

6. 4. 2 *Measurement results*

In addition to beam pattern measurements at 625, 784, and 814 GHz, the sensitivity and noise-equivalent power of the pyroelectric detector is compared to that of commercial power meters, the Golay cell [188] and a quasioptical power meter [91]. Also, the sensitivity of the room-temperature bolometers is studied.

Since the pyroelectric detector does not have an optimized antenna structure and the detector is located in a cavity behind a silicon window, the beam patterns are strongly dependent on the frequency. However, the boresight response of the detector is similar to that of the Golay cell at 625-814 GHz. Also, the SNR of the measurement with the pyroelectric detector is always more than 20 dB. The response is shown in Figure 6-9. The sensitivity and NEP of the pyroelectric detector is estimated by comparing its performance to that of the Golay cell given by the manufacturer. The sensitivity and NEP of the ad hoc detector is found to be 1700 V/W and of 0.4 ◎W/Hz½, respectively.

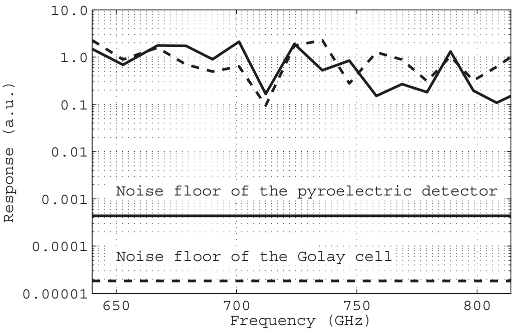

Figure 6-9. The responses from the pyroelectric detector (solid) and the Golay cell (dashed).

6. 5 Summary

In this chapter, antenna-coupled microbolometers are studied. The bolometers are used in the focal plane array of a passive submillimeter wave imaging system. When cooled to cryogenic temperature, the bolometers operate in the transition-edge mode. Then, the bolometers become extremely sensitive power detectors. The bolometers are fabricated on a silicon substrate, and the power is coupled to them through a substrate lens and a wide-band antenna.

The characterization reported here is made at room temperature. The beam patterns of the bolometers are measured at 321-782 GHz. Compared to the measurements made elsewhere with substrate-lens antennas [180], similar behavior is observed. Due to the compact structure of the substrate lens and the module housing it, the beam patterns deviate from the known $\propto \lambda/D$ behavior at the low end of the frequency range. Also, measurement accuracy as well as the deviations due to fabrication and assembly is studied with repetitive measurements. The measurement of the beam pattern is repeated with differences less than 0.5 dB in amplitude.

Finally, an ad hoc power detector is characterized: a mid-infrared detector is compared to commercial power detectors at submillimeter waves. It is concluded that the detector is well suited to, at least, power-indication purposes.

7 Summary of the publications

7. 1 Indirect holographic imaging

In [I], the indirect holographic method is experimentally verified at 310 GHz for the first time. The experimental setup consists of a network analyzer, and hologram measurements are carried out as raster scans with a planar near-field scanner. A spherical reference wave is illuminating the hologram from an offset angle. In [II], methods for evaluating the image quality at submillimeter waves are introduced and tested with the indirect holographic imaging experiment. Standardized test targets are used to evaluate the point spread function and the image signal-to-noise ratio. In [III], the indirect holographic method is developed further by the spatial-domain –technique to retrieve the target wave. There, the indirect holographic method is no longer restricted by the reference wave incident angle.

7. 2 Reflectarrays

Millimeter-wave reflectarrays are discussed in [IV]. The reflectarrays are intended for a millimeter-wave imaging application. The reflectarray element design is described. Three reflectarrays are fabricated and they are tested in the near-field measurement range. In addition to the beam pattern measurements, also the aperture field of the reflectarrays is imaged. Aperture field imaging allows for estimating the reflectarray efficiency, which is an important quantity especially for reflectarrays with element spacing larger than half a wavelength.

The measured performance of the reflectarrays is close to the simulation, when the observed fabrication errors are taken into account. The reflectarrays are fabricated on a polymer substrate and they are based on the conductor-backed coplanar structures. The fabrication process and materials are suitable for the future development of the reconfigurable reflectarray, and the static reflectarrays characterized are used as an engineering advice.

7. 3 Submillimeter-wave holograms and applications

In [V], the performance of a reflection-type phase hologram is characterized. In order to verify the performance of the fabricated hologram, the quiet-zone amplitude and phase is measured in a near-field measurement range. The holograms are suitable for compact radar-cross-section measurements due to their excellent efficiency.

In [VI] and [VII], the reflectivity of different radar absorbing materials is studied. The reflectivity is measured in a hologram-based compact RCS measurement. The results of the measurements are used to provide information on low-cost absorbing materials at submillimeter waves. A full-scale compact antenna test range measurement campaign has been carried out with a carpet material as RAM [20].

7. 4 Bolometers in submillimeter-wave imaging

In [VIII], antenna-coupled microbolometers are characterized in an antenna measurement range. The beam patterns of the detector are measured at point frequencies across the submillimeter-wave band in order to find out the behavior of the beamwidth as a function of frequency. The relatively simple detectors are fabricated lithographically, and their performance might be degraded due to fabrication errors. The results of the measurement improve the understanding of, e.g., effect of fabrication tolerances to the main beam direction and especially the behavior of the beam patterns, when the lens size is comparable to the wavelength.

In [IX], a commercial infrared detector based on the pyroelectric effect is characterized at submillimeter waves. The beam pattern measurements are done in the power measurement range at point frequencies from 625 to 814 GHz. The pyroelectric detector is compared to dedicated power meters, and its noise-equivalent power and sensitivity is estimated by comparing its response to that of a Golay cell. It is found that the detector has reasonable agreement with the response of the Golay cell. The results from this publication indicate that this kind of ad hoc power detector could be very useful for uncalibrated power measurement.

8 Conclusions and future work

This doctoral thesis focuses on millimeter- and submillimeter-wave imaging. Also, partly overlapping with the field of imaging, the thesis discusses on material reflectivity studies and power detector characterization. The thesis is based on the research work reported in publications [I]-[IX]. The scientific background, findings made by the author, and comparative review of the achieved results are summarized in Chapters 1-7.

Millimeter- and submillimeter-wave imaging has been a subject of intensive research since the discovery of its usefulness for Earth science and radio astronomy decades ago. Later, due to progress mainly in semiconductor technology, commercial millimeter-wave applications have emerged and they are breaking through to large-scale use. At the high end of millimeter waves and at submillimeter-waves, imaging is one of the most prospective applications. The propagation in that wavelength range is ray-like, and high-resolution imaging is possible with convenient aperture size. In addition to the immature level of technology and unavailability of, e.g., compact transceivers, the high atmospheric attenuation at submillimeter waves makes the development of applications difficult or prohibits operation in sea-level conditions. To counter-act the limitations, this thesis describes applications and methods, which provide alternatives to some of the conventional and more complex approaches.

Imaging at millimeter and submillimeter waves is widely applied in a scenario, where a single state-of-art receiver or transceiver is focused on the target and image is formed with pixel-by-pixel mechanical movement. While the approach is sufficient for imaging stationary target, it is very difficult to speed up for applications, where near real-time imaging is needed. A few submillimeter-wave imaging systems have applied a focal plane array, where each detector counts for a pixel in the image; the number of detectors ranges from tens to a hundred. The pixel count is then multiplied by a fast mechanical scanning. Current submillimeter-wave imaging systems are capable of imaging human-sized targets at 10 frames per second. This fast imaging and detector count is currently possible with direct detectors only, and most near-real time imaging systems are based on the passive detection of the target brightness temperature. In passive imaging, the detectors need to be wide-band due to the low spectral power density at submillimeter waves. A typical detector in passive submillimeter-wave imaging is a superconductive transition-edge bolometer. In this thesis, antenna-coupled microbolometers are characterized in room temperature at 321-782 GHz. Their beam patterns are measured in a power measurement range at point frequencies across their intended operation band. A beamwidth-frequency relation of 8.5°/THz is found for a 2-mm substrate lens. Also ad hoc power detectors are compared to commercial submillimeter-wave power meters. They are found to be wide-band and their sensitivity at submillimeter waves is sufficient at least for power indication purposes. A new generation of bolometers for the passive detection will allow more discrimination in the spectral domain, as the antenna-coupled bolometers are being designed for sub-bands also. At the same time, the characterization of the bolometers in spectral domain becomes important. In the future work, spectroscopic measurements at cryogenic temperature will be carried out.

This thesis presents the indirect holographic method as an alternative to the active imaging scenarios, where coherent detection is provided by heterodyne receivers. In the holographic method, only direct detection is required and simpler detectors, such as the bolometers, can be used. Using a non-focused array allows for a computational image focusing, whereas those imaging systems with FPA are focused to fixed distance. In the thesis, indirect holographic method is verified at 310 GHz. Also, the achieved image quality is assessed based on the measured point spread function. Standardized image quality metrics allows for fair comparison between different imaging systems and methods. With this experimental setup, the resolution is estimated to be 20-30 % lower than the theoretical. The indirect holographic method is now proven at submillimeter waves. In the future work, instead of a vector network analyzer, a custom direct detector, or preferably an array of detectors, is required to verify the estimates of the required link budget.

A millimeter-wave reflectarray shares some of the advantages of a reflector antenna and a phased array. The feeding of the elements in reflectarrays is done quasioptically and no loss due to a waveguide network is present. A reconfigurable reflectarray with electrically controllable phase shifters allows for rapid beam steering. Only one transceiver is needed with the reflectarray, so the overall system cost is not burdened by the expensive array technology. The ultimate goal of the development is a reconfigurable reflectarray with thousands of elements on it. Design of such a device is a compromise between the designs of the antenna array and the controlling electronics. The static reflectarrays described in this thesis have a design that is compatible with the future reconfigurable reflectarray with the MEMS phase shifters. The reflectarrays are based on conductor-backed coplanar structures. The phase shift quantization and element spacing in the reflectarrays is selected to be compatible with the future control electronics. In this case, the reflectarray has element spacing greater than half a wavelength and 2-bit phase shifting. The reflectarray efficiency is reduced especially if the element spacing is large. The fabricated reflectarrays are characterized in a near-field range. When the known unidealities in the reflectarrays are taken into account, the performance of the reflectarrays is in line with simulation. The beamwidth of the reflectarray is up to 10 % broader than that of an ideal reflectarray. Also, the efficiency of the reflectarrays is 0.11 compared to the expected efficiency of 0.54. The reconfigurable reflectarray is under development. The MEMS-based phase shifters are realized at 120 GHz, and their integration to the reflectarray with the controlling electronics is underway. At the same time, 1-bit submillimeter-wave reflectarrays are being developed, and they are also envisioned to have integrated MEMS phase shifters.

Submillimeter-wave phase holograms have been characterized and applied in a compact RCS measurement range. The hologram collimates a spherical wave into a quiet zone, which corresponds to the conditions at the far-field distance. The deviations from a planar wave are measured to be ±1.5 dB and ±5° at 310 GHz and ±3 dB and ±25° at 650 GHz. The hologram at 310 GHz is reflection-type, and its measured efficiency is −3.6 dB compared to the simulated efficiency of −3.0 dB. The reflection-type phase hologram has superior efficiency, since the hologram is free of significant amplitude modulation, dielectric loss, or resonant effects.

The holograms allow for direct beam pattern or RCS measurements in a short range without limitation of the atmospheric attenuation. In this thesis, the hologram-based RCS range is used for measuring the reflectivity of radar absorbing materials. In addition to tailor-made submillimeter-wave absorbers, some every-day materials, such as carpets, have been found to have low monostatic reflectivity from −60 to −40 dB. The tailor-made radar absorbing material has a typical reflectivity from −60 to −50 dB, but for periodic materials, the reflectivity can be as high as ca. −30 dB in the directions of Bragg's maxima. The use of low-cost material in a full-scale reflector antenna test campaign reduces the cost significantly compared to the use of tailor-made radar absorbing materials.

References

[1] J. C. Wiltse, "History of millimeter and submillimeter waves," *IEEE Transactions on Microwave Theory and Techniques*, vol. 32, no. 9, pp. 118-1127, 1984.

[2] D. M. Mittleman, R. H. Jacobsen, and M. C. Nuss, "T-ray imaging," *IEEE Journal of Selected Topics in Quantum Electronics*, vol. 2, no. 3, pp. 679-692, 1996.

[3] P. H. Siegel, "Terahertz technology," *IEEE Transactions on Microwave Theory and Techniques*, vol. 50, no. 3, pp. 910-928, 2002.

[4] T. S. Rappaport, J. N. Murdock, and F. Gutierrez, "State of the art in 60-GHz integrated circuits and systems for wireless communications," *Proceedings of the IEEE*, vol. 99, no. 8, pp. 1390-1436, 2001.

[5] D. Doyle, G. Pilbratt, and J. Tauber, "The Herschel and Planck space telescopes," *Proceedings of the IEEE*, vol. 97, no. 8, pp. 1403-1411, 2009.

[6] A. Wootten and A. R. Thompson, "The Atacama large millimeter/submillimeter array," *Proceedings of the IEEE*, vol. 97, no. 8, pp. 1463-1471, 2009.

[7] J. F. Federici, B. Schulkin, F. Huang, D. Gary, R. Barat, F. Oliveira, and D. Zimdars, "THz imaging and sensing for security applications - explosives, weapons and drugs," *Journal of Semiconductor Science and Technology*, vol. 20, no. 7, pp. 266-280, 2005.

[8] K. B. Cooper, R. J. Dengler, N. Llombart, B. Thomas, G. Chattopadhyay, and P. H. Siegel, "THz imaging radar for standoff personnel screening," *IEEE Transactions on Terahertz Science and Technology*, vol. 1, no. 1, pp. 169-182, 2011.

[9] Z. D. Taylor, R. S. Singh, D. B. Bennett, P. Tewari, C. P. Kealey, N. Bajwa, M. O. Culjat, H. Lee, J. Hubschman, E. R. Brown, and W. S. Grundfest, "THz medical imaging: in vivo hydration sensing," *IEEE Transactions on Terahertz Science and Technology*, vol. 1, no. 1, pp. 201-219, 2011.

[10] C. M. Armstrong, "The truth about terahertz," *IEEE Spectrum*, vol. 49, no. 9, pp. 36-41, 2012.

[11] "Recommendation ITU-R P.676-9 Attenuation by atmospheric gases," ITU-R, June 2013. [Online]. http://www.itu.int/dms_pubrec/itu-r/rec/p/R-REC-P.676-9-201202-I!PDF-E.pdf

[12] R. C. Johnson, H. A. Ecker, and J. S. Hollis, "Determination of far-field antenna patterns from near-field measurements," *Proceedings of IEEE*, vol. 61, no. 12, pp. 1668-1694, 1973.

[13] J. Tuovinen, A. Vasara, and A. V. Räisänen, "A new type of compact antenna test range," in *Proceedings of the 22nd European Microwave Conference*, Espoo, Finland, 1992, pp. 503-508.

[14] J. Häkli, "Shaped reflector antenna design and antenna measurements at sub-mm wavelengths," Radio Laboratory, Helsinki University of Technology, Espoo, Finland, Doctoral Thesis 2006.

[15] T. Koskinen, "Studies on an amplitude hologram as the collimator in a submillimeter-wave compact antenna test range," Radio Laboratory, Helsinki University of Technology, Espoo, Finland, Doctoral Thesis 2007.

[16] J. Ala-Laurinaho, "Numerical studies on a radio frequency hologram and its use in antenna measurements," Radio Laboratory, Helsinki University of Technology, Espoo, Finland, Doctoral Thesis 2001.

[17] T. Sehm, J. Ala-Laurinaho, T. Hirvonen, and A. V. Räisänen, "Antenna measurements using a hologram CATR," *Electronics Letters*, vol. 35, no. 10, pp. 757-758, 1999.

[18] J. Ala-Laurinaho, T. Hirvonen, P. Piironen, A. Lehto, J. Tuovinen, A. V. Räisänen, and U. Frisk, "Measurement of the Odin telescope at 119 GHz with a hologram-type CATR," *IEEE Transactions on Antennas and Propagation*, vol. 49, no. 9, pp. 1264-1270, 2001.

[19] J. Häkli, T. Koskinen, A. Lönnqvist, J. Säily, V. Viikari, J. Mallat, J. Ala-Laurinaho, J. Tuovinen, and A. V. Räisänen, "Testing of a 1.5-m reflector antenna at 322 GHz in a CATR based on a hologram," *IEEE Transactions on Antennas and Propagation*, vol. 53, no. 10, pp. 3142-3150, 2005.

[20] A. Karttunen, J. Ala-Laurinaho, M. Vaaja, T. Koskinen, J. Häkli, A. Lönnqvist, J. Mallat, A. Tamminen, V. Viikari, and A. V. Räisänen, "Antenna tests with a hologram-based CATR at 650 GHz," *IEEE Transactions on Antennas and Propagation*, vol. 57, no. 3, pp. 711-720, 2009.

[21] R. C. Johnson, H. A. Ecker, and R. A. Moore, "Compact range techniques and measurements," *IEEE Transactions on Antennas and Propagation*, vol. 17, no. 5, pp. 568-576, 1969.

[22] H. A. Ecker and R. A. Moore, "Compact radar reflectivity ranges," Georgia Institute of Technology, Technical Report, 1968.

[23] J. Mallat, J. Ala-Laurinaho, E. Noponen, V. Viikari, A. Lönnqvist, T. Koskinen, J. Säily, J. Häkli, J. Meltaus, and A. V. Räisänen, "A phase hologram RCS range for scale model measurements," in *Digest of Technocal Papers, URSI/IEEE XXVII Convention on Radio Science*, Espoo, Finland, 2002, pp. 143-145.

[24] E. Knott, J. Shaeffer, and M. Tuley, *Radar Cross Section*, 2nd ed. Norwood, Massachusetts: Artech House, 1993.

[25] A. Lönnqvist, J. Mallat, E. Noponen, J. Ala-Laurinaho, J. Säily, T. Koskinen, J. Häkli, and A. V. Räisänen, "A phase hologram compact RCS range for scale model measurements,"in *Proceedings of the 3rd ESA Workshop on Millimetre Wave Technology and Applications*, Espoo, Finland, 2003, pp. 511-516.

[26] A. Lönnqvist, "Applications of hologram-based compact range: antenna radiational pattern, radar cross section, and absorber reflectivity measurements," Radio Laboratory, Helsinki University of Technology, Espoo, Finland, Doctoral Thesis 2006.

[27] A. Tamminen, A. Lönnqvist, J. Mallat, and A. V. Räisänen, "Transmittance and monostatic reflectivity of radar absorbing materials for CATR," in *Proceedings of The Second European Conference on Antennas and Propagation*, Edinbrough, United Kingdom, 2007, publication no. We4.11.4.

[28] R. Appleby and H. B. Wallace, "Standoff detection of weapons and contraband in the 100 GHz to 1 THz region," *IEEE Transactions on Antennas and Propagation*, vol. 55, no. 11, pp. 2944-2956, 2007.

[29] J. E. Bjarnason, T. L. J. Chan, and A. W. M. Lee, "Millimeter-wave, terahertz, and mid-infrared transmission through common clothing," *Applied Physics Letters*, vol. 85, no. 4, pp. 519-521, 2004.

[30] A. Luukanen and J. P. Pekola, "A superconducting antenna-coupled hot-spot microbolometer," *Applied Physics Letters*, vol. 82, no. 22, pp. 3970-3972, 2003.

[31] E. Grossman, C. R. Dietlein, J. Ala-Laurinaho, M. Leivo, L. Grönberg, M. Grönholm, P. Lappalainen, A. Rautiainen, A. Tamminen, and A. Luukanen, "Passive terahertz camera for standoff security screening," *Applied Optics*, vol. 49, no. 19, pp. 106-120, 2010.

[32] E. Heinz, T. May, D. Born, G. Zieger, S. Anders, G. Thorwirth, V. Zakosarenko, M. Schubert, T. Krause, M. Starkloff, A. Krüger, M. Schulz, F. Bauer, and H.-G. Meyer, "Passive submillimeter-wave stand-off video camera for security applications," *Journal of Infrared, Millimeter and Terahertz Waves*, vol. 31, no. 11, pp. 1355-1369, 2010.

[33] A. Iacono, A. Neto, G. Gerini, J. Baselmans, S. Yates, A. Baryshev, and H. Hoevers, "Kinetic inductance detectors based receiver array architectures for imaging at THz frequency," in *Proceedings of the 39th European Microwave Conference*, Rome, Italy, 2009, pp. 830-833.

[34] E. R. Brown, "A system-level analysis of Schottky diodes for incoherent THz imaging arrays," *Solid-State Electronics*, vol. 48, no. 10-11, pp. 2051-2053, 2004.

[35] R. Appleby and R. N. Anderton, "Millimeter-wave and submillimeter-wave imaging for security and surveillance," *Proceedings of the IEEE*, vol. 95, no. 8, pp. 1683-1690, 2007.

[36] J. W. Goodman, "Some fundamental properties of speckle," *Journal of Optical Society of America*, vol. 66, no. 11, pp. 1145-1150, 1976.

[37] D. M. Sheen, J. L. Fernandes, J. R. Tedeschi, D. L. McMakin, M. Jones, W. M. Lechelt, and R. H. Severtsen, "Wide-bandwidth, wide-beamwidth, high-resolution, millimeter-wave imaging for concealed weapon detection," in *Proceedings of SPIE, Passive and Active Millimeter-Wave Imaging XVI*, Baltimore, 2013, publication no. 871509.

[38] D. Sheen, D. McMakin, and T. Hall, "Near-field three-dimensional radar imaging techniques and applications," *Applied Optics*, vol. 49, no. 19, pp. 83-93, 2010.

[39] D. T. Petkie, C. Casto, F. C. De Lucia, S. R. Murrill, B. Redman, R. L. Espinola, C. C. Franck, E. L. Jacobs, S. T. Griffin, C. E. Halford, J. Reynolds, S. O'Brien, and D. Tofsted, "Active and passive imaging in the THz spectral region: phenomenology, dynamic range, modes, and illumination," *Journal of Optical Society of America B*, vol. 25, no. 9, pp. 1523-1531, 2008.

[40] C. Dietlein, A. Luukanen, F. Meyer, Z. Popovic, and E. Grossman, "Phenomenology of passive broadband terahertz images," in *Proceedings of 4th ESA Workshop on Millimetre-Wave Technology and Applications*, Espoo, Finland, 2006, pp. 405-409.

[41] K. B. Cooper, R. J. Dengler, N. Llombart, T. Bryllert, G. Chattopadhyay, E. Schlecht, J. Gill, C. Lee, A. Skalare, I. Mehdi, and P.H. Siegel, "Penetrating 3-D imaging at 4- and 25-m range using a submillimeter-wave radar," *IEEE Transactions on Microwave Theory and Techniques*, vol. 56, no. 12, pp. 2771-2778, 2008.

[42] P. H. Siegel and R. J. Dengler, "Terahertz heterodyne imaging part I: introduction and techniques," *International Journal of Infrared and Millimeter Waves*, vol. 27, no. 4, pp. 465-480, 2006.

[43] I. Ederra, R. Gonzalo, B. Alderman, P. G. Huggard, B. P. De Hon, M. C. van Beurden, A. Murk, L. Marchand, and P. De Maagt, "Sub-millimeter-wave imaging array at 500 GHz based on 3-D electromagnetic-bandgap material," *IEEE Transactions on Microwave Theory and Techniques*, vol. 56, no. 11, pp. 2556-2565, 2008.

[44] D. Glaab, S. Boppel, A. Lisauskas, U. Pfeiffer, E. Ojefors, and H.G. Roskos, "Terahertz heterodyne detection with silicon field-effect transistors," *Applied Physics Letters*, vol. 96, no. 4, 3 p., 2010.

[45] K. B. Cooper, "Submillimeter-wave imaging radar utilizing transceiver arrays," in *Proceedings of SPIE, Passive and Active Millimeter-Wave Imaging XVI*, Baltimore, MD, 2013, publication no. 87150A.

[46] B. B. Hu and M. C. Nuss, "Imaging with terahertz waves," *Optics Letters*, vol. 20, no. 16, pp. 1716-1718, 1995.

[47] P. F. Goldsmith, C.-T. Hsieh, G. R. Huguenin, J. Kapitzky, and E. L. Moore, "Focal plane imaging systems for millimeter wavelengths," *IEEE Transactions on Microwave Theory and Techniques*, vol. 41, no. 10, pp. 1664-1675, 1993.

[48] A. Luukanen, M. Grönholm, M. Leivo, H. Toivanen, A. Rautiainen, and J. Varis, "Measured performance of a high-resolution passive video-rate submillimeter-wave imaging system demonstrator for stand-off imaging," in *Proceedings of SPIE 8362, Passive and Active Millimeter-Wave Imaging XV*, Baltimore, 2012, publication no. 836209.

[49] H. Sherry, J. Grzyb, Y. Zhao, R. Al Hadi, A. Cathelin, A. Kaiser, and U. Pfeiffer, "A 1kpixel CMOS camera chip for 25fps real-time terahertz imaging applications," in *IEEE International Solid-State Circuits Conference Digest of Technical Papers (ISSCC)*, San Francisco, CA, 2012, pp. 252-254.

[50] J. Grzyb, H. Sherry, Y. Zhao, R. Al Hadi, A. Cathelin, A. Kaiser, and U. Pfeiffer, "Real-time video rate imaging with a 1k-pixel THz CMOS focal plane array," in *Proceedings of SPIE 8362, Passive and Active Millimeter-Wave Imaging XV*, Baltimore, MD, 2012, publication no. 83620C-1-12.

[51] E. Grossman, A. Luukanen, and A. J. Miller, "Terahertz active direct detection imagers," in *Proceedings of SPIE, Terahertz for Military and Security Applications II*, Orlando, FL, 2004, pp. 68-77.

[52] J. W. Lamb, "Miscellaneous data on materials for millimetre and submillimetre optics," *International Journal of Infrared and Millimeter Waves*, vol. 17, no. 19, pp. 1997-2034, 1996.

[53] D. Sheen, D. McMakin, and T. Hall, "Near-field three-dimensional radar imaging techniques and applications," *Applied Optics*, vol. 49, no. 19, pp. 83-93, 2010.

[54] A. Brahm, M. Kunz, S. Riehemann, G. Notni, and A. Tünnermann, "Volumetric spectral analysis of materials using terahertz-tomography techniques," *Applied Physics B: Lasers and Optics*, vol. 100, no. 1, pp. 151-158, 2010.

[55] S. Wang and X.-C. Zhang, "Pulsed terahertz tomography," *Journal of Physics D: Applied Physics*, vol. 37, no. 4, pp. 1-36, 2004.

[56] J. Pearce, H. Choi, D. M. Mittleman, and J. White, "Terahertz wide aperture reflection tomography," *Optics Letters*, vol. 30, no. 13, pp. 1653-1655, 2005.

[57] B. Gonzalez-Valdes, Y. Alvarez, J. A. Martinez, F. Las-Heras, and C. M. Rappaport, "On the use of improved imaging techniques for the development of a multistatic three-dimensional millimeter-wave portal for personnel screening," *Progress In Electromagnetics Research*, vol. 138, pp. 83-98, 2013.

[58] A. Dallinge, S. Bertl, and J. Detlefsen, "Coherent millimeter-wave imaging for security applications," in *Proceedings of the European Radar Conference*, Munich, Germany, 2007, pp. 28-31.

[59] P. Hannan, "The element-gain paradox for a phased-array antenna," *IEEE Transactions on Antennas and Propagation*, vol. 12, no. 4, pp. 423-433, 1964.

[60] W. L. Chan, M. L. Moravec, R. G. Baraniuk, and D. M. Mittleman, "Terahertz imaging with compressed sensing and phase retrieval," *Optics Letters*, vol. 33, no. 9, pp. 974-976, 2008.

[61] C. F. Cull, D. A. Wikner, and N. Joseph, "Millimeter-wave compressive holography," *Applied Optics*, vol. 49, no. 19, pp. 67-82, 2010.

[62] A. Bandyopadhyay, A. Stepanov, B. Schulkin, M. D. Federici, A. Sengupta, D. Gary, and J. F. Federici, "Terahertz interferometric and synthetic aperture imaging," *Journal of the Optical Society of America*, vol. 23, no. 5, pp. 1168-1178, 2006.

[63] S. Bertl, A. Dallinger, and J. Detlefsen, "Broadband circular interferometric millimetre-wave ISAR for threat detection," *Advances in Radio Science*, vol. 5, pp. 147-151, 2007.

[64] Z. Liu, K. Su, D. E. Gary, J. F. Federici, R. B. Barat, and Z. Michalopoulou, "Video-rate terahertz interferometric and synthetic aperture imaging," *Applied Optics*, vol. 48, no. 19, pp. 3788-3795, 2009.

[65] S. Bertil, A. Dallinger, and J. Detlefsen, "Interferometric focusing for the imaging of humans," *IET Radar, Sonar and Navigation*, vol. 4, no. 3, pp. 457-463, 2010.

[66] K. Su, Z. Liu, R. B. Barat, D. E. Gary, Z. Michalopoulou, and J. F. Federici, "Two-dimensional interferometric and synthetic aperture imaging with a hybrid terahertz/millimeter wave system," *Applied Optics*, vol. 49, no. 19, pp. 13-19, 2010.

[67] S. S. Ahmed, A. Schiessl, and L.-P. Schmidt, "A novel fully electronic active real-time imager based on a planar multistatic sparse array," *IEEE Transactions on Microwave Theory and Techniques*, vol. 59, no. 12, pp. 3567-3576, 2011.

[68] S. S. Ahmed, "Personnel screening with advanced multistatic imaging technology," in *Proceedings of SPIE, Passive and Active Millimeter-Wave Imaging XVI*, Baltimore, MD, 2013, publication no. 87150B.

[69] G. R. Lockwood and F. S. Foster, "Optimizing sparse two-dimensional transducer arrays using an effective aperture approach," in *Proceedings of Ultrasonics Symposium*, Cannes, France, 1994, pp. 1497-1501.

[70] T. Niu, W. Withayachumnanku, B. S.-Y. Ung, H. Menekse, M. Bhaskaran, S. Sriram, and F. Christophe, "Experimental demonstration of reflectarray antennas at terahertz frequencies," *Optics Express*, vol. 21, no. 3, pp. 2875-2889, 2013.

[71] H. Kamoda, T. Iwasaki, J. Tsumochi, T. Kuki, and O. Hashimoto, "60-GHz electronically reconfigurable large reflectarray using single-bit phase shifters," *IEEE Transactions on Antennas and Propagation*, vol. 59, no. 7, pp. 2524-2531, 2011.

[72] A. Tamminen, J. Ala-Laurinaho, D. Gomes-Martins, J. Häkli, P. Koivisto, M. Kärkkäinen, S. Mäkelä, P. Pursula, P. Rantakari, M. Sipilä, J. Säily, R. Tuovinen, M. Varonen, K. A. I. Halonen, A. Luukanen, and A. V. Räisänen, "Reflectarray for 120-GHz beam steering application: design, simulations, and measurements," in *Proceedings of SPIE, Passive and Active Millimeter-Wave Imaging XV*, Baltimore, MD, 2012, publication no. 836205.

[73] A. Luukanen, J. Ala-Laurinaho, D. Gomes M., J. Häkli, P. Koivisto, P. Pursula, Rantakari P., J. Säily, A. Tamminen, R. Tuovinen, and M. Sipilä, "Rapid beamsteering reflectarrays for mm-wave and submm-wave imaging radars," in *Proceedings of SPIE, Passive Millimeter-Wave Imaging Technology XIV*, Orlando, FL, 2011, publication no. 80220M.

[74] Z. Du, A. Tamminen, J. Ala-Laurinaho, J. Säily, P. Rantakari, A. Luukanen, and A. V. Räisänen, "Design and optimization of reconfigurable reflectarray element with MEMS phase shifter," in *Proceedings of the 7th European Conference on Antennas and Propagation*, Gothenburg, Sweden, 2013, pp. 2362-2366.

[75] A. Tamminen, J. Ala-Laurinaho, S. Mäkelä, D. Gomes-Martins, J. Häkli, P. Koivisto, P. Rantakari, J. Säily, R. Tuovinen, A. R. Luukanen, M. Sipilä, and A. V. Räisänen, "Near-field measurements of submillimeter-wave reflectarrays," in *Proceedings of SPIE, Passive and Active Millimeter-Wave Imaging XVI*, Baltimore, MD, 2013, publication no. 871506.

[76] The MathWorks, Inc. (2013, June) MATLAB and Simulink for Technical Computing - MathWorks. [Online]. http://www.mathworks.se/

[77] ANSYS, Inc. (2013, June) Ansoft HFSS. [Online]. http://www.ansys.com/Products/Simulation+Technology/Electromagnetics/High-Performance+Electronic+Design/ANSYS+HFSS

[78] J. A. Stratton and L. J. Chu , "Diffraction theory of electromagnetic waves," *Physical Review Letters*, vol. 56, no. 1, pp. 99–107, 1939.

[79] J. A. Ratcliffe, "Some aspects of diffraction theory and their application to the ionosphere," *Reports on Progress in Physics*, vol. 19, no. 1, pp. 188-267, 1956.

[80] J. W. Goodman, *Introduction to Fourier Optics*.: McGraw-Hill Book Company, 1968.

[81] C. A. Balanis, *Antenna Theory, Analysis and Design*, 2nd ed. New York, USA: Wiley, 1997.

[82] A. D. Yaghjian, "An overview of near-field antenna measurements," *IEEE Transactions on Antennas and Propagation*, vol. 34, no. 1, pp. 30-45, 1986.

[83] AB Millimetre. (2013, June) Product information. [Online]. http://www.abmillimetre.com/Products.htm

[84] D. Slater, *Near-Field Antenna Measurements*, 10th ed., Helmut E. Schrank, Ed. Norwood, USA: Artech House, 1991.

[85] J. Säily, "Instrumentation of a submillimetre wave hologram compact antenna test range," Helsinki University of Technology, Espoo, Finland, Doctoral Dissertation 2003.

[86] Nearfield Systems Inc. (2013, May) Product information. [Online]. http://ww2.nearfield.com/Sales/datasheets/NSI-200V-5x5.htm

[87] J. Säily, P. Eskelinen, and A. V. Räisänen, "Pilot signal based real-time measurement and correction of phase errors caused by microwave cable flexing in planar near-field tests," *IEEE Transactions on Antennas and Propagation*, vol. 51, no. 2, pp. 195-200, 2003.

[88] A. D. Yaghjian, "Approximate formulas for the far field and gain of open-ended rectangular waveguide," *IEEE Transactions on Antennas and Propagation*, vol. 32, no. 4, pp. 378-384, 1984.

[89] Nearfield Systems Inc. (2013, May) Product information. [Online]. http://ww2.nearfield.com/Sales/ProbePattern.htm

[90] S. Martens, B. Gompf, and M. Dressel, "Characterization of continuous-wave terahertz sources: laser mixing versus backward-wave oscillators," *Applied Optics*, vol. 48, no. 29, pp. 5490-5496, 2009.

[91] R. Wylde. (2013, June) Absolute Terahertz Power/Energy Meter. [Online]. http://www.terahertz.co.uk/index.php?option=com_content&view=article&id=140&Itemid=443

[92] Stanford Research Systems. (2013, June) Product information. [Online]. http://www.thinksrs.com

[93] D. Gabor, "A New Microscopic Principle," *Nature*, vol. 116, pp. 777-778, 1948.

[94] E. N. Leith and J. Upatnieks, "Reconstructed wavefronts and communication theory," *Journal of the Optical Society of America*, vol. 52, no. 10, pp. 1123-1130, 1962.

[95] D. L. McMakin, D. M. Sheen, and H. D. Collins, "Remote concealed weapons and explosive detection on people using millimeter-wave holography," in *Proceedings of the 30th Annual International Carnahan Conference*, KY, 1996, pp. 19-25.

[96] D. M. Sheen, D. L. McMakin, and T. E. Hall, "Three-dimensional millimeter-wave imaging for concealed weapon detection," *IEEE Transactions on Microwave Theory and Techniques*, vol. 49, no. 9, pp. 1581–1592, 2001.

[97] G. Tricoles and N. H. Farhat, "Microwave holography: Applications and techniques," *Proceedings of the IEEE*, vol. 65, no. 1, pp. 108-121, 1977.

[98] M. Leach, M. Elsdon, S. J. Foti, and D. Smith, "Imaging dielectric objects using a novel synthetic off-axis holographic technique," *Microwave and Optical Technology Letters*, vol. 48, no. 10, pp. 1957–1961, 2006.

[99] D. Smith, M. Elsdon, M. Leach, M. Fernando, and S. J. Foti, "3D microwave imaging for medical and security applications," in *Proceedings of the International RF and Microwave Conference*, Putrajaya, Malaysia, 2006, pp. 233-237.

[100] J. Trontelj, "Micro-machined millimeter wave sensor array for FM radar application," in *Proceedings of SPIE, Terahertz Physics, Devices, and Systems VII: Advanced Applications in Industry and Defense*, Baltimore, MD, 2013, publication no. 85440G.

[101] G. Junkin and J. C. Bennett, "Holographic testing of terahertz antennas," *IEEE Transactions on Antennas and Propagation*, vol. 48, no. 3, pp. 409-417, 2000.

[102] D. J. Brady, K. Choi, D. L. Marks, R. Horisaki, and S. Lim, "Compressive Holography," *Optics Express*, vol. 17, no. 15, pp. 13040-13049, 2009.

[103] L. Denis, D. Lorenz, E. Thiébaut, C. Fournier, and D. Trede, "Inline hologram reconstruction with sparsity constraints," *Optics Letters*, vol. 34, no. 22, pp. 3475-3477, 2009.

[104] K. Khare and N. George, "Direct coarse sampling of electronic holograms," *Optics Letters*, vol. 28, no. 12, pp. 1004-1006, 2003.

[105] R. L. Baer, "Circular-edge spatial frequency response test," in *Proceedings of the SPIE, Image Quality and System Performance*, Orlando, FL, 2003, pp. 71-81.

[106] A. J. Fitzgerald, E. Berry, R. E. Miles, N. N. Zinovev, M. A. Smith, and J. M. Chamberlain, "Evaluation of image quality in terahertz pulsed imaging using test objects," *Physics in Medicine and Biology*, vol. 47, no. 21, pp. 3865–3873, 2002.

[107] "MIL-STD-150A, Photographic Lenses," Standard 1950.

[108] A. E. Burgess, "The Rose model, revisited," *Journal of Optical Society of America*, vol. 16, no. 3, pp. 633-646, 1999.

[109] D. G. Berry, R. G. Malech, and W. A. Kennedy, "The reflectarray antenna," *IEEE Transactions on Antennas and Propagation*, vol. 11, no. 6, pp. 645-651, 1963.

[110] C. S. Malagisi, "Microstrip disc element reflect array," in *Electronics and Aerospace Systems Convention*, Arlington, VA, 1978, pp. 186-192.

[111] J. P. Montgomery, "A microstrip reflectarray antenna element," in *Antenna Applications Symposium*, Urbana, IL, 1978, 19 p.

[112] D. M. Pozar, S. D. Targonski, and H. D. Syrigos, "Design of millimeter wave microstrip reflectarrays," *IEEE Transactions on Antennas and Propagation*, vol. 45, no. 2, pp. 287-296, 1997.

[113] P. F. Goldsmith, *Quasioptical Systems*, 10th ed., J. B. Anderson, Ed. New York: IEEE Press, 1998.

[114] M. Smith and Y. Guo, "A comparison of methods for randomizing phase quantization errors in phased arrays," *IEEE Transactions on Antennas and Propagation*, vol. 31, no. 6, pp. 821-828, 1983.

[115] J. Perruisseau-Carrier and A. K. Skrivervik, "Monolithic MEMS-based reflectarray cell digitally reconfigurable over a 360o phase range," *IEEE Antennas and Wireless Propagation Letters*, vol. 7, pp. 138-141, 2008.

[116] B. Wu, A. Sutinjo, M. E. Potter, and M. Okoniewski, "On the selection of the number of bits to control a dynamic digital MEMS reflectarray," *IEEE Antennas and Wireless Propagation Letters*, vol. 7, pp. 183-186, 2008.

[117] G. M. Rebeiz, G.-L. Tan, and J. S. Hayden, "RF MEMS phase shifters: design and applications," *IEEE Microwave Magazine*, vol. 3, no. 2, pp. 72-81, 2002.

[118] R. Malmqvist, C. Samuelsson, B. Carlegrim, P. Rantakari, T. Vähä-Heikkilä, A. Rydberg, and J. Varis, "Ka-band RF MEMS phase shifters for energy starved millimetre-wave radar sensors," in *International Semiconductor Conference*, Linköping, Sweden, 2010, pp. 261-264.

[119] A. S. Hedden, C. R. Dietlein, and A. Wikner, "Design of 220 GHz electronically scanned reflectarrays for confocal imaging systems," *SPIE Optical Engineering*, vol. 51, no. 9, publication no. 091611, 2012.

[120] C. R. Dietlein, A. S. Hedden, and D. A. Wikner, "Digital reflectarray considerations for terrestrial millimeter-wave imaging," *IEEE Antennas and Wireless Propagation Letters*, vol. 11, pp. 272-275, 2012.

[121] R. J. Mailloux, "Grating lobes and average sidelobe levels due to periodic phase, amplitude, and time-delay quantization," in *Phased Array Antenna Handbook*. Norwood, USA, MA: Artech House, 1994, ch. 7, pp. 403-404.

[122] J. Huang and J. A. Encinar, *Reflectarray Antennas*. New Jersey, USA: Wiley, 2008.

[123] D. M. Pozar, "Microstrip reflectarrays myths and realities," in *Proceedings of the International Symposium on Antennas*, Nice, France, 2004, pp. 175-179.

[124] H. Rajagopalan, S. Xu, and Y. Rahmat-Samii, "On understanding the radiation mechanism of reflectarray antennas: an insightful and illustrative approach," *IEEE Antennas and Propagation Magazine*, vol. 54, no. 5, pp. 14-38, 2012.

[125] J. Budhu and Y. Rahmat-Samii, "Understanding the appearance of specular reflection in offset fed reflectarray antennas," in *IEEE International Symposium on Antennas and Propagation – APSURSI,* Spokane, WA, 2011, pp. 97-100.

[126] S. V. Hum and M. Okoniewski, "A technique for predicting specular reflections from reflectarrays," in *IEEE Antennas and Propagation Society International Symposium Digest*, Honolulu, HI, 2007, pp. 2116-2119.

[127] J. W. Greiser, "Coplanar stripline antenna," U.S. Patent 4063246, June 1, 1976.

[128] K. Li, C. H. Cheng, T. Matsui, and M. Izutsu, "Coplanar patch antennas: principle, simulation and experiment," in *Proceedings of IEEE AP-S Symposium*, Boston, MA, 2001, pp. 402-405.

[129] D. M. Pozar, "Microstrip antenna aperture-coupled to a microstripline," *Electronics Letters*, vol. 21, no. 2, pp. 49-50, 1985.

[130] R. Q. Lee and R. N. Simons, "Coplanar-waveguide aperture-coupled microstrip patch antenna," *IEEE Microwave and Guided Wave Letters*, vol. 2, no. 4, pp. 138-139, 1992.

[131] H. Kamitsuna, "A very small, low-loss MMIC rat-race hybrid using elevated coplanar waveguides," *IEEE Microwave and Guided Wave Letters*, vol. 2, no. 8, pp. 337-339, 1992.

[132] T. Tokumitsu, T. Hiraoka, H. Nakamoto, and T. Takenaka, "Multilayer MMIC using a 3 mu m*3-layer dielectric film structure," in *IEEE MTT-S International Microwave Symposium Digest*, vol. 2, 1990, pp. 831-834.

[133] G. E. Ponchak and L. P. B. Katehi, "Measured attenuation of coplanar waveguide on CMOS grade silicon substrates with polyimide interface layer," *Electronics Letters*, vol. 34, no. 13, pp. 1327-1329, 1998.

[134] G. Ternent, S. Ferguson, Z. Borsofoldi, K. Elgaid, T. Lohdi, D. Edgar, C. D. W. Wilkinson, and I. G. Thayne, "Coplanar waveguide transmission lines and high Q inductors on CMOS grade silicon using photoresist and polyimide," *Electronics Letters*, vol. 35, no. 22, pp. 1957-1958, 1999.

[135] W. H. Haydl, "On the use of vias in conductor-backed coplanar circuits," *IEEE Transactions on Microwave Theory and Techniques*, vol. 50, no. 6, pp. 1571-1577, 2002.

[136] D. M. Pozar, "Bandwidth of reflectarrays," *Electronics Letters*, vol. 39, no. 21, pp. 1490-1491, 2003.

[137] J. Hanfling, G. Borgiotti, and L. Kaplan, "The backward transform of the near field for reconstruction of aperture fields," in *IEEE Antennas and Propagation Society International Symposium*, 1979, Seattle, WA, pp. 764-767.

[138] J. J. Lee, E. M. Ferren, D. P. Woollen, and K. M. Lee, "Near-field probe used as a diagnostic tool to locate defective elements in an array antenna," *IEEE Transactions on Antennas and Propagation*, vol. 36, no. 6, pp. 884-889, 1988.

[139] J.-D. Lacasse and J. Laurin, "A method for reflectarray antenna design assisted by near field measurements," *IEEE Transactions on Antennas and Propagation* , vol. 54, no. 6, pp. 1891-1897, 2006.

[140] S. Dieter and W. Menzel, "High-resolution probes for near-field measurements of reflectarray antennas," *IEEE Antennas and Wireless Propagation Letters*, vol. 8, pp. 157-160, 2009.

[141] S. Dieter, A. Mössinger, S. Müller, R. Jakoby, and W. Menzel, "Characterization of reconfigurable LC-reflectarrays using near-field measurements," in *German Microwave Conference*, Munich, Germany, 2009, 4 p.

[142] Y. Alvarez, M. Arrebola, F. Las-Heras, and J. A. Encinar, "On the sources reconstruction method application for a reflectarray antenna characterization," in *Proceedings of the 3rd European Conference on Antennas and Propagation*, Berlin, Germany, 2009, pp. 23-27.

[143] A. S. Nagra, X. Jian, E. Erker, and R. A. York, "Monolithic GaAs phase shifter circuit with low insertion loss and continuous 0-360° phase shift at 20 GHz," *IEEE Microwave and Guided Wave Letters*, vol. 9, no. 1, pp. 31-33, 1999.

[144] N. S. Barker and G. M. Rebeiz, "Distributed MEMS true-time delay phase shifters and wide-band switches," *IEEE Transactions on Microwave Theory and Techniques*, vol. 46, no. 11, pp. 1881-1890, 1998.

[145] N. S. Barker and G. M. Rebeiz, "Optimization of distributed MEMS transmission-line phase shifters-U-band and W-band designs," *IEEE Transactions on Microwave Theory and Techniques*, vol. 48, no. 11, pp. 1957-1966, 2000.

[146] J. S. Hayden and G. M. Rebeiz, "One and two-bit low-loss cascadable MEMS distributed X-band phase shifters," in *IEEE MTT-S International Microwave Symposium Digest*, vol. 1, Boston, MA, 2000, pp. 161-164.

[147] J. B. Muldavin and G. M. Rebeiz, "High-isolation CPW MEMS shunt switches. 1. Modeling," *IEEE Transactions on Microwave Theory and Techniques*, vol. 48, no. 6, pp. 1045-1052, 2000.

[148] J. B. Muldavin and G. M. Rebeiz, "High-isolation CPW MEMS shunt switches. 2. Design," *IEEE Transactions on Microwave Theory and Techniques*, vol. 48, no. 6, pp. 1053-1056, 2000.

[149] C. R. Birtcher, C. A. Balanis, and V. J. Vokurka, "RCS measurements, transformations, and comparisons under cylindrical and plane wave illumination," *IEEE Transactions on Antennas and Propagation*, vol. 42, no. 3, pp. 329-334, 1994.

[150] M. J. Coulombe, T. Horgan, J. Waldman, G. Szatkowski, and W. Nixon, "A 524 GHz polarimetric compact range for scale model RCS measurements," in *Proceedings of the Meeting and Symposium of Antenna Measurement and Techniques Association*, Monterey Bay, CA, 1999, pp. 458-463.

[151] E. Noponen, A. Tamminen, and M. Vaaja, "Design of transmission-type phase holograms for a compact radar-cross-section measurement range at 650 GHz," *Applied Optics*, vol. 46, no. 20, pp. 4181-4196, 2007.

[152] A. Ludwig, "The definition of cross polarization," *IEEE Transactions on Antennas and Propagation*, vol. 21, no. 1, pp. 116-119, 1973.

[153] A. Lönnqvist, J. Mallat, and A. V. Räisänen, "Phase-hologram-based compact RCS test range at 310 GHz for scale models," *IEEE Transactions on Microwave Theory and Techniques*, vol. 54, no. 6, pp. 2391-2397, 2006.

[154] J. Meltaus, J. Salo, E. Noponen, M. M. Salomaa, V. Viikari, A. Lönnqvist, T. Koskinen, J. Säily, J. Häkli, J. Ala-Laurinaho, J. Mallat, and A. V. Räisänen, "Millimeter-wave beam shaping using holograms," *IEEE Transactions on Microwave Theory and Techniques*, vol. 51, no. 4, pp. 1274-1280, 2003.

[155] M. J. Coulombe, T. Horgan, J. Waldman, G. Szatkowski, and W. Nixon, "A 585 GHz compact range for scale model RCS measurements," in *Prioceedings of the Meeting and Symposium of Antenna Measurement and Techniques Association*, Dallas, TX, 1993, pp. 129-134.

[156] R. Giles. (2013, May) Far-Infrared Radiation Absorbing Materials (FIRAM™). [Online]. http://www.uml.edu/Research/Centers/STL/Research/firam.aspx

[157] R. Giles. (2013, June) Product information. [Online]. http://www.uml.edu/docs/FIRAM_Absorber_Info_Sheet_tcm18-42245.pdf

[158] R. H. Giles, A. J. Gatesman, J. Fitzgerald, S. Fisk, and J. Waldman, "Tailoring artificial dielectric materials at terahertz frequencies," in *Proceedings of The 4th International Symposium on Space Terahertz Technology*, Los Angeles, CA, 1993, pp. 124-133.

[159] C. Wu, A. J. Gatesman, L. DeRoeck, T. Horgan, R. H. Giles, and W. E. Nixon, "Terahertz backscattering behavior of various absorbing materials," in *Proceedings of SPIE, Terahertz Physics, Devices, and Systems III: Advanced Applications in Industry and Defense*, Orlando, FL, 2009, publication no. 73110M.

[160] J. Tuovinen, A. Lehto, and A. V. Räisänen, "Performance of Absorbers and Anechoic Chambers at 110 GHz and 183 GHz," in *Proceedings of the 20th European Microwave Conference*, Budapest, Hungary, 1990, pp. 371-376.

[161] J. Säily and A. V. Räisänen, "Characterization of submillimeter wave absorbers from 200–600 GHz," *International Journal of Infrared and Millimeter Waves*, vol. 37, no. 1, pp. 71-88, 2004.

[162] J. Säily, J. Mallat, and A. V. Räisänen, "Reflectivity measurements of various commercial absorbers at millimetre and submillimetre wavelengths," *Electronics Letters*, vol. 37, no. 3, pp. 143-145, 2001.

[163] A. Murk, "Baseline measurements with 650 GHz radiometer," in *Proceedings of the 2nd ESA Workshop on Millimetre wave technology and applications: antennas, circuits and systems*, Espoo, Finland, 1998, pp. 121-126.

[164] A. Murk and N. Kämpfer, "Baseline issues in an airborne 650 GHz radiometer," in *COST-712 Workshop on Microwave Techniques in Meteorology*, Bern, Germany, 1999, pp. 41-51.

[165] P. L. Richards, "Bolometers for infrared and millimeter waves," *Journal of Applied Physics*, vol. 76, no. 1, 24 p., 1994.

[166] K. D. Irwin, G. C. Hilton, D. A. Wollman, and J. M. Martinis, "X-ray detection using a superconducting transition-edge sensor microcalorimeter with electrothermal feedback," *Applied Physics Letters*, vol. 69, no. 13, pp. 1945-1947, 1996.

[167] A. T. Lee, P. L. Richards, S. W. Nam, B. Cabrera, and K. D. Irwin, "A superconducting bolometer with strong electrothermal feedback," *Applied Physics Letters*, vol. 69, no. 12, pp. 1801-1803, 1996.

[168] A. Luukanen, E. N. Grossman, A. J. Miller, P. Helistö, J. S. Penttilä, H. Sipola, and H. Seppä, "An ultra-low noise superconducting antenna-coupled microbolometer with a room-temperature read-out," *IEEE Microwave and Wireless Components Letters*, vol. 16, no. 8, pp. 464-466, 2006.

[169] A. Luukanen, M. Grönholm, P. Lappalainen, M. Leivo, A. Rautiainen, A. Tamminen, J. Ala-Laurinaho, A. V. Räisänen, C. R. Dietlein, and E. N. Grossman, "Passive real-time submillimetre-wave imaging system utilizing antenna-coupled microbolometers for stand-off security screening applications," in *International Workshop on Antenna Technology*, Lisbon, Portugal, 2010, 4 p.

[170] J. D. Dyson, "The equiangular spiral antenna," *IRE Transactions on Antennas and Propagation*, vol. 7, no. 2, pp. 181-187, 1959.

[171] A. Tamminen, J. Ala-Laurinaho, J. Mallat, A. Luukanen, E. Grossman, and A. V. Räisänen, "Characterization of Antenna-coupled Microbolometers for THz-imaging," in *Proceedings of the 31st ESA Antenna Workshop*, Noordwijk, The Netherlands, 2009, pp. 441-446.

[172] E. N. Grossman, C. R. Dietlein, J. E. Bjarnason, M. Ramirez, M. Leivo, J. S. Penttilä, P. Helistö, and A. Luukanen, "Imaging with modular linear arrays of cryogenic Nb microbolometers," in *Proceedings of SPIE, Passive Millimeter-Wave Imaging Technology XI*, Orlando, FL, 2008, publication no. 694806.

[173] A. Luukanen, L. Grönberg, M. Grönholm, P. Lappalainen, M. Leivo, A. Rautiainen, A. Tamminen, J. Ala-Laurinaho, C. R. Dietlein, and E. Grossman, "Real-time passive terahertz imaging system for standoff concealed weapons imaging," in *Proceedings of SPIE 7670, Passive Millimeter-Wave Imaging Technology XIII*, Orlando, FL, 2010, publication no. 767004.

[174] A. Luukanen, T. Kiuru, M. Leivo, A. Rautiainen, and J. Varis, "Passive three-colour submillimetre-wave video camera," in *Proceedings of SPIE, Passive and*

Active Millimeter-Wave Imaging XVI, Baltimore, MD, 2013, publication no. 87150F.

[175] T. Büttgenbach, "An improved solution for integrated array optics in quasi-optical mm and submm receivers: the hybrid antenna," *IEEE Transactions on Microwave Theory and Techniques*, vol. 41, no. 10, pp. 1750-1760, 1993.

[176] D. F. Filipovic, S. S. Gearhart, and G. M. Rebeiz, "Double-slot antennas on extended hemispherical and elliptical silicon dielectric lenses," *IEEE Transactions on Microwave Theory and Techniques*, vol. 41, no. 10, pp. 1738-1749, 1993.

[177] D. F. Filipovic, G. P. Gauthier, S. Raman, and G. M. Rebeiz, "Off-axis properties of silicon and quartz dielectric lens antennas," *IEEE Transactions on Antennas and Propagation*, vol. 45, no. 5, pp. 760-766, 1997.

[178] Y. Mushiake, "Self-complementary antennas," *IEEE Antennas and Propagation Magazine*, vol. 34, no. 6, pp. 23-29, 1992.

[179] A. Luukanen and J. P. Pekola, "A superconducting antenna-coupled hot-spot microbolometer," *Applied Physics Letters*, vol. 82, no. 22, pp. 3970-3972, 2003.

[180] C. Dietlein, J. D. Chisum, M. D. Ramirez, A. Luukanen, E. N. Grossman, and Z. Popovic, "Integrated microbolometer antenna characterization from 95-650 GHz," in *IEEE MTT-S International Microwave Symposium Digest*, Honolulu, HI, 2007, pp. 1165-1168.

[181] H. Eisele, M. Naftaly, and J. R. Fletcher, "A simple interferometer for the characterization of sources at terahertz frequencies," *Journal of Measurement Science and Technology*, vol. 18, no. 8, pp. 2623-2628, 2007.

[182] M. Naftaly, A. Malcoci, and H. Eisele, "A sensitive broadband detector for room-temperature operation of a simple terahertz Fourier-transform spectrometer," in *Proceedings of Joint 31st International Conference on Infrared and Millimeter Waves and 14th International Conference on Teraherz Electronics*, Shanghai, China, 2006, 3 p.

[183] F. Voltolina, U. Dillner, E. Kessler, and P. H. Bolivar, "Realization of a quasi-commercial terahertz detector," in *Proceedings of the 40th European Microwave Conference*, Paris, France, 2010, pp. 65-68.

[184] S. Preu, *Continuous-wave, tunable THz n-i-pn-i-p superlattice photomixers and applications*, S. Malzer et al., Eds. Erlangen-Nürnberg: Erlangen Scientific Press, 2009.

[185] Murata Manufacturing Co., Ltd. (2013, May) Pyroelectric Infrared Sensors. [Online]. http://www.murata.com/products/catalog/pdf/s21e.pdf

[186] Gentec EO. (2013, June) THz Detectors. [Online]. https://www.gentec-eo.com/products/thz-detectors/THZ12

[187] D. Dooley. (2013, June) Application Note 1011 Rev. A. [Online]. photonics.com/ShowObject.aspx?MID=245

[188] Tydex Optics. (2013, June) Golay cell GC-1P, product information. [Online]. http://www.tydexoptics.com/products/thz_optics/golay_cell/

Errata

Publication I

In the second paragraph of Section IV it should read "…in equation (6) is seen.". In the third paragraph of Section IV it should read "…as is in equation (8)."

In the fourth paragraph of Section II B. it should read "The convolutions in spectrum (6) are also located around thespatial frequency $k_{r,x}$ defined in equation (7). The first two terms in equation (6) represent the autocorrelations of the fields, and are located around the origin of the spectrum."

Publication III

In the fourth paragraph of Section II, equation (5) is erroneous. A correct formulation is presented in this thesis in Section 3. 1. 2.

This thesis explores a range of experimental techniques and methods at millimeter and submillimeter wavelengths. Significant interest in technological developments at this frequency range has continued over the past two decades, which has also yielded several advancements for commercial applications. The key prospects afforded by millimeter- and submillimeter-wave technologies, such as the capability of providing high-resolution imagery, has resulted in emerging commercial imaging-based applications. This thesis concentrates on the development of imaging methods and technology from 120 to 782 GHz, and it includes indirect holographic imaging, detector characterization, reflectarrays for beam forming, and material reflectivity studies. The thesis offers alternative imaging solutions to current state-of-the-art methods, which utilize complex transmitter and receiver technologies. The experimental results provide novel information on material properties and guide the development of power detectors and reflectarrays.

Aalto-DD 131/2013

9 789526 053004

ISBN 978-952-60-5300-4
ISBN 978-952-60-5301-1 (pdf)
ISSN-L 1799-4934
ISSN 1799-4934
ISSN 1799-4942 (pdf)

Aalto University
School of Electrical Engineering
Department of Radio Science and Engineering
www.aalto.fi

BUSINESS +
ECONOMY

ART +
DESIGN +
ARCHITECTURE

SCIENCE +
TECHNOLOGY

CROSSOVER

DOCTORAL
DISSERTATIONS